Molecular Strong Field Ionization viewed with Photoelectron Velocity Map Imaging

A Dissertation presented

by

Péter Sándor

to

The Graduate School

in Partial Fulfillment of the

Requirements

for the Degree of

Doctor of Philosophy

in

Physics

Stony Brook University

Spring 2016

Stony Brook University

The Graduate School

Péter Sándor

We, the dissertation committe for the above candidate for the
Doctor of Philosophy degree, hereby recommend
acceptance of this dissertation

Thomas C. Weinacht - Dissertation Advisor
Professor, Department of Physics and Astronomy, Stony Brook University

Dominik A. Schneble - Chairperson of Defense
Associate Professor, Department of Physics and Astronomy, Stony Brook University

Matthew Dawber - Committee Member
Associate Professor, Department of Physics and Astronomy, Stony Brook University

Thomas Bergeman - Committee Member
Adjunct Professor, Department of Physics and Astronomy, Stony Brook University

Thomas Baumert - External Committee Member
Professor, Institute of Physics, University of Kassel

This dissertation is accepted by the Graduate School

Charles Taber
Dean of the Graduate School

Abstract of the Dissertation

Molecular Strong Field Ionization viewed with Photoelectron Velocity Map Imaging

by

Péter Sándor

Doctor of Philosophy

in

Physics

Stony Brook University

2015

In this thesis, work is presented on Molecular Strong Field Ionization, during which an electron is removed from polyatomic molecules in the presence of strong laser fields. This is a process which is the basis of a number of experimental techniques to uncover electronic dynamics in atoms and molecules on the femtosecond and attosecond timescale. 'Strong' refers to an electric field strength which leads to a response from the system which can not be modeled perturbatively. These fields can be easily produced in the focus of femtosecond laser radiation, as is done in this work.
With the use of Velocity Map Imaging of the photoelectron in coincidence with the fragment ion, multiple ionization–dissociation pathways can be distinguished. It is shown that as opposed to early attempts to model the process, multiple low-lying states are populated in the ion, and also the signatures of multi-electron dynamics are revealed.
By changing the laser pulse duration from 30 fs to below 10 fs, control is demonstrated over which quantum states of the ion are populated. It is also shown that for pulses shorter than 10 fs (which is a timescale below the shortest vibrational period in molecules), ionization pathways that involve motion of the nuclei are almost completely shut off.
Finally, the origin of electrons with <1 meV kinetic energy is discussed. A two-step model is proposed for creating the electrons: the first step is population transfer to high-lying excited states of the neutral molecule by the laser field; the second step is ionization. Different ionization mechanisms are examined and their viability is checked against available data.

To my family.

Contents

List of Figures

Acknowledgements

This work would have not been possible to bring about without the help, assistance and support of a great number of people who have contributed to it in one way or another, knowingly or unknowingly. Here I would merely like to show my appreciation to them.

First and foremost I would like to thank my family: Mom, Dad, Attila and Balázs for bearing with me and supporting me even from afar. The physical distance has tested the strength of the bond between us—which, I am happy to say, proved to be pretty strong, and gives me some reassurance that I did the right thing when I moved to the U.S. for my studies.

I want to thank Tom for being an outstanding advisor. He has really been supportive and flexible all these years and stayed on the ball 24/7, always ready to solve problems being it technical, scientific, or political in nature. In addition, he has always been an advocate of clear thinking and clear presentation, making him an extraordinary teacher and making us a little better at expressing our ideas.

I owe our group, past and current members alike. Marty Cohen has been a pillar we could all rely on, helping out with his professional advice on optics and lasers. Chien-Hung Tseng (Coco) was the first one with whom I worked in the lab. We struggled together with making the 2D experiments work in the UV. Even though none of that made it to this thesis, those were heroic times for me and will remember them. Dominik Geißler introduced me to the world of charged particle detection and velocity map imaging (VMI). The chamber we made my first such measurements on (originally built by Sarah Nichols), I ended up ”inheriting” from him. It proved to be an entirely different game compared to the experiments I had done before. He had the procedures already worked out in terms of experimentation and data processing. Most of these I continued to use up until the last data runs, they were figured out so well. Others we disagreed on and continued to have fruitful discussion on. (How to use the Abel-inversion routines?) With him, Will Lunden and Arthur Zhao, the four of us started developing the photoelectron imaging and later, the coincidence detection scheme. Those were great times, thank you all for being there and making it happen. The coincidence machine matured through my collaboration with Arthur, and we made some milestone measurements together. Even though we didn't have big projects together with Spencer Horton, he could easily be the guy I talked to the most. His super friendly personality brought the whole AMO community together at Stony Brook. The two of us showed others what foosball o'clock is about (go Cougar Baits!), not to mention an occasional, stress-relieving movie night. It's been jolly good times. A special thanks goes to Vincent Tagliamonti, whom I had the privilege to get to know and spend time with in- and outside the lab. Being reliable, conscientious and a real team player, working with him on the measurements involving the filamentation-based light source was most enjoyable.

A big thanks goes out to my fellow basement-dwellers, AMO students in the labs of Schneble, Metcalf, Allison and Figueroa, past and present. I am hesitant to list any names, there are too many! It has been wonderful to be able to rely on each other's help, being it diverting lab floods, disposing of dead animals from the air vent, getting a helping hand in the machine shop, or just borrowing an equipment or an adapter for that special connector nobody produces since the 1960's.

At this point I would also like to thank those who made the department work. László Mihály, Jac

Verbaarschot and Sara Lutterbie made it possible for me to join the physics graduate program at Stony Brook in the first place, and with Socoro Delquaglio, they took care of all the administration since. Nathan Leoce-Schappin and Don Sheehan helped make my 'endgame' smooth. The staff of the machine shop—especially Walter and JT—were instrumental in making some of the hardware work. They have always been professional, available and friendly—in case of JT, friendliness of course means that unsparingly satirical kind. Linda at shipping has always been a pleasure to come by.

Last but not least, I would like to thank the committee members, most of whom have followed my progress since my oral exam: Dominik Schneble, Matthew Dawber, and Tom Bergeman. I was grateful for Thomas Baumert for joining us from Germany.

Chapter 1

Introduction

Ultrafast laser science has come a long way since its advent in the nineteen-seventies. There are a number of aspects in which various ultrafast laser systems around the world exhibit unprecedented performance; some of these aspects are inseparable. Firstly, achievable bandwidths of the available gain media enables the shortest electromagnetic pulses, reaching the limit where the duration becomes equal to a single optical period in the near infrared ($\approx$2.7 fs), or even measurable on the 10 as scale in the XUV. Secondly, systems around the world take advantage of clever ways to scale up energy per laser pulse, called Chirped Pulse Amplification [1, 2, 3], which, combined with the short pulse duration, can generate the highest peak powers achievable (measured in PetaWatts). Thirdly, choosing the frequency of radiation in an enormous range is enabled by making use of matter's highly nonlinear response to strong electromagnetic driving fields. (This has results in anything between accelerating charges with femtosecond pulses to create THz radiation to using frequency-mixing processes to produce infrared 'light' to generating the 100th or higher harmonics of the fundamental 800 nm to go up into the XUV regime.) Fourthly, precise control of the temporal shape of the electromagnetic radiation can be exerted on two timescales. Pulse shaping techniques (involving light-modulating optical elements and fast electronics) can be used to sculpt the envelope of the electric field, usually employed for pulses containing many optical cycles. In case of the few- or single-cycle regime, optical interferometry is well suited to provide a feedback mechanism for locking the carrier-envelope phase (CEP).

All the techniques listed above benefited from innovative ideas, and from a long evolution, during which the details of each method and principle were analyzed, understood and mastered. Eventually this made the systems built based on them more reliable. The remarkable advance in technology in turn created a fertile ground for research in a diverse collection of fields in biology, chemistry and physics. The common goal in case of all three is to look at systems of various sizes with unprecedented spatial and/or temporal resolution. However, the physical scientists and engineers also carry the burden (and bath in the glory) of pushing the technological frontier further by understanding the fine details of light-matter interaction. One such important detail out of the many has to do with what happens to an electron when it is ripped off from its host atom or molecule by a strong electric field. Needless to say that when molecules are considered, we find a field rich in things to discover. The phenomenon is then straightforwardly named molecular strong field ionization (molecular SFI or MSFI), and is the central subject of this thesis.

Strong field ionization plays a key role in high harmonic generation (HHG), creating electron wave packets [4, 5, 6] and attosecond electron dynamics [7, 8]. It can also be used to track excited state molecular dynamics [9] and for imaging molecular structure, both electronic and nuclear [10, 11, 12]. Understanding what states of the molecular cation are populated, and how, is very important for producing and probing electron wave packets, as well as for understanding strong field ionization as a tool

for molecular imaging and as a probe of neutral dynamics. Current work, amongst others, aims to explore how ionization depends on the parameters of the strong-field driving pulse, such as pulse duration [13, 14], chirp [15], central frequency etc.

This thesis is organized as follows:

In chapter 2, the experimental apparatus (laser system, vacuum chamber, charged particle optics), data acquisition methods (coincidence and non-coincidence velocity map imaging schemes) and data processing algorithms (used to convert a measured VMI image to photoelectron/ion spectrum) are introduced. These were employed during the work outlined in the later chapters of the thesis.

Chapter 3 builds upon earlier work which established direct ionization to multiple states of the molecular cation via coincidence detection of electrons and ions [16]. We present the first measurements on CH_2IBr and CH_2BrCl using coincidence detection of photoelectrons and ions with velocity map imaging of the photoelectrons. By combining our coincidence measurements with *ab initio* electronic structure and dynamic Stark shift calculations for the molecular cations, peaks are assigned in the photoelectron spectrum to specific ionic states; different ionization–dissociation pathways are also distinguished.

In chapter 4, strong-field molecular ionization is studied as a function of pulse duration, going from several tens of femtoseconds to below 10 fs, where vibrational dynamics is frozen out (the 'impulsive limit') [17]. Surprisingly, it is found that as the pulse duration is shortened from about 40 fs to less than 10 fs, there is a dramatic change in the photoelectron spectrum, which reflects a change in the combination of ionic continua that are accessed during the ionization process. Similar behavior is observed in three different molecules (CH_2IBr, CH_2BrCl and C_6H_5I) and it is demonstrated that the result depends more sensitively on pulse duration than spectral content. For CH_2IBr, the experimental measurements are further interpreted in terms of calculations of strong-field molecular ionization which include vibrational dynamics on intermediate neutral states during the ionization process.

In chapter 5, a peculiar feature is examined in the velocity map images of a number of different atomic and molecular systems: it is called the zero energy structure (ZES) and manifests itself as a sharply peaked distribution of electrons with energy <1 meV. The behavior of the structure is studied as a function of laser pulse paremeters, including peak intensity and bandwidth, and it is checked against current understanding how such low-energy electrons may be produced. This chapter is more open ended than the previous ones, since the measurements and their interpretation are not yet complete.

Chapter 2

Experimental Apparatus

2.1 Laser System

The main tool for producing ultrashort laser pulses for the experiments in the present thesis is a Ti:Sapphire-based amplified laser system. The heart of the system is a soft-aperture Kerr-lens modelocked Ti:S femtosecond oscillator from KM Labs, shown in figure 2.1. The crystal inside the laser cavity is optically pumped by a continuous-wave diode-pumped, frequency-doubled Nd:Vanadate (Nd:YVO_4) laser (Verdi V-5). The output of the oscillator is sent to the multipass amplifier stage (KM Labs HAP-AMP), which is pumped by a diode-pumped, intracavity frequency-doubled, Q-switched Nd:YLF laser (Photonics DM-20, see figure 2.2). The amplifier increases the pulse energy from a few nanoJoules to 1 mJ at 1 kHz repetition rate. The center wavelength is usually somewhere between 760 and 790 nm, and the bandwidth supports 30 fs pulses (see figure 2.6).

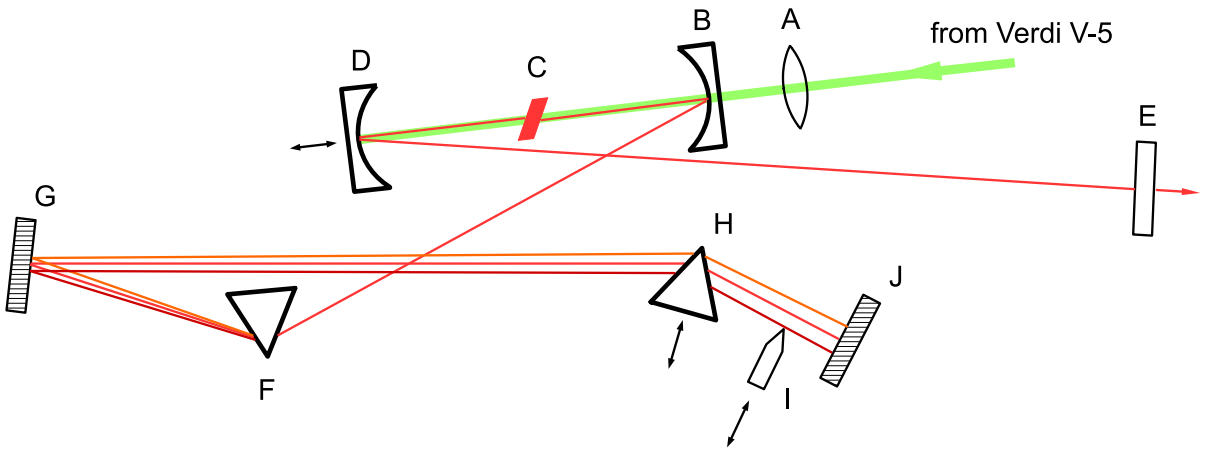

Figure 2.1: KM Labs Ti:S oscillator. A: pump focusing lens; B,D: curved dielectric mirrors; C: Ti:S crystal; E: output coupler; F,H: prisms; I: razor blade (for controlling the central wavelength); G: folding dielectric mirror; J: end mirror

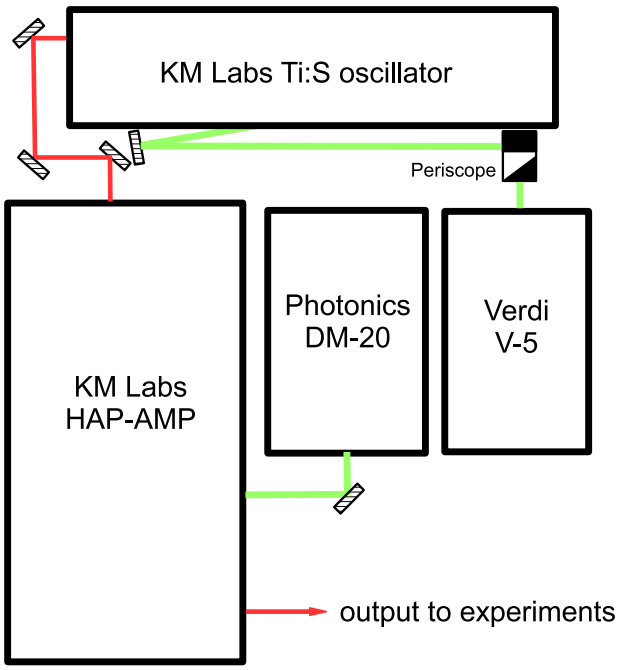

Figure 2.2: Schematic drawing of the full laser system. 'Periscope' shifts the level of the beam and rotates its polarization by 90°.

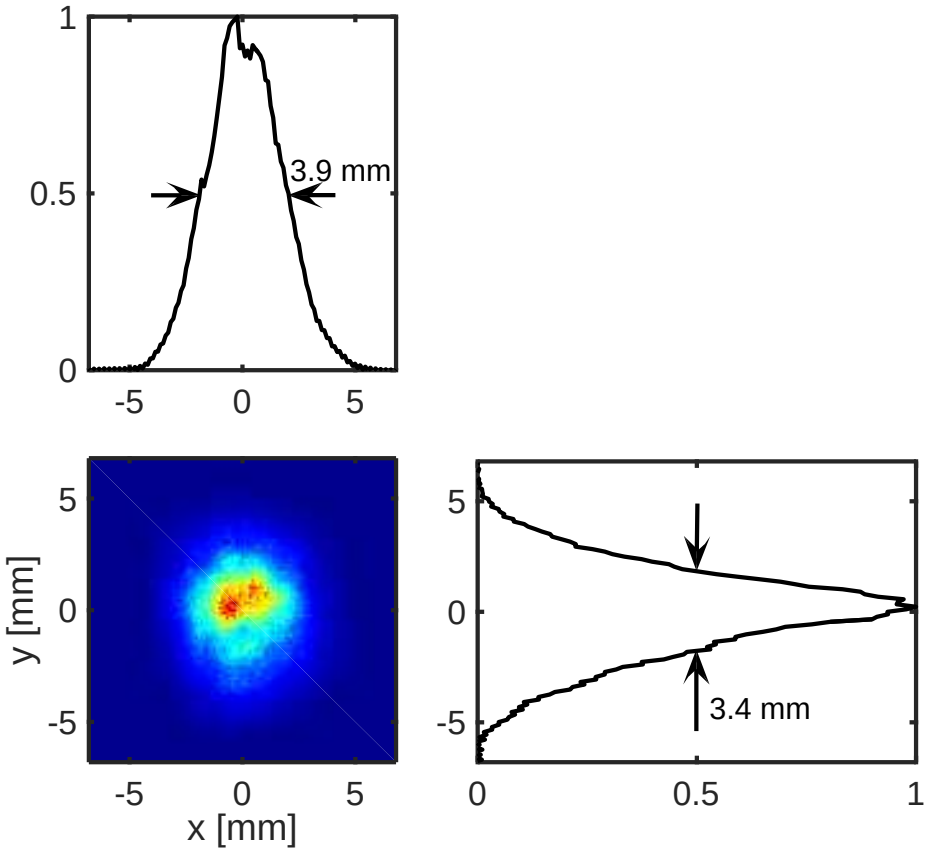

Figure 2.3: Amplifier beam profile with no 2x downcollimating telescope at the output. The colormap is linear with blue and red colors corresponding to lower and higher intensities, respectively.

2.2 Characterization of Ultrashort Pulses

The electric field of the laser can be completely described either in the time or in the frequency domain by the complex quantities $\tilde{E}(t)$ and $\tilde{E}(\omega)$, respectively. The two are equivalent and connected by the Fourier-transform.

$$\tilde{E}(\omega) = \frac{1}{\sqrt{2\pi}} \int_{-\infty}^{+\infty} \tilde{E}(t) e^{-i\omega t} dt$$

The electric field as a function of time is of course a real quantity, and it can be calculated by adding $\tilde{E}(t)$ and its complex conjugate: $E(t) \propto \tilde{E}(t) + \tilde{E}(t)^*$. For subsequent discussions, it is convenient to explicitly separate the amplitude and the phase of the field:

$$\tilde{E}(t) = E_0(t) e^{i\phi(t)}$$

$$\tilde{E}(\omega) = E_0(\omega) e^{i\phi(\omega)}$$

Here, $E_0(t)$ and $E_0(\omega)$ are real quantities, corresponding to the field amplitudes as a function of time and angular frequency, respectively. In the frequency domain, the phase is frequently expanded in Taylor-series around the central frequency ω_0 and the first few of the resulting coefficients are recognized to affect the time-domain field in different, but physically intuitive ways.

$$\begin{aligned} \phi(\omega) &= \phi_0 + \phi_1(\omega - \omega_0) + \phi_2(\omega - \omega_0)^2 + \phi_3(\omega - \omega_0)^3 + \dots \\ &= \phi_0 + GD(\omega - \omega_0) + \frac{GDD}{2}(\omega - \omega_0)^2 + \frac{TOD}{6}(\omega - \omega_0)^3 + \dots \end{aligned}$$

Where $\phi_0 \equiv \phi(\omega_0)$, an unimportant overall phase, $\phi_1 \equiv \left.\frac{d\phi}{d\omega}\right|_{\omega_0}$ is called the group delay (GD), which changes the arrival time of the pulse. $\left.\frac{d^2\phi}{d\omega^2}\right|_{\omega_0}$ and $\left.\frac{d^3\phi}{d\omega^3}\right|_{\omega_0}$ are called the group delay dispersion (GDD) and the third-order dispersion (TOD), respectively. GDD essentially controls the length of the pulse in time. In case of pulses with Gaussian intensity envelope, the functional form of the envelope stays the same for different values of the GDD, only its duration varies. For any functional form of the intensity and for GDD$\neq$0, the instantaneous frequency of the pulse becomes 'chirped' such that for GDD$>$0 (normal dispersion) "red colors arrive earlier", while for GDD$<$0 (anomalous dispersion) "blue colors arrive earlier". TOD can alter the temporal profile of the pulse substantially, giving rise to pre- or postpulses.
In the special case when $\phi(\omega) \equiv 0$, i.e. all the coefficients vanish, the field and the intensity ($I(t) = \frac{1}{2}\epsilon_0 c|\tilde{E}(t)|^2$) profile of the pulse has the shortest duration in time for the given amplitude distribution $E_0(\omega)$ and is said to be transform-limited (TL). There is no way to make the pulse shorter than this (which is dictated by the shape and the frequency content of the amplitude profile) just by manipulating the phase. For more on this topic see section 2.4.

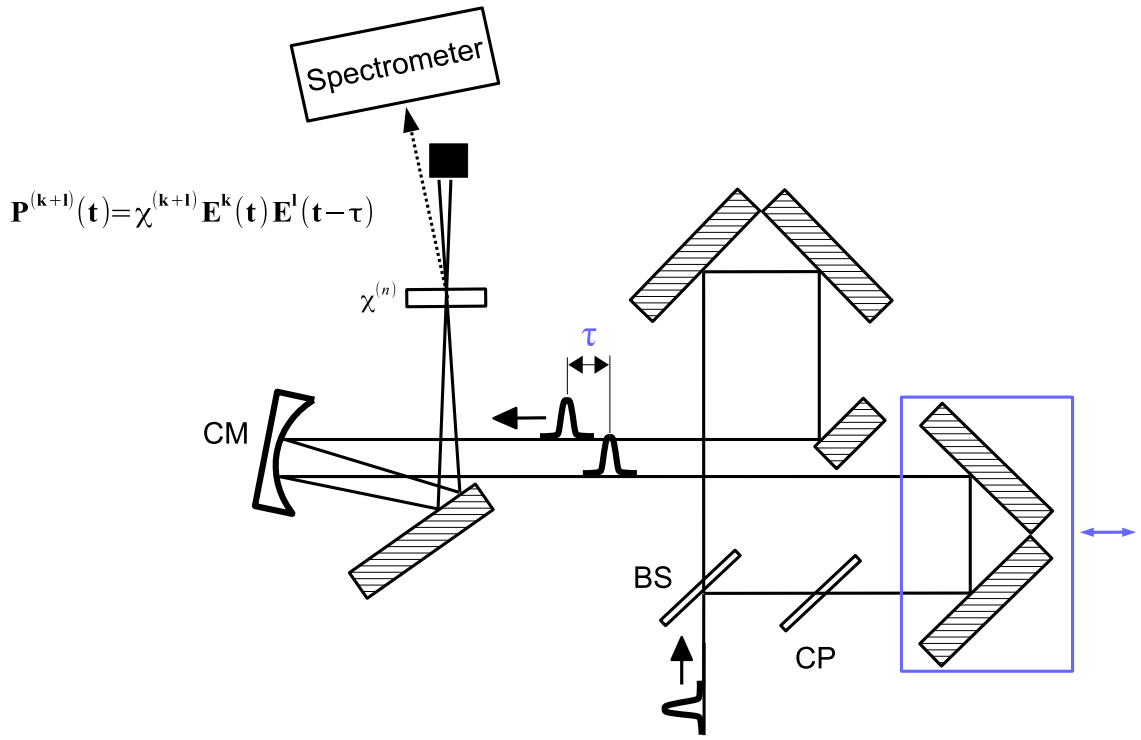

Figure 2.4: Optical setup for Frequency Resolved Optical Gating (FROG). BS: Beam Splitter; CP: Compensation Plate; CM: Curved Mirror

Characterization of the pulses was carried out with the frequency-resolved optical gating (FROG) technique [18]. For layout of the optical setup, see figure 2.4. This relies on the ultrashort pulse being time-gated with a replica in a nonlinear medium, producing a background-free signal which has an amplitude that is very sensitive to the temporal overlap between the two pulses. The signal is spectrally resolved at every time-delay τ. For a second-order nonlinearity, as in case of second-harmonic generation (SHG), the signal is given by

$$S_{SHG}(\omega,\tau) = \left|\int_{-\infty}^{+\infty} \chi^{(2)}\tilde{E}(t)\tilde{E}(t-\tau)e^{-i\omega t}dt\right|^2$$

where $\chi^{(2)}$ is the second-order nonlinear susceptibility, $\tilde{E}(t)$ and $\tilde{E}(t-\tau)$ are the complex electric fields for the pulse and its time-delayed replica, and τ is the time delay between the two. The SHG FROG trace of the amplifier output pulse is shown on figure 2.5, from which the intensity as a function of time (and also frequency) can be reconstructed (figure 2.6). It is worth noting that such a measurement does not contain information about the direction of time, so the measured SHG FROG trace will be symmetric. Practically speaking, there will be no measurable difference e.g. between a positively or negatively chirped pulse. One way to discriminate between these two cases is to perform a FROG measurement using an odd-order nonlinearity. The χ^3 coefficient is used in case of self-diffraction (SD) FROG measurements. The SD signal is generated by modulating the refractive index using the optical Kerr effect in a medium with two pulses that cross at a small angle. The modulated refractive index acts as a grating, and diffracts a portion of the incident beams to new beams, one of which is detected. Apart from getting rid of the time-ambiguity, SD FROG has the property that the signal has the same central wavelength as that of the input pulse, which is advantageous in certain wavelength regions, e.g. in the UV. The signal is given by:

$$S_{SD}(\omega,\tau) = \left|\int_{-\infty}^{+\infty} \chi^{(3)}\tilde{E}^2(t)\tilde{E}^*(t-\tau)e^{-i\omega t}dt\right|^2$$

Here, * denotes complex conjugation.

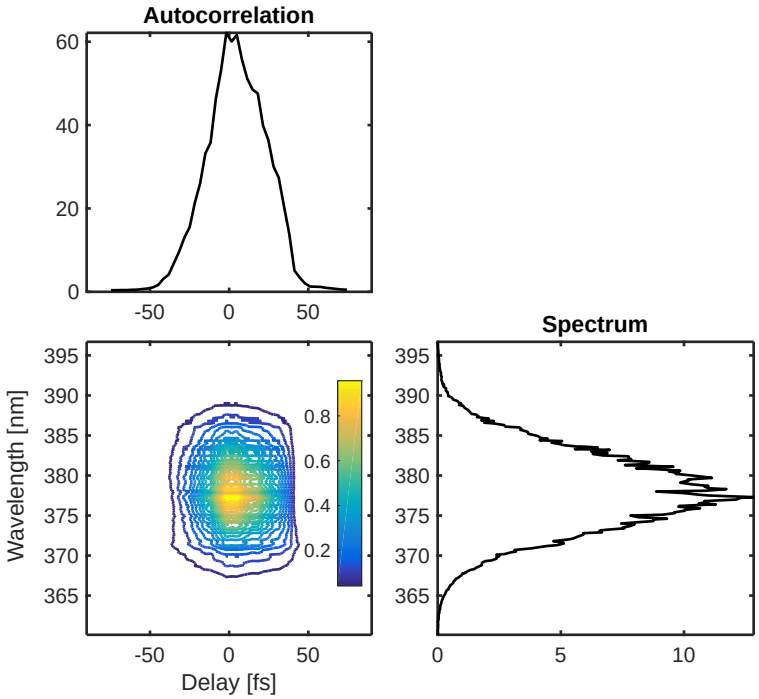

Figure 2.5: Typical amplifier SHG FROG trace (bottom left panel) with the marginals: autocorrelation (top left) and spectrum (bottom right).

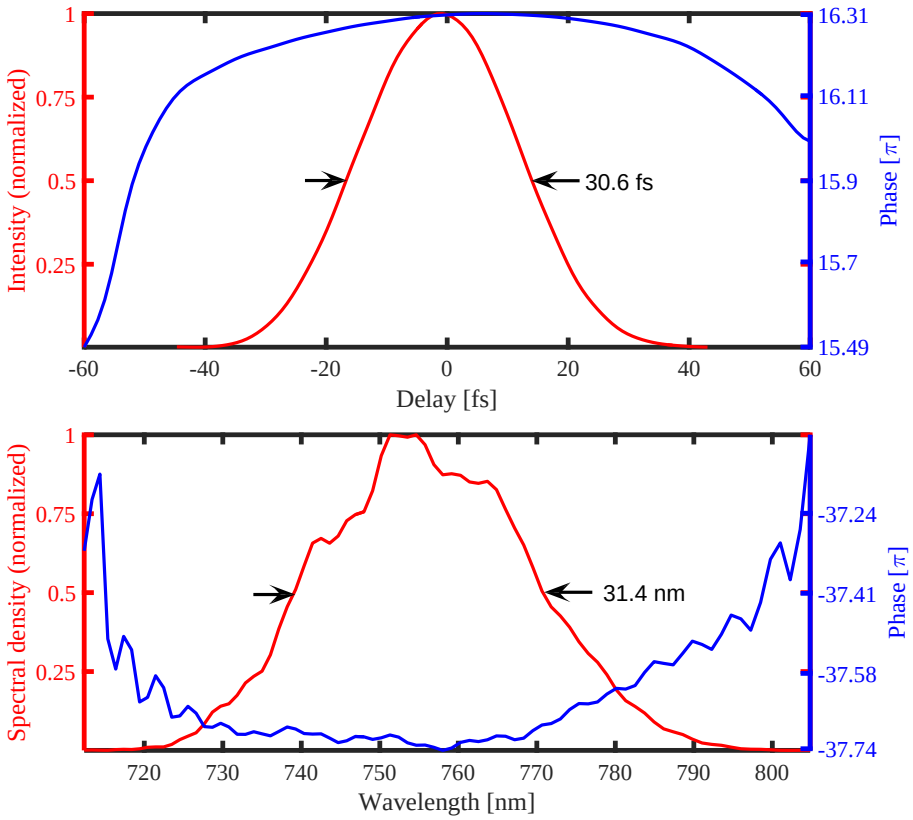

Figure 2.6: Reconstructed SHG FROG trace for the pulses from the ultrafast amplifier. Intensity (red curve) and phase (blue curve) profiles are shown as a function of time (top panel) and wavelength (bottom panel).

2.3 Pulse Shaping

As outlined in section 2.2, the time-domain electric field profile can be manipulated by changing the field in the frequency domain. Extensive use of this pulse shaping technique have been made to finely control the intensity profile of the laser pulses used in some of the experiments. Our pulse shaper is a grating pulse stretcher/compressor arranged in 4-f geometry with an acousto-optic modulator (AOM) placed in the Fourier-plane as an active element [19]. A traveling acoustic wave is launched in the AOM such that part of the optical beam incident on it undergoes Bragg-diffraction and forms an output beam. The diffracted angle θ_B is given by the Bragg-condition: $\sin(\theta_B) = \frac{\lambda}{2\Lambda}$, where λ is the optical and Λ is the acoustic wavelength. The acoustic waveform is generated with a piezoelectric transducer driven with a radio frequency (RF) electrical signal. The low-amplitude waveform for the RF signal is synthesized by an arbitrary waveform generator card with 1 GHz sampling rate and 300 MHz analog bandwidth (Compugen CG11G from GaGe Applied Sciences), low-pass filtered (3 dB at 250 MHz) and amplified such that the RF peak power driving the piezo transducer is 2W.

The device is capable of controlling both the spectral amplitude and the phase of the optical field, such that its effect can be described with the spectral transfer function $M(\omega)$: $E_{out}(\omega) = M(\omega)E_{in}(\omega)$. The optical angular frequency ω is mapped to a spatial coordinate 'x' along the length of the AOM. On the timescale of the laser pulse (tens of femtoseconds) the acoustic wave appears 'frozen', since the acoustic velocity (4.2 $\frac{mm}{\mu s}$ in TeO_2) is much less than the speed of light. This means that there is also a well-defined linear mapping between the coordinate 'x' and the acoustic arrival time (t_{AC}). Ultimately, acoustic arrival

time can be converted to optical frequency by calibrating the pulse shaper:

$$\omega = \alpha \cdot t_{AC} + \beta \tag{2.1}$$

Here α and β are parameters that are determined by the optical imaging and the properties of the RF signal collectively. With this calibration in hand, it is straightforward to calculate the acoustic waveform that is required to program any kind of optical transfer function $M(\omega)$.
As a simple example we show that if an electronically generated time delay is needed, the required linear spectral phase will lead to a constant offset of the acoustic frequency.[1] The transfer function for a time delay of τ is given by: $M(\omega) = e^{i\tau(\omega-\omega_0)}$. Here the optical frequencies are parametrized with the acoustic arrival time (see equation 2.1): $\omega = \omega(t_{AC})$ and $\omega_0 = \omega(t_0)$ where t_0 is a fixed reference time. The acoustic waveform to be synthesized (S_{RF}) is the product of the transfer function waveform and the carrier wave $S_{carrier}(t_{AC}) = e^{-i\omega_c t_{AC}}$:

$$\begin{aligned}
S_{RF}(t_{AC}) &= Re\left\{M(\omega(t_{AC})) \cdot S_{carrier}(t_{AC})\right\} \\
&= Re\left\{e^{i\tau(\omega(t_{AC})-\omega(t_0))} \cdot e^{-i\omega_c t_{AC}}\right\} \\
&= Re\left\{e^{i\tau(\alpha\cdot t_{AC}+\beta-\alpha\cdot t_0-\beta)-i\omega_c t_{AC}}\right\} \\
&= Re\left\{e^{-i((\omega_c-\tau\alpha)t_{AC}+\tau\alpha\cdot t_0)}\right\} \\
&= \cos((\omega_c-\tau\alpha)t_{AC}+\tau\alpha\cdot t_0)
\end{aligned}$$

The acoustic frequency corresponding to a fixed delay τ can thus be calculated as $\omega_{RF} = \omega_c - \tau\alpha$. In practice this limits the range of time delays that can be generated, since the diffraction efficiency depends on the acoustic frequency, and is peaked at a certain value of ω_c. For a pulse shaper that is configured for the amplifier output using a TeO_2 modulator with $\nu_c \equiv \frac{\omega_c}{2\pi}$ =150 MHz, $\alpha \approx 2.45 \cdot 10^{-5}\frac{rad}{fs\cdot ns}$, the 3 dB points for the efficiency are at acoustic frequencies of ν_c±50 MHz, and the 50 MHz difference in frequency corresponds to $\tau \approx$13 ps time delay.

[1] A linear spectral phase will lead to an offset in time by virtue of the Fourier-shift theorem.

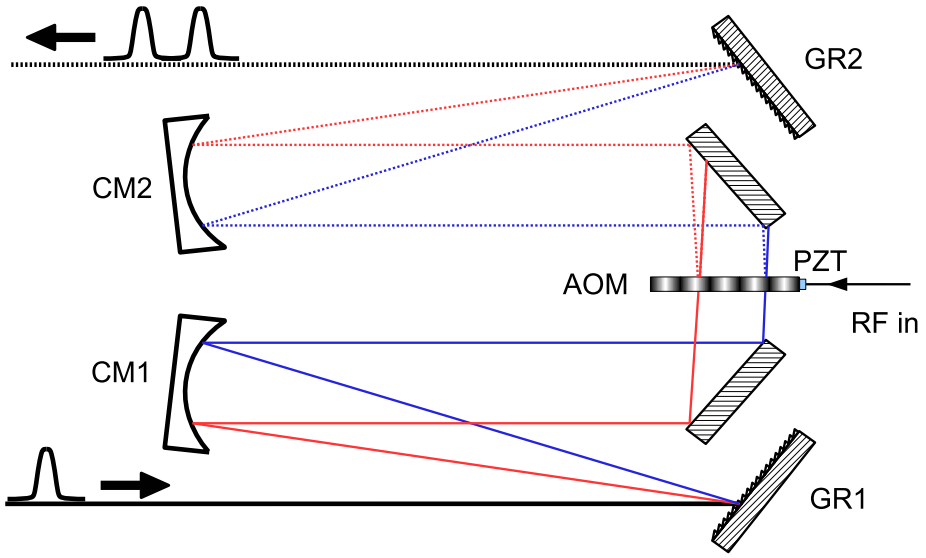

Figure 2.7: Optical setup of the 4-f pulse shaper. Solid lines show the incident and undiffracted beams, dashed line shows the diffracted beam. (The beam path for the undiffracted beam is not drawn beyond the first turning mirror following the AOM.) AOM: TeO_2 Acousto-Optic Modulator; PZT: piezoelectric transducer; GR1, GR2: plane ruled reflection gratings (670 lines/mm); CM1, CM2: curved dielectric mirrors (f = 75 cm).

2.4 Filamentation-based Source

As described in section 2.2, the only way to shorten the duration of a transform limited pulse is by adding new frequency components to the spectrum, and keeping the phase flat. New components can be added, for instance, by driving a nonlinear medium with sufficiently high intensity. To see how it works in principle, we first consider the optical Kerr-effect that adds an intensity-dependent term to the refractive index: $n(t) = n_0 + n_2 I_{env}(t)$. The intensity is given by: $I(t) = I_{env}(t)\cos^2(\phi(z,t))$ where $\phi(z,t) = kz - \omega_0 t = \frac{n(t)\omega_0}{c} z - \omega_0 t = (n_0 + n_2 I_{env}(t))\frac{\omega_0}{c} z - \omega_0 t$. The instantaneous angular frequency is given by the derivative of the phase: $\omega = -\frac{d\phi}{dt} = \omega_0 - n_2 z \frac{\omega_0}{c} \frac{dI_{env}(t)}{dt}$. There are two terms in this expression: the central frequency ω_0 and a correction added to it which sensitively depends on the derivative of the intensity envelope. This shows that depending on which instant in time we consider under the pulse envelope, the angular frequency can take on a range of values. The z-dependence also tells us that the longer the pulse propagates in the nonlinear medium, the larger the difference will be between the instantaneous and the central frequency. All these new frequencies contribute to the measured spectrum, broadening the distribution.

In the laboratory, spectral broadening was achieved by focusing the amplifier output into a vacuum tube backfilled with 1-1.5 atm of Argon gas. The high peak intensity in the focus leads to significant nonlinear response of the medium: modulation of the refractive index and ionization of the atoms. From the interplay of these two effects, a filament of laser-driven plasma is created, which has the potential to sustain itself over distances exceeding the Rayleigh length of the focused laser beam [20].

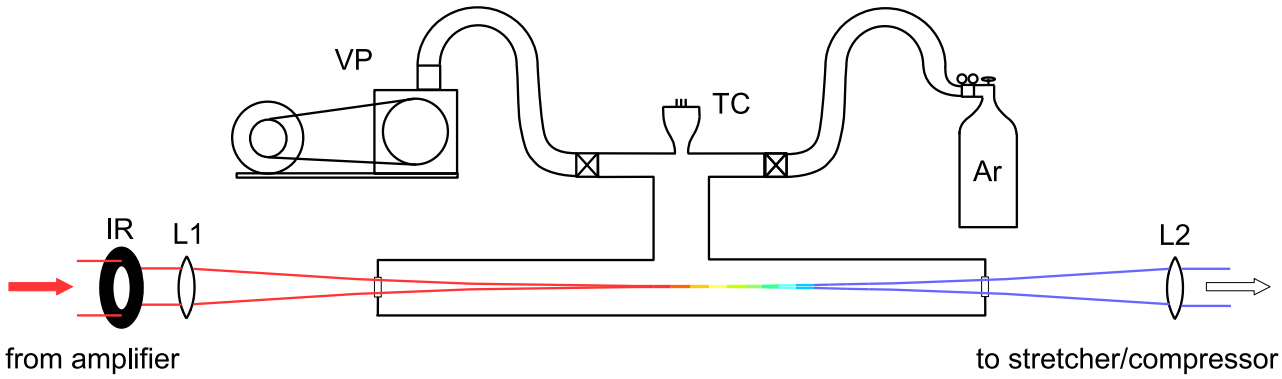

Figure 2.8: Optical setup and vacuum apparatus for the filamentation-based light source. L1, L2: lenses with $f = 1$ m; VP: mechanical (roughing) vacuum pump; TC: thermocouple gauge to monitor the pressure; IR: Iris

Dispersion control was accomplished with a grating stretcher–compressor built in 4-f configuration. The design is very similar to that of the pulse shaper (see section 2.3, with a few important modifications. First, the active element (the AOM) was removed; second, the optics were replaced with broadband metallic counterparts (silver or aluminium); and third, the dispersion of the gratings were reduced to accommodate the larger bandwidth. The amount of dispersion (positive or negative) written onto the pulse can be controlled by changing the grating separation.

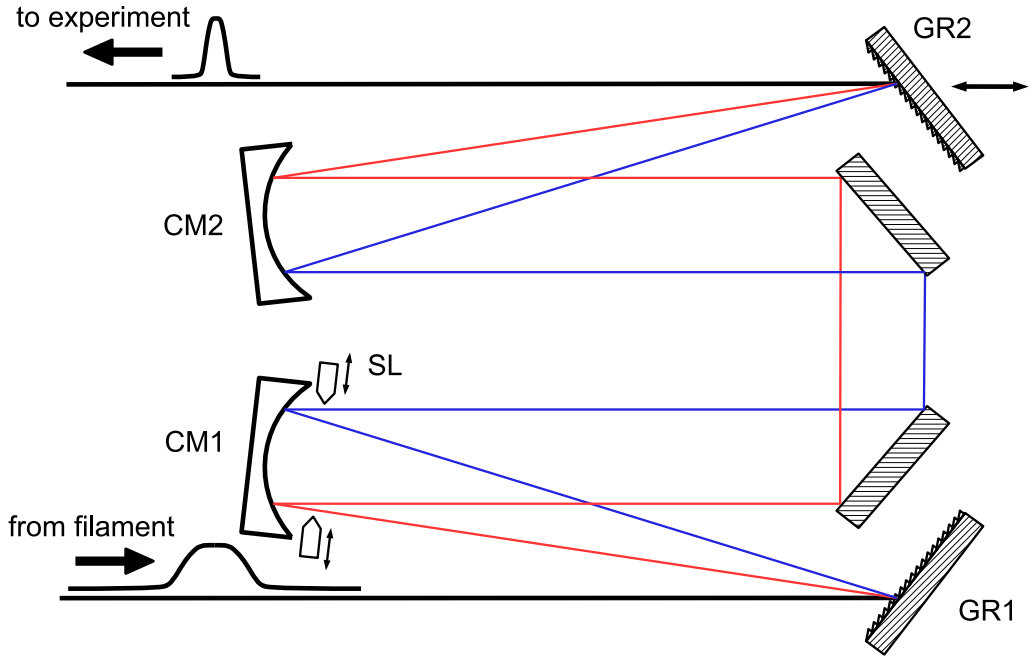

Figure 2.9: Optical setup of the 4-f grating stretcher/compressor. SL: Slit for bandwidth and central wavelength control; GR1, GR2: plane ruled reflection gratings (300 lines/mm, Al-coated); CM1, CM2: curved Ag-coated mirrors (f = 50 cm).

The broadest spectrum produced is capable of supporting sub-6 fs pulses, and FROG measurements place an upper limit on the duration of the full bandwidth pulses of about 8-9 fs, see figure 2.10. The spectrum can be cut using a variable slit in the grating compressor (see figure 2.9) in order to obtain the desired bandwidth. The spectrum of the pulse is adjusted at the focusing element instead of the Fourier

plane in order to avoid hard cutoffs at the edges of the spectrum, which would lead to a structured pulse in the time domain.

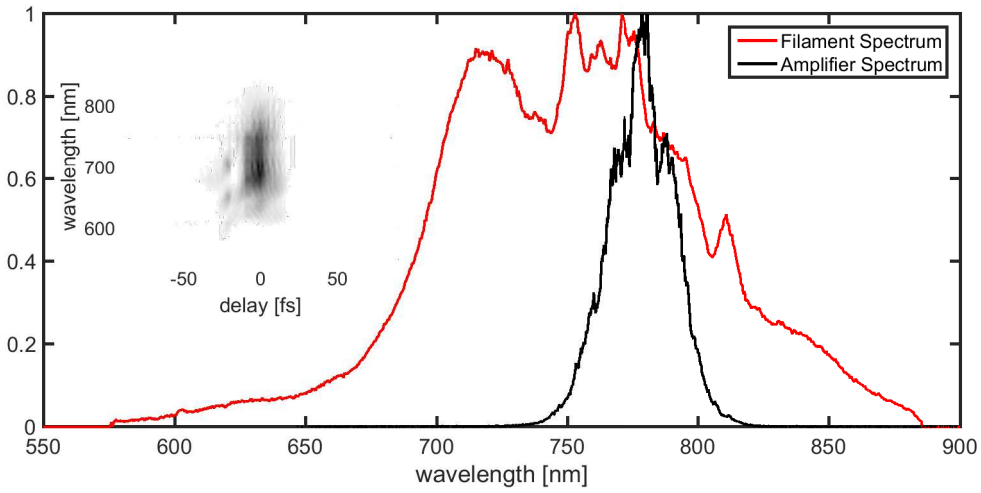

Figure 2.10: Optical spectra for the amplified beam (input to argon gas cell) and the filament (output of gas cell). Inset: self-diffraction FROG trace of a dispersion-compensated pulse from filamentation.

2.5 Velocity-Map Imaging (VMI) Apparatus for Ions and Electrons

Velocity map imaging is a charged-particle detection scheme in which ions or electrons that are generated in a small volume of space (e.g. in the focus of a laser beam) are imaged to a 2D position-sensitive detector according to their transverse velocity (or momentum) [21]. This is achieved by a static electric field configuration that acts as a lens (see figure 2.11).

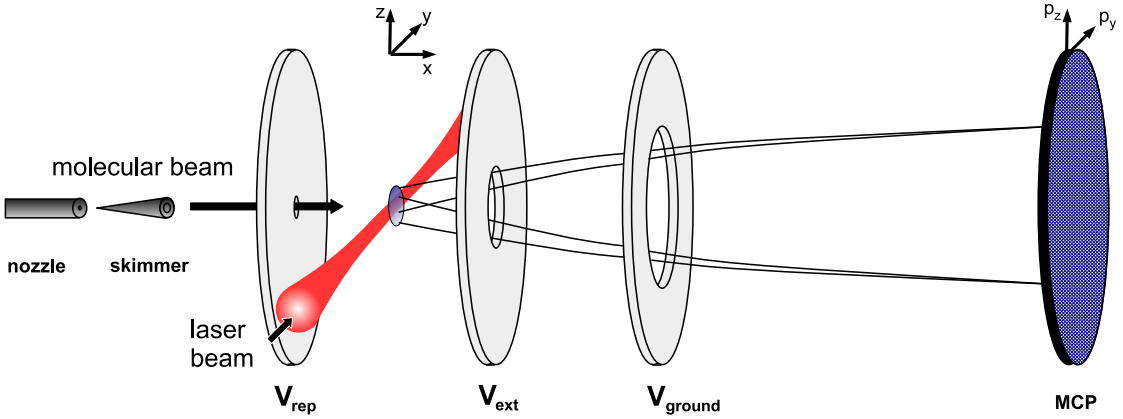

Figure 2.11: The geometry of velocity map imaging (VMI). The focused laser beam crosses the path of the effusive molecular beam. A set of electrostatically charged plates image the generated charged particles (ions and/or electrons) to a 2-dimensional position-sensitive detector according to the transverse momentum of the particles.

The signal is detected and digitized by an arrangement of a dual stack of MCPs in chevron configuration, a phosphor screen and a camera. The MCPs convert each of the incoming charged particles to a

well localized shower of electrons, effectively amplifying the signal. The phosphor screen converts these electrons to photons, and the camera images the phosphor screen to a CCD or CMOS chip. Both electrons and ions can be imaged with this setup, and information is retained about either the position of the individual hits or the distribution of the ensemble of charged particles reaching the detector. Electrons need additional shielding from external magnetic fields, and this is realized by enclosing the time-of-flight (TOF) tube with a cylinder made of a 250 μm thick μ-metal sheet (see figure 2.13).
The imaging apparatus is housed in a high vacuum chamber, with a base pressure of $5 \cdot 10^{-9}$ Torr. Sample molecules are delivered to the region where they interact with the laser pulse using an effusive molecular beam. The pressure in the chamber is monitored using a residual gas analyzer (Extorr XT200) and is set such that the partial pressure of the sample (all fragments combined) is at least an order of magnitude above the pressure of the background molecules (mostly H_2O - see figure 2.12). Further details of the vacuum system can be found in [22].

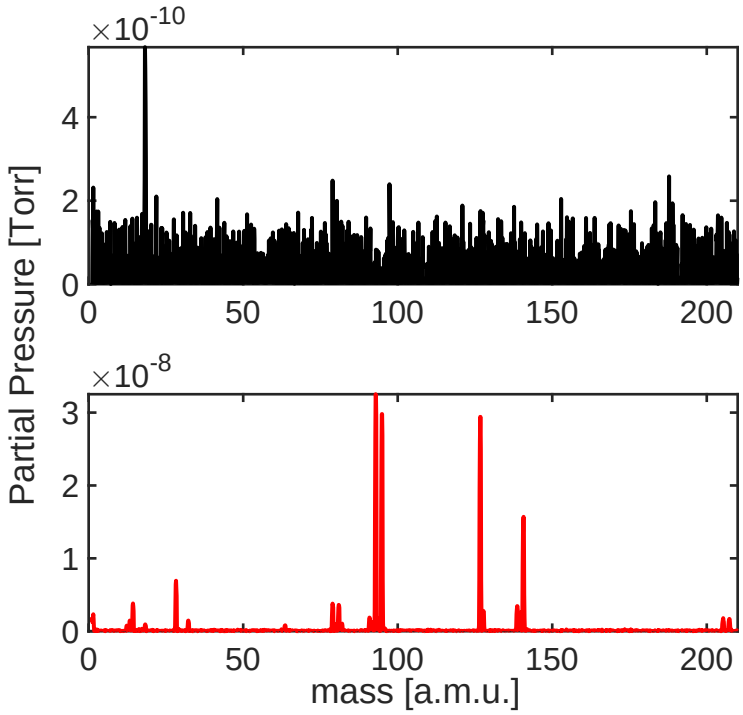

Figure 2.12: Signature of CH_2IBr parent and fragment ions on a typical RGA readout (bottom panel) and a typical background trace (top panel).

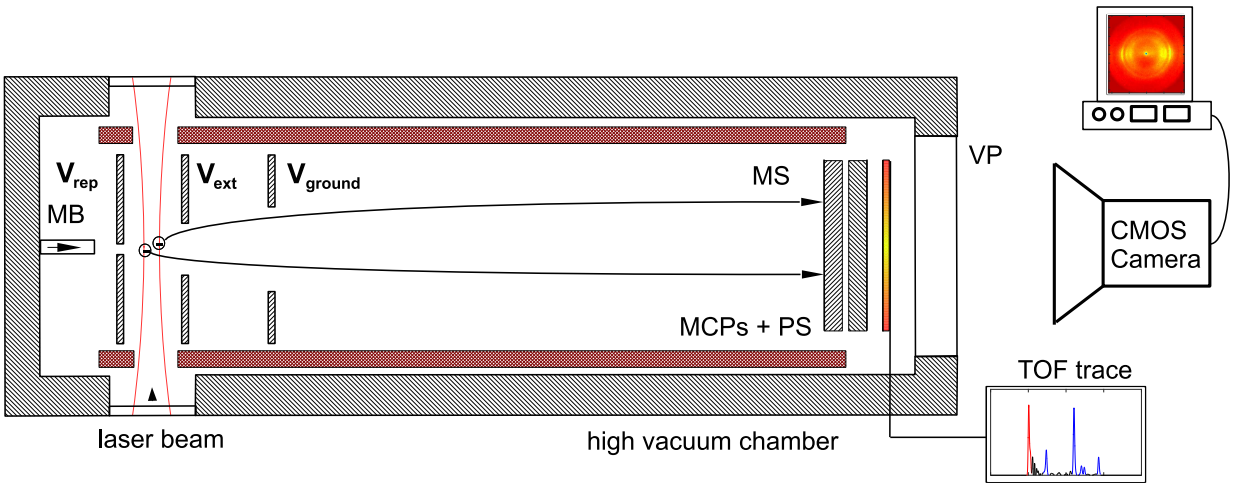

Figure 2.13: Schematic drawing of the VMI chamber. PS: Phosphor Screen; MS: μ-metal Magnetic Shielding; VP: Viewport; MB: Molecular Beam

Given the geometry of the repeller plates, setting up the electrostatic lens for optimal imaging is done by adjusting the ratio of V_{rep} and V_{ext} (the voltages on the repeller and extractor plates, respectively; V_{ground} is kept at 0 V) such that $\frac{V_{ext}}{V_{rep}} = 0.71 \pm 0.005$. It is worth noting that faithful imaging of the laser focus as a function of physical position ("spatial imaging") can be achieved by setting $\frac{V_{ext}}{V_{rep}} = 0.97$. The overall magnification of the image is determined by V_{rep} [21]. This can be understood by considering the charged particles leaving the lens and flying ballistically in the field-free region until they hit the MCPs at distance d. A higher V_{rep} will result in higher kinetic energy, and with it, higher longitudinal momentum ($m \cdot v_L$) imparted to the particles (we suppose that the transverse momentum ($m \cdot v_T$) doesn't change appreciably). This will lead to reduced flight times (t) and hence reduced distances for each hit from the center of the image (R). Expressing this, we can write:

$$R = t \cdot v_T$$
$$t = \frac{d}{v_L}$$
$$v_L = \sqrt{\frac{2qV_{rep}}{m}}$$

Where v_L is the longitudinal velocity, q is the charge of the particle. Substituting the latter two expressions to the one for R:

$$R = \frac{d_L}{\sqrt{2q}}\sqrt{\frac{m}{V_{rep}}}v_T \tag{2.2}$$

From this it is apparent that the imaging scales neither purely with momentum, nor with energy. Rather, it scales with square root of the part of the kinetic energy that is associated with transverse motion: $E \equiv \frac{1}{2}mv^2 \equiv \frac{1}{2}m(v_L^2 + v_T^2)$ and $E_T \equiv \frac{1}{2}mv_T^2$.
The photoelectron momentum distributions in most cases are converted to photoelectron spectra, i.e. to distributions of the yield as a function of kinetic energy. Steps of the conversion are discussed in detail in section 2.6; at this point some consideration is given to determining the energy axis calibration, or in other words asking, a given pixel corresponds to what energy value. This can in principle be done by rearranging equation 2.2. Taking the square of both sides and identifying $E_T \equiv \frac{1}{2}mv_T^2$:

$$E_T = \frac{qV_{rep}}{d^2}R^2 \tag{2.3}$$

The calibration constant $\frac{qV_{rep}}{d^2}$ can be experimentally determined by making use of the fact that photoelectron distributions obtained with multiphoton excitation show a series of concentric rings that are spaced by the photon energy (figure 2.14). These rings are the result of above-threshold ionization (ATI), during which electrons can absorb a discrete number of photons to get ionized, possibly more than it is necessary to reach a given continuum state. The excess leads to discrete features in the kinetic energy spectrum [23]. A calibration obtained in such a way is consistent with d=31 cm.

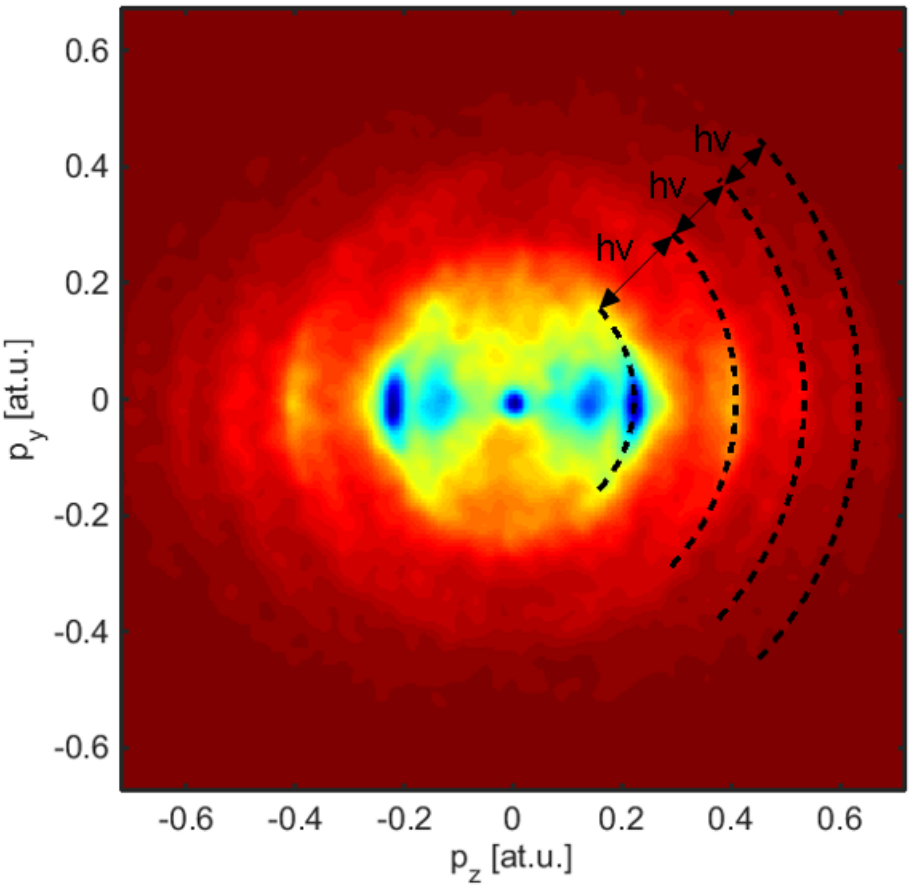

Figure 2.14: ATI rings observed in a raw VMI image of CH_2IBr. The laser pulse used in this experiment has 775 nm central wavelength and ≈30 nm bandwidth. V_{rep} = -1800 V.

While it is difficult to directly measure the resolution of the VMI apparatus given the lack of a tunable monoenergetic source of electrons, we can estimate a lower limit to the resolution based upon the size of a single electron hit on the detector - the $1/e^2$ diameter of such a hit is ≈2 pixels. Two such hits are just resolved if their centers are separated by twice this width, i.e. 4 pixels. The mapping of electron velocity to camera pixel is linear (≈5 km/s per pixel for V_{rep} = -600 V), however, the mapping of energy is quadratic, giving nonuniform resolution across the spectrum. E.g., at 0 eV, $\Delta E \approx 1$ meV; at 1 eV, ΔE ≈70 meV, and at 2 eV, ΔE ≈100 meV.

2.5.1 Noncoincident VMI

During VMI data acquisition that is not in coincidence with ions, all electrons are recorded on the same image, regardless of the ionization–dissociation channels that led to their production. Below two techniques are discussed which are used to record a raw image.

Data acquisition in aggregate mode

In this mode the camera exposure time is chosen such that the number of particles on each image is about 50 or more. In some cases this requires aggregating particle hits from multiple laser shots. Each image is individually saved to the hard drive and processed after acquisition is done.
Processing usually includes:

- Thresholding the images to eliminate background electronic noise of the detector chip of the camera
- Averaging the images
- Correct the images for nonuniformities of the detector gain

This technique has the advantage that it is relatively simple and flexible, allowing the experimenter to vary the laser parameters (i.e. intensity) in a broader range.

Data acquisition in counting mode

Limiting the number of hits recorded by the camera to <50 per image opens up the possibility of identifying and analyzing each of the hits individually. Images can be processed (either during of after data acquisition) such that each hit location is determined individually and only its coordinates are retained. From these coordinates an artificial image can be synthesized (figure 2.15). This artificial image is free from background noise because a threshold is applied to the raw image below which pixel values are set to zero. It is also free from the nonuniformities of the detector gain. The simple reason behind it is that while the detection efficiency does not vary appreciably across the detector, the size and signal level of a detected hit are correlated with the local gain of the MCP. The algorithm (major steps outlined below) disregards information both on the size and on the signal level when determining the hit locations. For synthesis, the same primitives (in our case, Gaussians of a fixed width and height) are placed at each location.

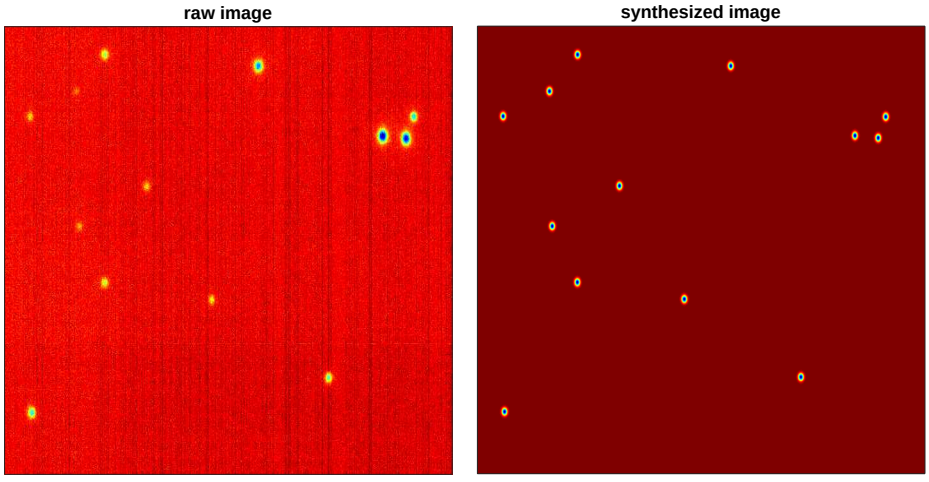

Figure 2.15: Left panel: portion of a raw VMI image showing electron hits. Right panel: synthesized image

Steps for obtaining a synthesized image include:

- Thresholding the images
- Clustering the pixels that have nonzero value after thresholding (i.e. determining which group of pixels belong to the same hit)
- Centroiding the clusters (i.e. determine the center coordinates of each group of pixels that constitute a hit)
- Using the obtained coordinates to synthesize the image, by placing a predetermined primitive (e.g. a 2D Gaussian of a given width and amplitude) on each coordinate. The width of the primitive is somewhat arbitrary, but in practice it can be chosen to match the size of a hit on a raw image.

Practically it is usually required to work at laser intensities close to the ionization threshold and record an image every laser shot. Working at a higher laser intensity is possible as long as the ionization yield is kept low enough such that hits on a single image don't overlap. This is usually achieved by lowering the number of molecules in the laser focus (equivalently, the sample pressure). Unfortunately, the dynamic range in the intensity that can be used in a measurement is rather limited due to the fact that the yield scales highly nonlinearly with intensity, but only linearly with pressure.

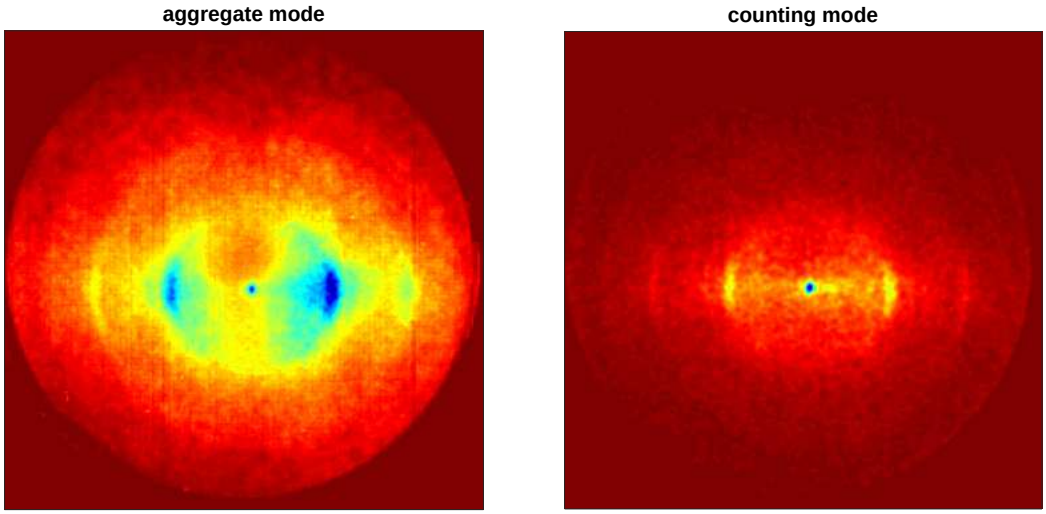

Figure 2.16: Comparison of two VMI images acquired with two different methods under the same experimental conditions. The image on the left panel was acquired in aggregate mode, and it is visibly affected by the nonuniformity of the detector gain close to the center of the distribution. The image on the right panel was acquired in counting mode.

2.5.2 Coincidence VMI of photoelectrons and photoions

During coincidence VMI data acquisition, electrons associated with different fragment ions are distinguished, and hence additional information becomes available with regards to the different ionization–dissociation pathways. Practically speaking, photoelectron momentum distributions corresponding to different fragments are recorded. In principle it is straightforward to carry this out if only a single photoelectron-photoion pair is generated and detected at every laser shot. Since both the generation and the detection are probabilistic in nature, some consideration has to be given to the other cases (i.e. when more than a single pair is generated), and how these affect the measured distributions - more on

this in section 2.5.2. Figure 2.17 shows the schematics of the experimental setup.

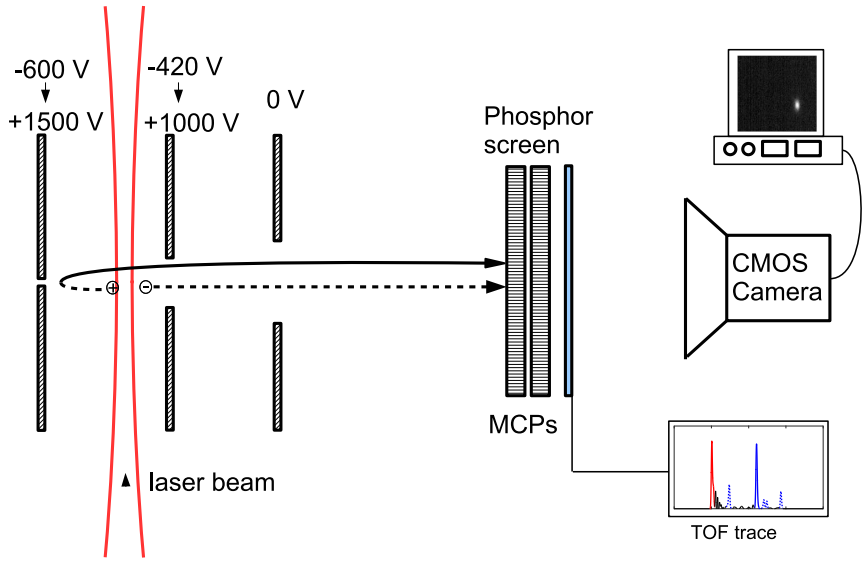

Figure 2.17: Schematics for coincidence data acquisition.

There are a number of ways to implement the coincidence detection scheme, some of which make use of imaging plate voltages that are held constant in time, and two detector elements, one for the electron and one for the ion [24]. Experiments in the present thesis are carried out with a scheme which uses a single detector element (similar to [25]), fast switching of the imaging voltages (V_{rep} and V_{ext}) following every laser shot, and a CMOS camera that is capable of short (24 μs) exposure times (Basler gigA2000 km340). Manipulating the high voltages is carried out by one or more fast high-voltage switches (IXYS Colorado PVX-4140 and PVX-4150). Owing to the mass of the electron being more than three orders of magnitude smaller than any of the fragment ions (implying a very short flight time to the detector, during which the ions hardly move), negative voltages are applied first to extract the electrons within tens of nanoseconds. The camera exposure ends at this point in time and an image is recorded with the photoelectrons. Then the voltages are switched to provide imaging for the ions, which are identified based on their time of flight (see figure 2.18). (Note that while the negative voltages are applied to image the electrons, the ions are flying the opposite direction, towards the back imaging plate. Some of the lighter fragments, for which the switching—which takes place in ≈200 ns—is not fast enough may end up hitting the back imaging plate and get lost.) At this point, the raw images are paired up with the TOF traces and further processing takes place to filter out the image + trace pairs that cannot correspond to a valid coincidence event.
A digital filter selects valid coincidence events based on the following criteria:

- The TOF trace should contain exactly two peaks: one for an electron hit and one for an ion hit.
- The image should contain exactly one hit (corresponding to an electron).

If both of these requirements are met, then the identifier for the fragment is paired up with the coordinates of the single electron hit. Aggregated over many laser shots, these valid coincidence events can be processed to produce a raw photoelectron VMI image for each fragment observed. Other valuable statistical information can be also extracted, for example branching ratios for the different fragments.

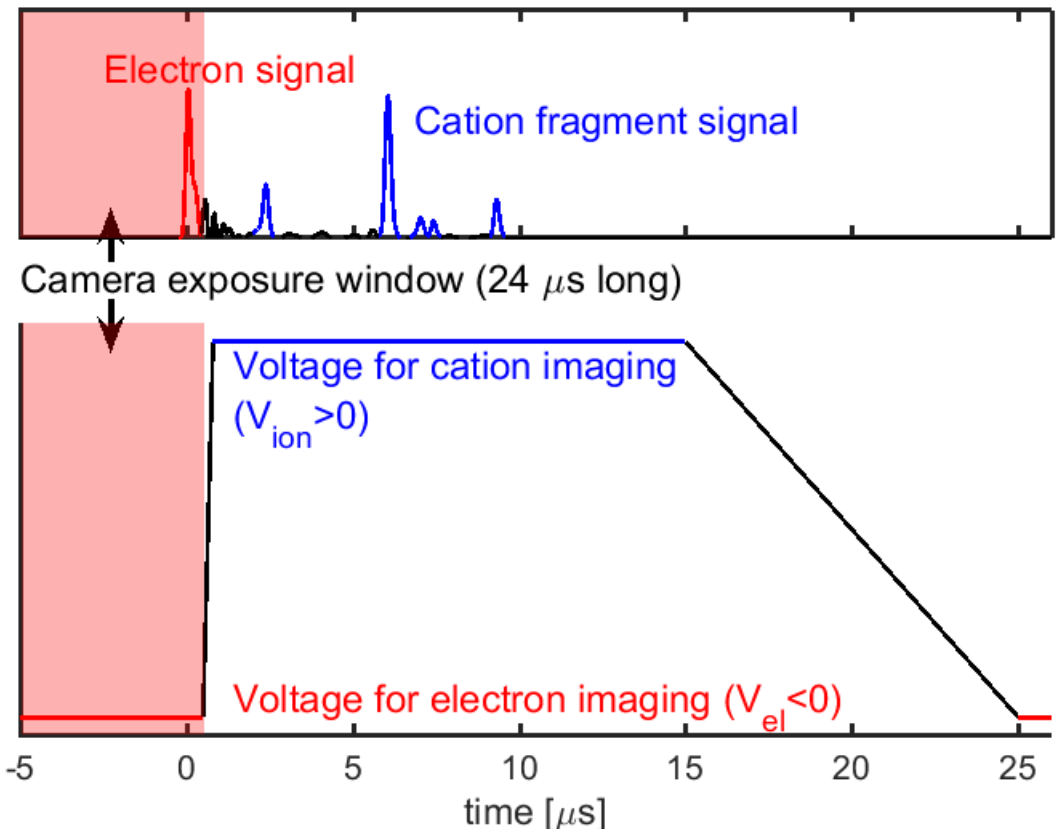

Figure 2.18: Timing diagram showing a typical measured TOF trace (upper panel) along with time dependence of the electrostatic lens voltage (lower panel) and the camera exposure window (red shading). The 10%-to-90% voltage switching time is $\approx$ 100 ns.

Data acquisition runs at 1 kHz, the repetition rate of the laser. However, due to the relatively low detection efficiencies (especially for heavy fragments) and also due to statistical considerations (see section 2.5.2), the actual rate at which coincidences occur (either valid or false), is usually below 100 Hz (strongly pulse shape and molecule dependent).
An estimate of the microchannel plate detector efficiency (as a function of particle mass and kinetic energy) for heavy (>100 a.m.u.) ions can be found in [26]. Using equation (26) in this reference, a kinetic energy of 1 keV and an open area ratio of 55% for the MCPs, the detection efficiencies of the cationic fragments are estimated, and in case of the data shown in chapter 3, their ratio is used to correct the relative yields of the coincidence photoelectron spectra. For a fixed longitudinal accelerating voltage of 1 kV, the values are spread between 5 and 50%, depending on the mass of the fragment. For electrons, using 0.6 kV for acceleration, the overall detection efficiency is about 50%. As an example for cations of halomethanes relevant to this thesis, the values are 24% for CH_2Br^+, 7% for CH_2IBr^+, 45% for CH_2Cl^+ and 15% for CH_2BrCl^+.

Coincidence statistics

In the ideal case when the detection efficiency is 100% for both ions and electrons, all valid coincidences are true coincidences, meaning that the detected electron and ion originated from the same ionization–dissociation event. However, if the efficiency is lower, then false coincidences can occur; the simplest example of this is when two molecules get ionized in the laser focus, dissociate to different fragments,

and the fragment from one of these processes gets detected along with the electron from the other.
We can estimate the ratio of true and false coincidences if we assume that the number of generated electron-ion pairs per laser shot exhibits a Poisson distribution with the expectation value λ and the number of occurrences k :

$$P(k,\lambda) = \frac{\lambda^k e^{-\lambda}}{k!} \tag{2.4}$$

Assuming a single species of ions (for example, if no fragmentation can take place), then the probability of generating k electron-ion pairs, and detecting exactly m electrons and l ions can be expressed as follows:

$$P(l,m,k,\lambda) = \underbrace{\frac{\lambda^k e^{-\lambda}}{k!}}_{\text{generate 'k' pairs}} \cdot \underbrace{\binom{k}{m} p^m (1-p)^{k-m}}_{\text{detect 'm' electrons}} \cdot \underbrace{\binom{k}{l} q^l (1-q)^{k-l}}_{\text{detect 'l' ions}} \tag{2.5}$$

where the electron and ion detection efficiencies are denoted by *p* and *q*, respectively.

In case multiple species of the ions have to be taken into account (i.e. we allow for fragmentation), the above formula can be generalized by considering the set of branching ratios b_j, detection efficiencies q_j, generated and detected quantities n_j and l_j, respectively. The number of possible fragment types is assumed to be N.

$$P(\{n_j\},\{l_j\},m,k,\lambda) = \frac{\lambda^k e^{-\lambda}}{k!}\binom{k}{m} p^m (1-p)^{k-m} \binom{k}{n_1 \cdots n_N} \prod_{j=1}^{N} b_j^{n_j} \binom{n_j}{l_j} q_j^{l_j} (1-q_j)^{n_j - l_j} \tag{2.6}$$

where $\binom{k}{m}$ and $\binom{k}{n_1 \cdots n_N}$ are the binomial and multinomial coefficients, respectively.
Furthermore, $\sum_{j=1}^{N} b_j = 1$, $\sum_{j=1}^{N} n_j = k$ and l_j is an integer in the range $[0, n_j]$. Note that in the special case when one of the branching ratios is 1 for a specific species and vanishes for all the others, expression 2.6 simplifies to 2.5.
Formula 2.6 is very general, and in most cases it is enough to consider two species (or fragments) for the ions: the parent and the most abundant fragment. This means we can set $N = 2$, and have b_p, q_p, n_p and l_p denote the quantities for the parent, while b_f, q_f, n_f and l_f do the same for the fragment. Of course in this special case $b_p + b_f = 1$, $n_p + n_f = k$.

$$\begin{aligned} P(n_p,n_f,l_p,l_f,m,k,\lambda) = {} & \frac{\lambda^k e^{-\lambda}}{k!}\binom{k}{m} p^m (1-p)^{k-m} \\ & \cdot \binom{k}{n_p, n_f} \cdot b_p^{n_p} \binom{n_p}{l_p} q_p^{l_p} (1-q_p)^{n_p - l_p} \cdot b_f^{n_f} \binom{n_f}{l_f} q_f^{l_f} (1-q_f)^{n_f - l_f} \end{aligned} \tag{2.7}$$

Using formula 2.7, various important quantities can be calculated, such as the probabilities of true and false coincidences, and examine under which conditions their ratio is acceptable. We begin by expressing the probability of all coincidences. A coincidence in the strictest sense of the word is when exactly one electron and one ion are detected; however, they may or may not originate from the same molecule.

$$\begin{aligned} P_{coinc} = \sum_{k=1}^{\infty} \Bigg(& \sum_{n_p=\mathbf{0}}^{\boldsymbol{k\text{-}1}} P(n_p, n_f = k - n_p, l_p = \mathbf{0}, l_f = \mathbf{1}, m = 1, k, \lambda) \\ & + \sum_{n_p=\mathbf{1}}^{\boldsymbol{k}} P(n_p, n_f = k - n_p, l_p = \mathbf{1}, l_f = \mathbf{0}, m = 1, k, \lambda) \Bigg) \end{aligned} \tag{2.8}$$

Here the first term in the parentheses corresponds to detecting a fragment, the second corresponds to detecting a parent in coincidence with an electron.
A subset of all coincidences are true coincidences, in which case exactly one electron and one ion are detected, and they originate from the same molecule. Ultimately these are the events that we set out to measure. Given k generated pairs, the number of possible detected pairs that satisfy this criterion is reduced by a factor of $\frac{1}{k}$.

$$P_{true} = \sum_{k=1}^{\infty} \frac{\mathbf{1}}{\boldsymbol{k}} \left(\sum_{n_p=\mathbf{0}}^{\boldsymbol{k\text{-}1}} P(n_p, n_f = k - n_p, l_p = \mathbf{0}, l_f = \mathbf{1}, m = 1, k, \lambda) + \sum_{n_p=\mathbf{1}}^{\boldsymbol{k}} P(n_p, n_f = k - n_p, l_p = \mathbf{1}, l_f = \mathbf{0}, m = 1, k, \lambda) \right) \tag{2.9}$$

Because of technical reasons, for the discussions of coincidence in the subsequent paragraphs the condition on the number of ions detected has to be relaxed, and the probability of all *detected* coincidences has to be introduced. The definition of this is to detect one electron and any number of ions, provided these latter are all the same type (either only parent or only fragment). The reason behind it is that in a TOF measurement, one cannot tell how many fragments of the same type contribute to a peak.

$$P_{all} = \sum_{k=1}^{\infty} \left(\sum_{n_p=\mathbf{0}}^{\boldsymbol{k\text{-}1}} \sum_{\boldsymbol{l_f}=1}^{\boldsymbol{n_f}} P(n_p, n_f = k - n_p, l_p = \mathbf{0}, \boldsymbol{l_f}, m = 1, k, \lambda) + \sum_{n_p=\mathbf{1}}^{\boldsymbol{k}} \sum_{\boldsymbol{l_p}=1}^{\boldsymbol{n_p}} P(n_p, n_f = k - n_p, \boldsymbol{l_p}, l_f = \mathbf{0}, m = 1, k, \lambda) \right) \tag{2.10}$$

All detected coincidences are sorted into two categories: valid and false ($P_{all} = P_{valid} + P_{false}$). Valid coincidences however, though not "true", still result in useful data. In this case, exactly one electron and any number of ions are detected, and though they may not come from the same molecule, the fragment (or fragments) is (are) all the same type as the electron's "true" partner.

$$P_{valid} = \sum_{k=1}^{\infty} \frac{\mathbf{1}}{\boldsymbol{k}} \left(\sum_{n_p=\mathbf{0}}^{\boldsymbol{k\text{-}1}} \sum_{\boldsymbol{l_f}=1}^{\boldsymbol{n_f}} \boldsymbol{n_f} \cdot P(n_p, n_f = k - n_p, l_p = \mathbf{0}, \boldsymbol{l_f}, m = 1, k, \lambda) + \sum_{n_p=\mathbf{1}}^{\boldsymbol{k}} \sum_{\boldsymbol{l_p}=1}^{\boldsymbol{n_p}} \boldsymbol{n_p} \cdot P(n_p, n_f = k - n_p, \boldsymbol{l_p}, l_f = \mathbf{0}, m = 1, k, \lambda) \right) \tag{2.11}$$

For the fragment, the number of cases is increased by n_f, for the parent, by n_p, compared to the true coincidences (because one has that many more electrons to choose from), and the cases for the different number of detected ions also have to be added up. The first term in the parentheses corresponds to valid coincidences involving the fragment ion, the second term is the same for the parent ion.
False coincidences then are complementary to the valid ones: exactly one electron and any number of ions are detected, and the fragment (or fragments) is (are) the same type but different than the electron's "true" partner.

$$P_{false} = \sum_{k=1}^{\infty} \frac{\mathbf{1}}{\boldsymbol{k}} \left(\sum_{n_p=1}^{k-1} \sum_{\boldsymbol{l_f}=1}^{\boldsymbol{n_f}} \boldsymbol{n_p} \cdot P(n_p, n_f = k - n_p, l_p = \mathbf{0}, \boldsymbol{l_f}, m = 1, k, \lambda) + \sum_{n_p=1}^{k-1} \sum_{\boldsymbol{l_p}=1}^{\boldsymbol{n_p}} \boldsymbol{n_f} \cdot P(n_p, n_f = k - n_p, \boldsymbol{l_p}, l_f = \mathbf{0}, m = 1, k, \lambda) \right) \tag{2.12}$$

The first term in the parentheses correspond to false coincidences involving the fragment ion and an electron from the parent, the second term is the same for the parent ion and an electron from the fragment. Calculated values for the probabilities are shown on figure 2.19 for a typical coincidence experiment carried out on CH_2IBr as a function of the expectation value for the generated pairs, λ. The parameters for the parent ion are $b_p = 0.23$ and $q_p = 0.07$; for the most abundant fragment, CH_2Br^+ these are $b_f = 0.77$ and $q_f = 0.24$. For the electrons, $p = 0.5$. Experiments were conducted with $\lambda \approx 0.6$, at which point 94% of coincidences are valid.

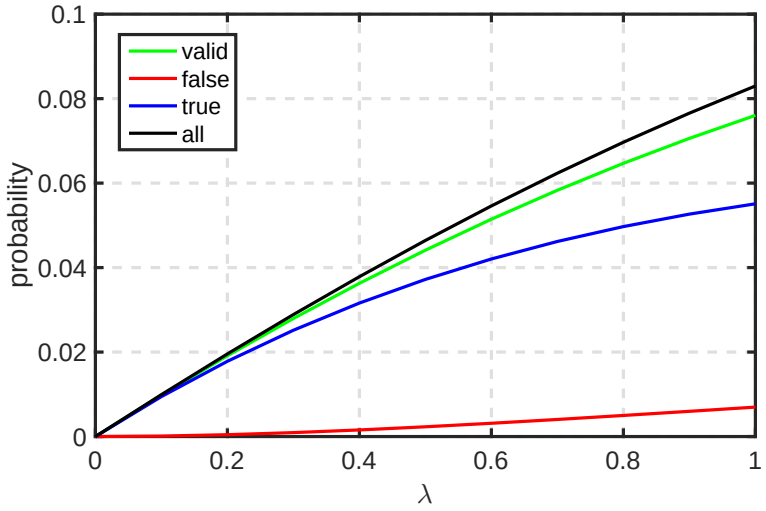

Figure 2.19: Coincidence probabilities for a typical experiment on CH_2IBr.

2.6 VMI Data Processing

A VMI image is essentially a discrete function of two variables *i* and *j*, where each index pair (*i*,*j*) represents a pixel on the image, and *P(i,j)* is the value of a given pixel. We assume that each hit on the image (due to either an electron or an ion) is represented by a number of pixels with a sum of the values for these pixels equal to one:

$$\sum_{pixels\ of\ a\ hit} P(i,j) = 1$$

Then, assuming 100% detection efficiency, one can say that all electrons are extracted from the interaction region (where photoionization took place due to the focused laser beam), each of them hit the 2D detector and were recorded by the camera. The number of electrons can be calculated by summing up the values of all pixels in the image:

$$\sum_{all\ pixels} P(i,j) = N_{tot}$$

For the following discussion, it is more convenient to use continuous variables instead of discrete ones. Associating each pixel with a center location, described by a coordinate pair in momentum space (p_y,p_z) and widths (dp_y,dp_z), we can turn the discrete sum to a double integral:

$$\int\int \eta(p_y,p_z)dp_y dp_z = N_{tot}$$

where $\eta(p_y,p_z)$ is the density, such that $\eta(p_y,p_z)dp_y dp_z = P(i,j)$ if (p_y,p_z) and (*i*,*j*) refer to the same location on the camera.

It is assumed that the 3D electron cloud (that was created in the laser focus) possesses cylindrical symmetry and hence the 3D distribution can be described with only two variables: (p_ρ,p_z). It is a reasonable assumption in case the laser field is linearly polarized (with the axis of the cylinder being the laser polarization axis), and the laser pulse envelope is long enough to contain more than a few optical cycles. A single quadrant of the raw images then contains all the information that can be obtained in the measurement, and hence data from all four quadrants can be added up ("folded" onto one quadrant) to increase signal-to-noise.
The next step is to apply Abel-inversion. Taking advantage of the cylindrical symmetry again, the full 3D distribution can be reconstructed in momentum space from the 2D distribution ($\eta(p_y, p_z) \xrightarrow{Abel-invert} \zeta(p_\rho, p_z)$). The geometry is illustrated in figure 2.20.

$$\zeta(p_\rho, p_z) = -\frac{1}{\pi} \int_{p_\rho}^{\infty} \frac{\partial \eta}{\partial p_y} \frac{dp_y}{\sqrt{p_y^2 - p_\rho^2}} \tag{2.13}$$

Note that the inverse-Abel transformation as given in eq. 2.13 couples the p_x and p_y variables ($p_\rho^2 = p_x^2 + p_y^2$), but not p_z, which then can be treated as a parameter. The transformation should be then performed in planes of (p_x, p_y) for every p_z.

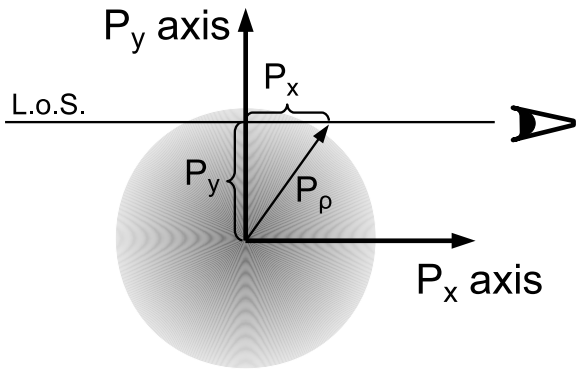

Figure 2.20: A geometrical interpretation of the Abel transform in two dimensions. An observer looks along a line parallel to the p_x-axis a distance p_y above the origin (Line of Sight - L.o.S.). The observer sees the projection (i.e. the integral along p_x) of the circularly symmetric function $\zeta(p_\rho, p_z)$ (for a given value of p_z; function is represented in gray) along the line of sight onto p_y. The observer is assumed to be located infinitely far from the origin so that the limits of integration are $\pm\infty$.

Numerical implementation of the inversion can be done in a number of different ways, all of which have strengths and weaknesses in terms of accuracy, speed and robustness to noise. Apart from straightforward evaluation of eq. 2.13, other algorithms worth noting are the BASEX [27], pBASEX [28] and Onion Peeling [29] methods, of which the BASEX approach was mostly used in chapters 3 and 4 of this thesis.

The total electron yield can then be evaluated from the original distribution in the cylindrical coordinate system:

$$N_{tot} = \int_0^{+\infty} \int_{-\infty}^{+\infty} \int_0^{2\pi} \zeta(p_\rho, p_z) p_\rho d\phi \, dp_z \, dp_\rho$$

Given the usually circular nature of the raw detected 2D distributions and the underlying spherical nature of the 3D electron cloud, one can choose to further transform the coordinate system to be spherical:

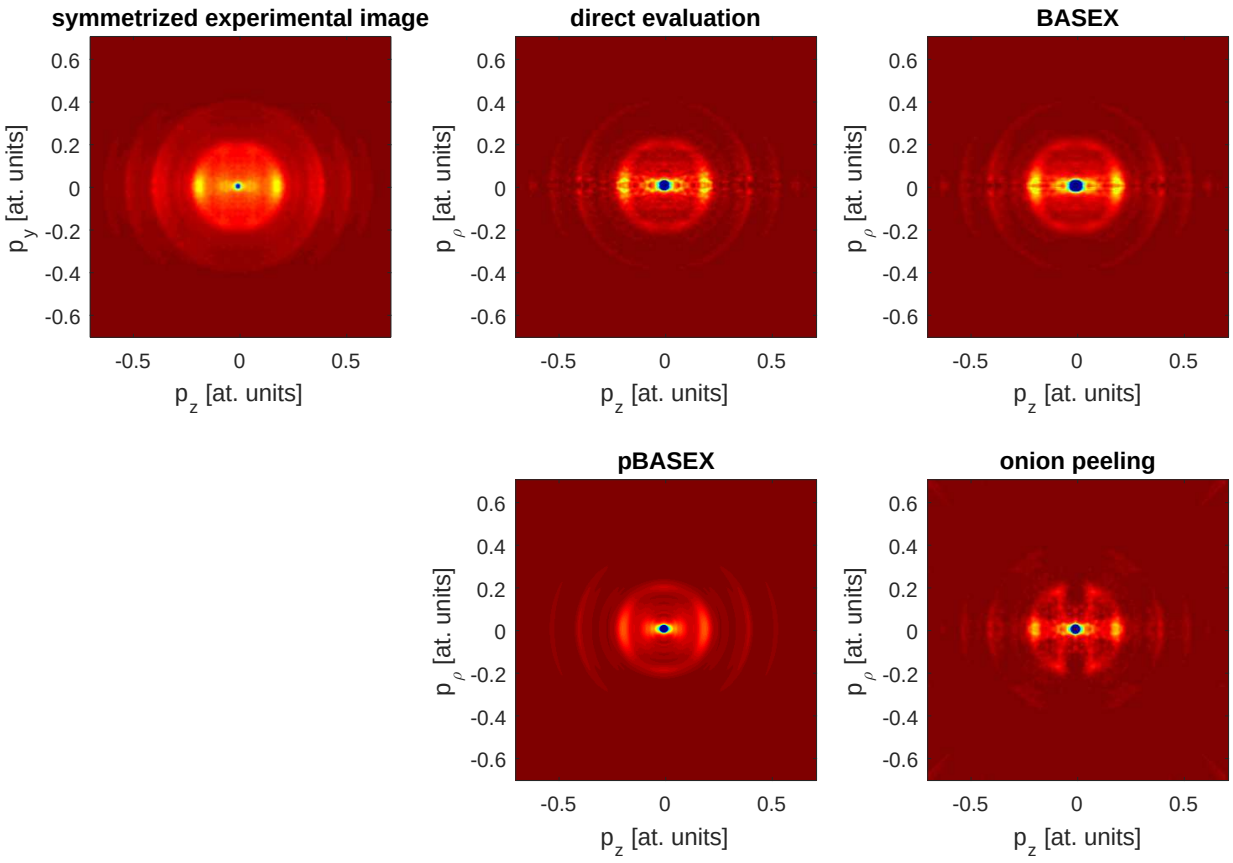

Figure 2.21: Comparison of different methods for performing Abel-Inversion. First image shows an experimentally obtained, symmetrized $\eta(p_y, p_z)$, the rest show $\zeta(p_\rho, p_z)$ that were calculated from that as an input.

(p_ρ,p_z,ϕ) $\rightarrow$ (p_r,θ,ϕ). The guiding principle, as always, is that the total number of electrons must be conserved. This will affect the functional forms of the distributions expressed in cylindrical and spherical coordinates, which, in general, will be different. The difference in form will mathematically manifest as a multiplication factor—the Jacobian—which can be calculated as follows:

$$p_\rho = p_r \cdot sin(\theta) \tag{2.14}$$

$$p_z = p_r \cdot cos(\theta) \tag{2.15}$$

$$J(p_\rho, p_z; p_r, \theta) = \begin{vmatrix} \frac{\partial p_\rho}{\partial p_r} & \frac{\partial p_\rho}{\partial \theta} \\ \frac{\partial p_z}{\partial p_r} & \frac{\partial p_z}{\partial \theta} \end{vmatrix} = \begin{vmatrix} sin(\theta) & p_r \cdot cos(\theta) \\ cos(\theta) & -p_r \cdot sin(\theta) \end{vmatrix} = p_r \cdot (\sin^2\theta + \cos^2\theta) = p_r$$

Which means $\zeta(p_\rho, p_z) = p_r \cdot \xi(p_r, \theta)$, and hence:

$$N_{tot} = \int_0^{+\infty} \int_{-\infty}^{+\infty} \int_0^{2\pi} \zeta(p_\rho, p_z) p_\rho d\phi \, dp_z \, dp_\rho \tag{2.16}$$

$$= \int_0^{+\infty} \int_0^{\pi} \int_0^{2\pi} \xi(p_r, \theta) \, p_r sin(\theta) d\phi \, p_r d\theta \, dp_r \tag{2.17}$$

In order to obtain the radial momentum distribution $\xi_{rad}(p_r)$, the integration with respect to p_r simply needs to be omitted. Since the distribution is cylindric, integration with respect to ϕ will yield an

unimportant factor of 2π.

$$\xi_{rad}(p_r) = \int_0^{\pi} \int_0^{2\pi} \xi(p_r, \theta)\, p_r^2 sin(\theta) d\phi\, d\theta \tag{2.18}$$

$$= 2\pi \cdot \int_0^{\pi} \xi(p_r, \theta)\, p_r^2 sin(\theta)\, d\theta \tag{2.19}$$

The photoelectron spectrum $S(E)$ is obtained by performing a final transformation on $\xi_{rad}(p_r)$, where as a first step $p_r = \sqrt{2mE}$ has to be substituted. However, similarly to the previous transformations, not just the x-, but also the y-axis has to be transformed, using the appropriate Jacobian: $dp_r = \sqrt{\frac{m}{2E}} dE$.

$$N_{tot} = \int_0^{\infty} \xi_{rad}(p_r) dp_r \tag{2.20}$$

$$= \int_0^{\infty} \xi_{rad}(\sqrt{2mE}) \sqrt{\frac{m}{2E}} dE \tag{2.21}$$

$$\equiv \int_0^{\infty} S(E) dE \tag{2.22}$$

So in the end:

$$S(E) \propto \frac{\xi_{rad}(\sqrt{2mE})}{\sqrt{E}} \tag{2.23}$$

Illustration of the different steps of the processing is shown on fig 2.22.

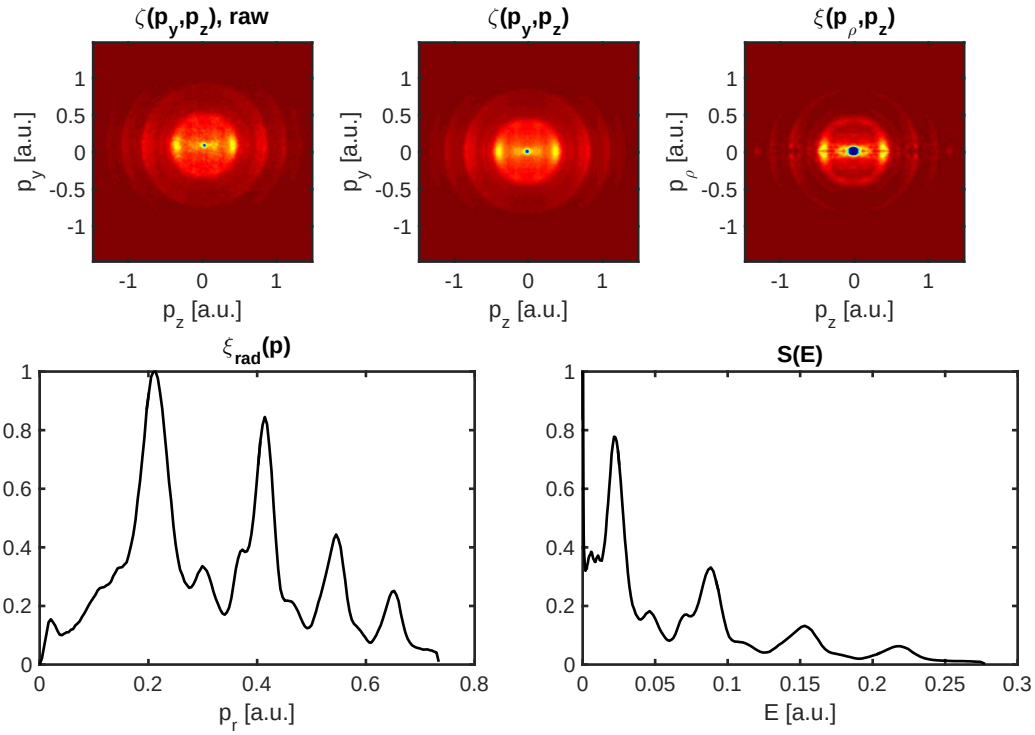

Figure 2.22: Sequence of the steps during VMI data processing.

Chapter 3

Molecular SFI - Direct and Indirect Pathways

3.1 Introduction

As mentioned in chapter 1, Strong Field Ionization is a sensitive probe of molecular dynamics and is a key underlying process of high harmonic generation and attosecond pulse generation. Its importance is well matched by its complexity: the strong laser field drives transitions from the neutral ground to possibly multiple ionic states, and to any one of these ionization may proceed via multiple channels. Though not strictly part of the ionization step per se, a molecule can also dissociate after it already has transitioned to an ionic state. Mapping out these ionization–dissociation pathways and their relative importance as a function of external field parameters is one of the main objectives of strong field physics.

As far as tools go, a number of things make such an endeavor feasible. Charged-particle imaging and detection schemes for photoions and photoelectrons are key components of most experiments. However, astonishingly powerful techniques are born from the coupling of the two, giving rise to a family of photoion-photoelectron coincidence imaging techniques. Coincidence VMI was introduced in section 2.5.2; other techniques offer even more selectivity. These are the Cold Target Recoil Ion Momentum Spectroscopy (COLTRIMS [30]) and the Reaction Microscope [31], which enable the full reconstruction of 3D momenta of all the ions and electrons after a many-body breakup process. Their application goes beyond atomic and molecular physics to study collision events involving other elementary particles (e.g. antiprotons, positrons).

In terms of physical pictures, strong-field physicists get themselves oriented by relying on the following two:

The *multiphoton picture*, as the name suggests, is the perturbative extension of the idea of ionizing with a single photon. The electromagnetic field is quantized, and multiple photons can be absorbed by an electron to overcome the energy barrier to ionization. The difference between the amount of energy absorbed from the field and the barrier will be carried away by the electron as translational kinetic energy.[1] When absorbing even more photons than minimally required for an electron to break free, distinct features called above threshold ionization (ATI) peaks appear in the photoelectron spectrum. This picture is usually applicable to modest to strong fields, and short wavelengths.

Tunnel ionization refers to a quasistatic picture in which the evolution of the electron wavefunction takes place in the binding potential on a shorter timescale than the laser period. The external field is thought of as classical, and strong enough to tilt the potential such that the electron can tunnel through it. Since buildup of appreciable portion of electron wavefunction usually takes place during multiple

[1] Here I refer to the barrier as a collective term including the weak field ionization potential of the atom or molecule in question.

tunneling "attempts" (each of which possess finite but small probability), the frequency of laser radiation is required to be much lower than the tunneling frequency.

Based on the considerations above, experiments can be crudely classified using a unitless parameter introduced by Keldysh [32], taken as the ratio of the optical frequency and the tunneling frequency:

$$\gamma = \frac{\omega_{laser}}{\omega_{tunnel}} = \frac{\sqrt{m_e I_p}}{q} \frac{\omega_{laser}}{E_0}$$

where m_e and q are the electron mass and charge, respectively, I_p is the ionization potential of the atom or molecule, E_0 is the peak electric field of the laser. $\gamma \gg 1$ suggests the validity of the multiphoton, and $\gamma \ll 1$ of the tunnel picture. In between the two is a regime where one can usually expect to see characteristics of both, and that is where experiments in this thesis are conducted ($\gamma \approx$1-2).

By interpreting photoelectron spectra collected in coincidence with the photoion fragments of CH_2IBr and CH_2BrCl, the different ionization–dissociation pathways are classified and the importance of neutral and ionic resonances is demonstrated during strong-field ionization.

3.2 Results

Figures 3.1 and 3.2 show the photoelectron spectra measured in coincidence with the two most prominent ionic fragments for two different molecules (CH_2IBr and CH_2BrCl) from the family of halomethanes. The photoelectron spectrum measured in coincidence with the parent ion is plotted with black solid line, while the spectrum for the most abundant fragment is plotted with blue dashed line on each figure; the most prominent fragments are CH_2Br^+ in the case of CH_2IBr and CH_2Cl^+ in the case of CH_2BrCl. Linearly polarized, transform limited pulses with a duration of 30 fs were used for the experiment. For strong field ionization of molecules with several low lying continua with comparable ionization potentials (such as the ones considered in this chapter, see table 3.1), one may expect significant structure in the low energy photoelectron spectrum. The kinetic energy of electrons ionized to the i^{th} continuum is given by:

$$K^i = nh\nu - I_p^i - U_p - E_{DSS}^i \tag{3.1}$$

where $h\nu$ is the energy of a single photon (typically 1.6 eV in these experiments - see discussion below), I_p^i is the ionization potential associated with the i^{th} continuum (or ionic state), U_p is the ponderomotive potential and E_{DSS}^i is the dynamic Stark-shift of the i^{th} ionic state. This equation is simply a statement about the conservation of energy and it is the extension of Einstein's famous formula describing the photoelectric effect in the weak field limit: $K = h\nu - W$. Equation 3.1 is valid in case of strong electric fields as well, involving possibly multiphoton transitions to the continuum. As a second term, the ionization potential for a specific ionic state I_p^i enters instead of the 'work function' *W*. The last two terms, U_p and E_{DSS}^i are not present in Einstein's formula, and can clearly be attributed to strong-field effects. Based on detailed calculations/measurements of each of these terms, the peaks in the coincidence spectra can be assigned to a specific continuum.

Details concerning the estimate of the two terms, I_p^i and E_{DSS}^i can be found in [33]. Briefly, the ionization potentials (I_p^i) for the five lowest-lying ionic continua for both molecules were determined using *ab initio* electronic structure calculations, the results of which are summarized in table 3.1.

To estimate the magnitude of dynamic Stark shifts (E_{DSS}^i), the time-dependent Schrödinger equation was integrated numerically, including the neutral ground state and the five lowest-lying ionic continua of CH_2BrCl. The continua were coupled by a strong infrared field, resulting in the Stark-shifts of interest. The ionic states were additionally coupled to the neutral ground state with a weak, tunable VUV field;

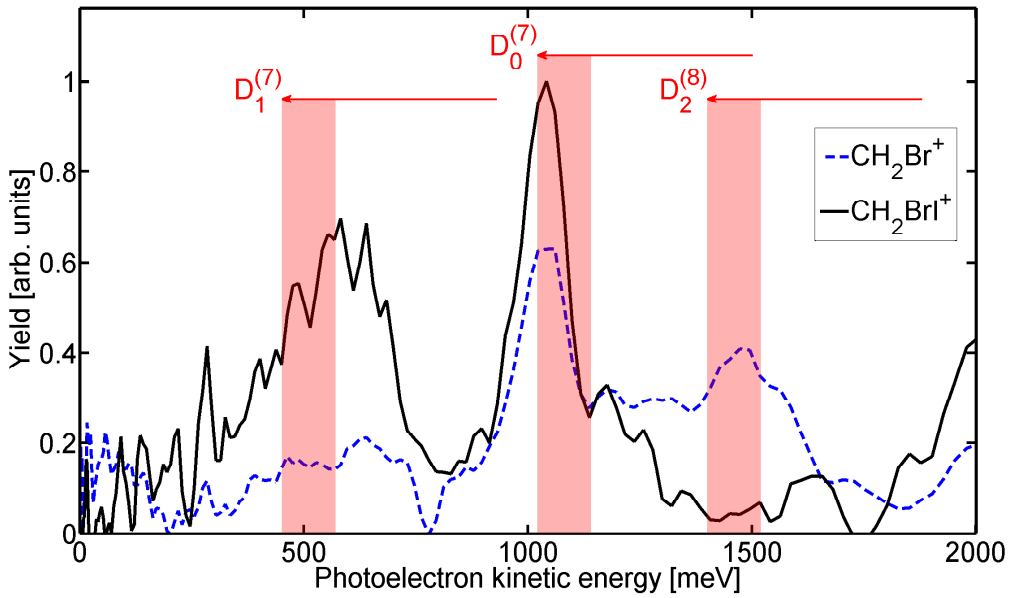

Figure 3.1: Photoelectron spectra for ionization of CH_2IBr. The dashed blue line shows the spectrum measured in coincidence with CH_2Br^+ fragments, while the solid black line shows the spectrum measured in coincidence with the parent ion. Superscript on the state labels indicate the number of photons absorbed to access the specific continuum. Arrows indicate the range of peak locations allowed for the full range of ponderomotive shifts in the laser focus, whereas the shaded region highlights the expected peak locations given the arguments discussed in the text.

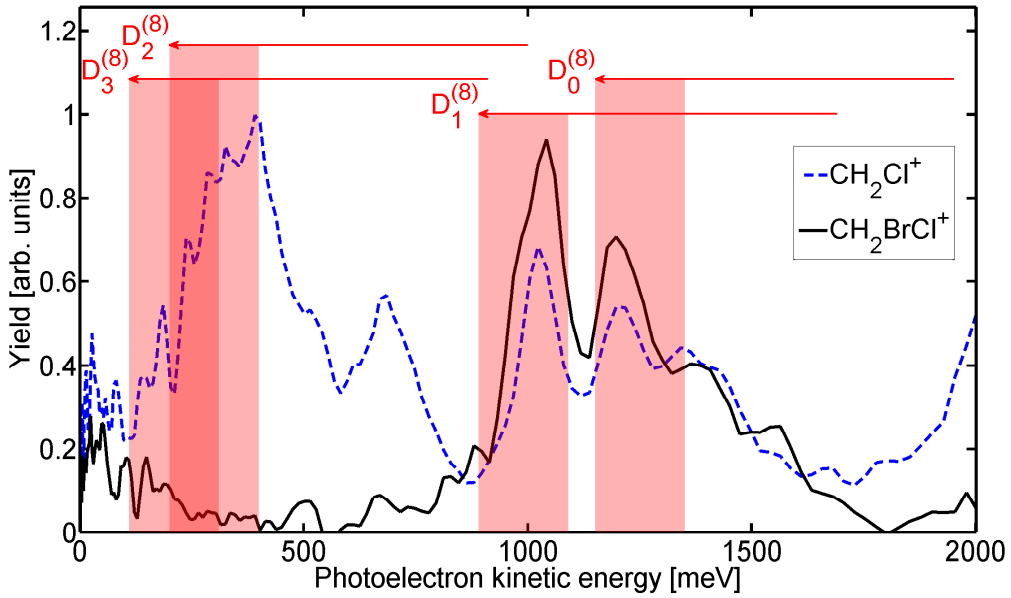

Figure 3.2: Photoelectron spectra for ionization of CH_2BrCl. The dashed blue line shows the spectrum measured in coincidence with CH_2Cl^+ fragments, while the solid black line shows the spectrum measured in coincidence with the parent ion. Superscript on the state labels indicate the number of photons absorbed to access the specific continuum. Arrows indicate the range of peak locations allowed for the full range of ponderomotive shifts in the laser focus, whereas the shaded region highlights the expected peak locations given the arguments discussed in the text.

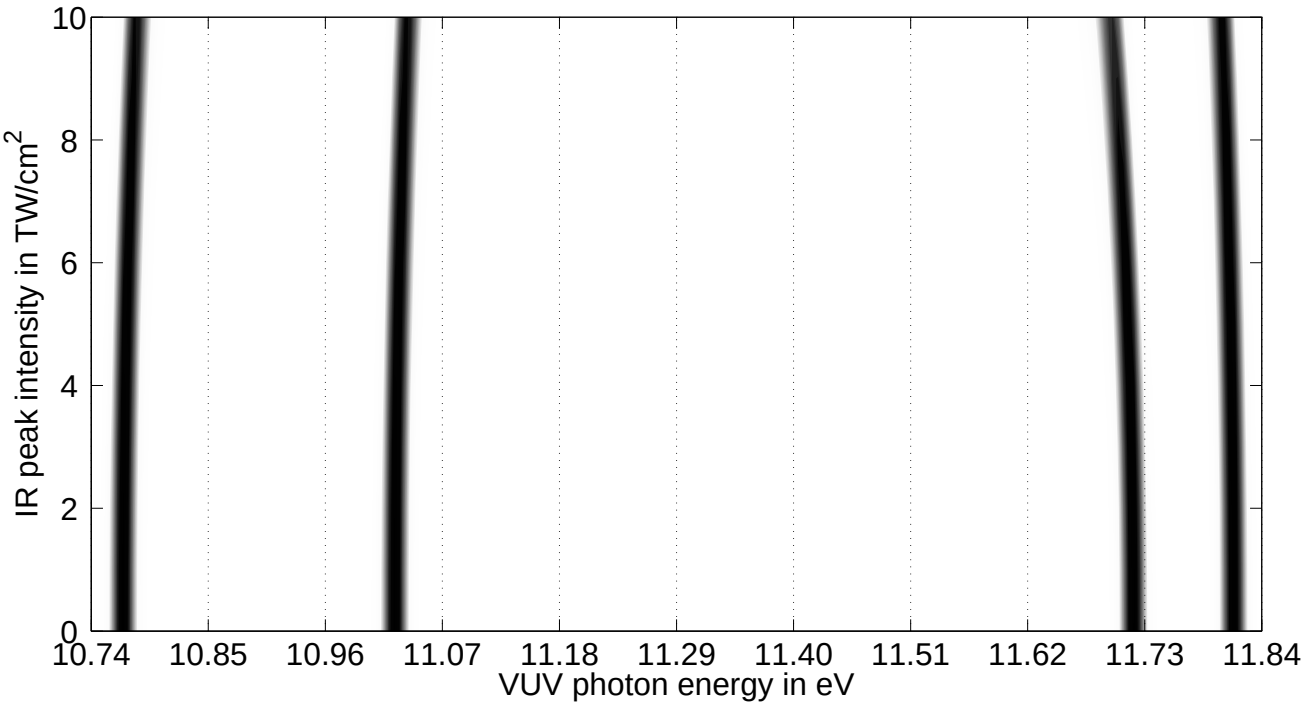

Figure 3.3: Calculations aimed at estimating dynamic Stark shifts for ionic states of CH_2BrCl in a strong field IR laser pulse. The graph shows population of the first five ionic states as a function of IR field strength and VUV photon energy. On the horizontal axis the frequency of the VUV radiation is plotted, while on the vertical, it is the peak intensity of the IR pulse.

population removed from the neutral state at a given VUV photon energy and IR field strength signaled ionization to one of the continua. Performing a series of calculations in which the VUV photon energy was scanned for different IR field strengths, the change in the ionization potential was followed for any of the continua as the IR field was varied from having zero (where the IP should coincide with the values given by *ab initio* theory) to nonzero strength. Simulations were performed with the IR electric field polarized along the C-Br bond. It is along this direction that the molecule-field coupling is the largest. Nevertheless, the shifts of the absorption peaks stay below 100 meV for the intensities used in the measurements (see figure 3.3). Similar calculations for CH_2IBr show similar Stark shifts. Since the other terms in equation 3.1 are significantly larger, neglecting E_{DSS} is expected to be a good approximation.

	CH_2IBr	CH_2BrCl
D_0	9.69	10.77
D_1	10.26	11.03
D_2	10.91	11.72
D_3	11.12	11.81
D_4	13.62	14.70

Table 3.1: Ionization potentials in eV. Energies for D_0 are experimental literature values from [34], while higher lying states are calculated relative to D_0 using the MRCI method as described in [33].

3.3 The Ponderomotive Shift

In equation 3.1, the third term on the right hand side is the ponderomotive potential, U_p, which describes the time-averaged kinetic energy of a charged particle in an oscillating electromagnetic field, and is given by:

$$U_p = \frac{e^2 I}{2\epsilon_0 m_e c \omega^2} \tag{3.2}$$

where *e* is the elementary charge, ϵ_0 is the vacuum permittivity, *c* is the speed of light, m_e is the mass of the electron, ω is the angular optical frequency of the laser field. As can be readily seen from equation 3.2, U_p depends on the laser frequency, ω, and intensity, *I*, but not on any molecular parameters.
As an illustration, one can visualize that a stationary photoelectron liberated *outside* of the laser field can be put into motion by it ("get dressed") once the laser intensity envelope rises to a nonzero value at its location; in other words, its potential energy is effectively raised. This is because the electric field does work on the charge (the electron "climbs the U_p hill"), leading to a wiggling motion [35]. Under certain conditions, the motion of the electron can be broken into two components: one is a localized oscillation driven by the laser field with amplitude $\frac{eE}{m\omega^2}$; the other is a drift motion due to the gradient of the spatial intensity envelope. The drift motion is driven by the so-called ponderomotive force $F_p(t) = -\frac{e^2}{4m\omega^2}\nabla E_{env}^2(\vec{r},t)$. The two conditions for the separation are: 1) the ponderomotive force is much smaller than the one that drives the oscillation; 2) the change in the field envelope E_{env} is negligible on the length scale of the oscillation amplitude. Having picked up by the field, the electron performs oscillatory motion and possesses ponderomotive energy. There are two exit channels from this state:

- The electron drifts out of the focal volume due to the ponderomotive force before the pulse is over. Once the electron escapes, it will have its ponderomotive energy converted to translational kinetic energy, which can be detected. One can show that in case of Gaussian spatial intensity profile (having σ width), the time scale associated with such a process is $t_{escape} \simeq \frac{\sigma m \omega_L}{eE_0}$, where *e* and *m* are the charge and mass of the electron, E_0 and ω_L are the peak field and the laser frequency, respectively. The condition for this channel to be open is $t_{escape} \ll \tau$, where τ is the pulse duration.

- The electron stays within the focal volume and is subject to the laser field for the entire pulse duration. It rides down on the temporal gradient of the trailing edge of the electric field envelope. Once the pulse passes, the electron returns to having negligible or no kinetic energy. The condition for this channel is $t_{escape} \gtrsim \tau$.

During experiments, electrons that are liberated *within* the laser field are considered, so they already possess ponderomotive energy U_p to start with. However, the electron can get to a field-free state ("undress") using the same two exit channels described above. The difference is how much kinetic energy they can come away with.[2] The experiments in this thesis were carried out in the short-pulse limit, $t_{escape} \gg \tau$. In this limit, since the initial ponderomotive energy will eventually be transferred to the field, the ionization potential for each electronic state is effectively increased by U_p [36]. This has to be taken into account when making the peak assignments. It has to be noted that not all ionization takes place at the peak intensity, and so there will be a distribution of ponderomotive shifts for molecules ionized at intensities around the peak intensity. However, since the ionization is a nonlinear function of intensity, most of the ionization takes place near the peak intensity (about 70% of the ionization yield occurs for intensities within 25% of the peak intensity for the data shown), and therefore the focus is on peak ponderomotive shifts in the discussion below.

[2]For the case $t_{escape} \ll \tau$, the measured photoelectron kinetic energy would be $K^i = nh\nu - I_p^i - E_{DSS}^i$ for the i^{th} continuum. This expression, as opposed to equation 3.1, lacks the term corresponding to the ponderomotive potential.

The peak ponderomotive shifts were measured using the intensity dependent shifting of peaks in the photoelectron spectrum of CS_2. CS_2 was chosen because the photoelectron spectrum is much simpler than for CH_2IBr or CH_2BrCl and because a linear shift was measured in the peak locations with intensity (ponderomotive shifting), indicating that for the range of intensities used in the calibration, intermediate resonances do not play an important role in determining the peak locations. The energy difference between the ground and first excited state of the cation is 2.6 eV [37], which means that for a large range of intensities it is possible to ionize only to the ground state.

Some details of the calibration process are outlined below. Figure 3.4a shows the measured photoelectron spectrum for CS_2 for different laser pulse energies. The pulse energy was controlled by programmatically varying the diffraction efficiency of the pulse shaper, and this allowed for higher precision, than, for instance, if a variable neutral density filter was used.

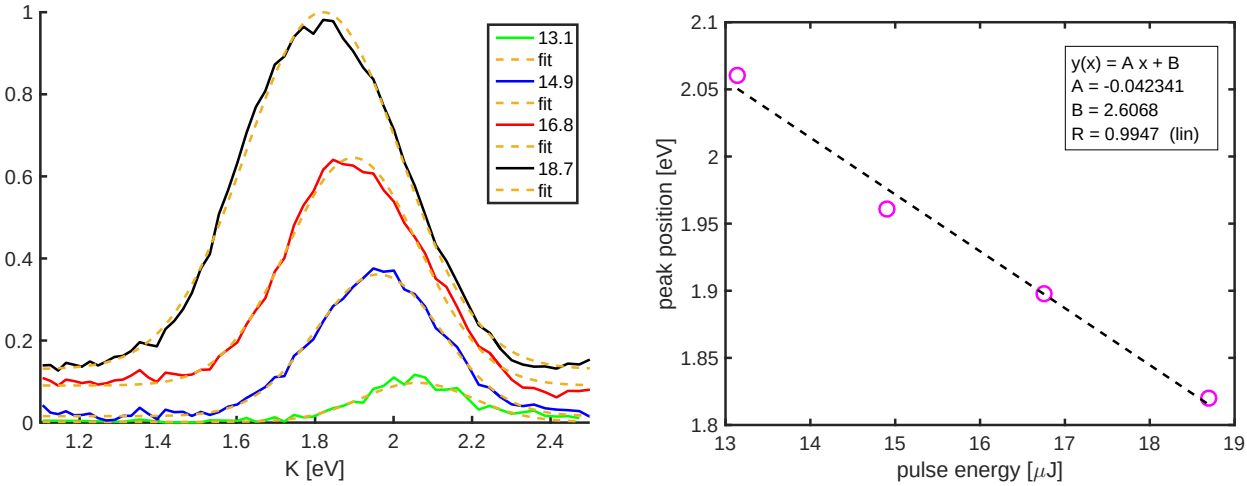

(a) Photoelectron spectra of CS_2 for different pulse energies (solid lines; values for the pulse energy in μJ are shown in legend), and Gaussian fits to the ponderomotively shifting peaks.

(b) Peak locations vs pulse energy (magenta circles) and linear fit (dashed black line).

Figure 3.4: Intensity calibration using ponderomotive shifts in CS_2.

By determining the peak position for each setting of the pulse energy (see figure 3.4b), and assuming a linear relationship between the two, the slope of this relationship tells us how much shift is produced per unit pulse energy. This is enough to estimate the ponderomotive potential in absolute terms, since for zero pulse energy the expected shift is zero.

Due to temporal and volume averaging of the laser intensity in the focus, the method described here gives a lower bound for the peak ponderomotive shift. This is because electrons that are liberated in spatio-temporal regions that 'see' lower laser intensities are shifted ponderomotively less than the peak value, and contribute only to the high-energy side of a given photoelectron peak, distorting the distribution. The severity of such distortion is also influenced by the intrinsic dependence of the photoelectron yield on the laser intensity; photoelectron distributions of higher order processes are distorted less. This last point is illustrated in figure 3.5. On the top panel, the fractional volume in a Gaussian laser focus is plotted as a function of the intensity (normalized to the maximum value I_0). On the lower panel, calculated yields for multiphoton ionization processes are plotted: the black dashed line is for pure 3^{rd} order, the red dashed line is for pure 6^{th} order processes. The solid lines take volume averaging into account, which means that the yield at each intensity is weighted by the fractional volume (shown on top panel) that corresponds

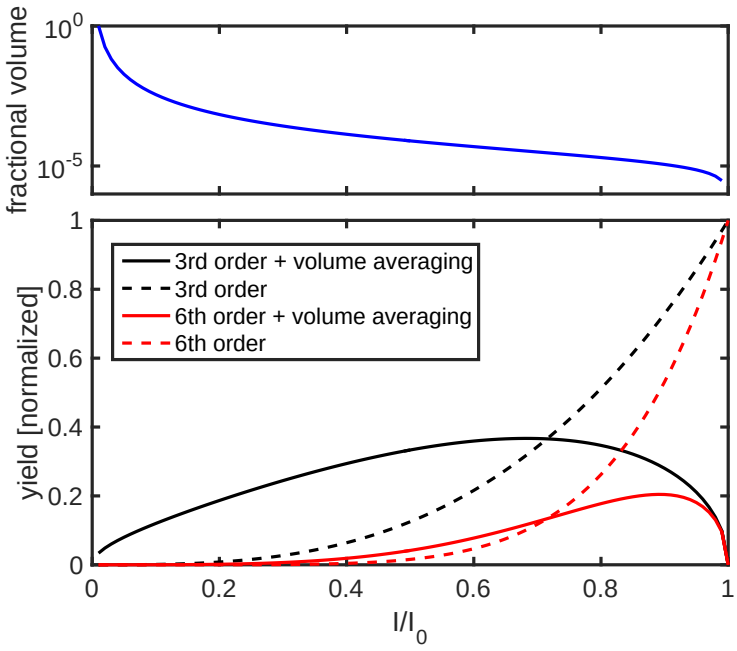

Figure 3.5: Illustration of the effect of volume averaging on intensity-dependent yields. Upper panel: fractional volume that 'sees' intensity I in a Gaussian laser focus, as given by $dV(I, I_0) = \frac{2I+I_0}{3I^2}\sqrt{\frac{I_0-I}{I}}dI$ [38]. Here I_0 is the peak intensity in the focus both in the spatial and temporal sense, while I is considered peak intensity only in the temporal sense, for different locations in the focus ($I \leq I_0$). On the lower panel, black and red dashed curves show yields for processes that have different polynomial dependence on intensity. Black and red solid curves show the same, but with volume averaging also taken into account (by multiplying the dashed curves with the curve of the fractional volume, shown on the upper panel).

to that specific intensity. When performing measurements on molecules with an ionization potential of $\approx$10 eV, and using near IR pulses ($h\nu$=1.6 eV), the photon order for the ionization process is 6 or higher. Looking at the solid red curve on the bottom panel of figure 3.5, one can see that the range of intensities having non-negligible contribution to the photoelectron spectrum for any peak is between $0.4 \cdot I_0$ and I_0. The accuracy with which the ponderomotive shift and hence the peak intensity is determined, is in principle further reduced if the peak under consideration is due to a weakly resonant process, and has a shift that is sub-ponderomotive. In case of CS_2, this is only a concern at higher intensities.

3.4 Photoelectron kinetic energy is determined at "birth"

During an ionization event, the kinetic energy carried away by the electron can be calculated using equation 3.1, where on the right hand side the second term is the ionization potential I_p^i, the binding energy associated with the ionic state D_i. The energy of this state is of course determined by how electrons are arranged in the different molecular orbitals. Since this arrangement can in principle change even after the electron leaves the ion core (for example, due to a post-ionization transition in the laser field), the question arises whether this change has any significant effect on the leaving electron. To put it in another way, when one measures the kinetic energy, does the obtained information reflect the state of the system during the instant of ionization, or is it also influenced by what happens after? In the following, an estimate is given for how much influence post-ionization transitions have on the outgoing electron, and it is eventually shown that the measured kinetic energy is mostly determined at the instance when the electron

is "born" in the continuum.

An analytic calculation is performed on the simplest molecule possible, H_2, examining what would happen if one of the electrons was removed and while it is drifting away from its origin, the parent ion H_2^+, originally in the ionic ground state, makes a transition to the first excited state. The question is how much the electrostatic potential energy changes during the transition, at different distances from the origin. Then a time interval is evaluated, corresponding to the time it takes for the electron to be separated enough from the ion such that the change in energy is negligible, which is then compared with the typical laser pulse duration.

I argue that H_2^+ is an appropriate system in which one can study this phenomenon for two reasons. The first is that the system is simple, its wavefunctions are well known and analytically calculable. The second is that since it is the smallest molecular system possible, its ionization potentials for the ground and first excited ionic states are the largest among the singly charged cations, and the energy difference between the two states is also the largest. So any change in energetics one sees in this case is going to be an upper bound compared to larger, singly charged systems.

The aim is to calculate the difference in the electrostatic potential energies of the ground and the first excited ionic states of H_2^+ at different points in space.

$$\Delta E(x,y,z) = \frac{1}{4\pi\epsilon_0}\int_{-\infty}^{+\infty}\int_{-\infty}^{+\infty}\int_{-\infty}^{+\infty}\frac{\Delta\rho(x',y',z')}{\sqrt{(x-x')^2+(y-y')^2+(z-z')^2}}dx'dy'dz' \tag{3.3}$$

where the charge density difference ($\Delta\rho$) is due to the different spatial distributions of the bonding (Ψ_B) and antibonding (Ψ_{AB}) wavefunctions (corresponding to ionic states $1\sigma_g$ and $1\sigma_u$, respectively).

$$\Delta\rho(x,y,z) = -e\cdot(|\Psi_B(x,y,z)|^2 - |\Psi_{AB}(x,y,z)|^2) \tag{3.4}$$

$$\Psi_B(x,y,z) = N_B\left(e^{-Z\cdot\sqrt{x^2+y^2+(z+R/2)^2}} + e^{-Z\cdot\sqrt{x^2+y^2+(z-R/2)^2}}\right) \tag{3.5}$$

$$\Psi_{AB}(x,y,z) = N_{AB}\left(e^{-Z\cdot\sqrt{x^2+y^2+(z+R/2)^2}} - e^{-Z\cdot\sqrt{x^2+y^2+(z-R/2)^2}}\right) \tag{3.6}$$

Here R=2.08 Bohr is the bond length, N_B and N_{AB} are normalization factors. Equation 3.3 is evaluated numerically on a rectangular grid, and the result is shown in figure 3.6 along with the density plots of the wavefunctions.

As the next step, let's compare how much distance an electron travels within the duration of a τ=30 fs laser pulse due to acceleration in the homogeneous electric field (magnitude $\approx 300\ \frac{V}{cm}$) of the imaging plates. Two scenarios are considered: an electron having initially zero and 1 eV kinetic energy. In the first case, the electron accelerates from zero velocity steadily, so the distance it travels is:

$$s = \frac{eE}{2m}\tau^2 = 0.04\,a_B$$

where $a_B = 0.529\mathring{A}$ is the Bohr radius. One can see from figure 3.6 that the energy shift within that distance can easily be on the order of an electronvolt, depending on the direction. This amount of change is much larger than the kinetic energy the electron possesses.

In the second case, having started with an eV of kinetic energy and assuming no further acceleration, the distance traveled is:

$$s = \sqrt{\frac{2E}{m}}\cdot\tau = 340\,a_B$$

This is four orders of magnitude larger distance than in the first case, and consequently the electron most of the time travels through a region of space where, even if the molecule switches states, no significant

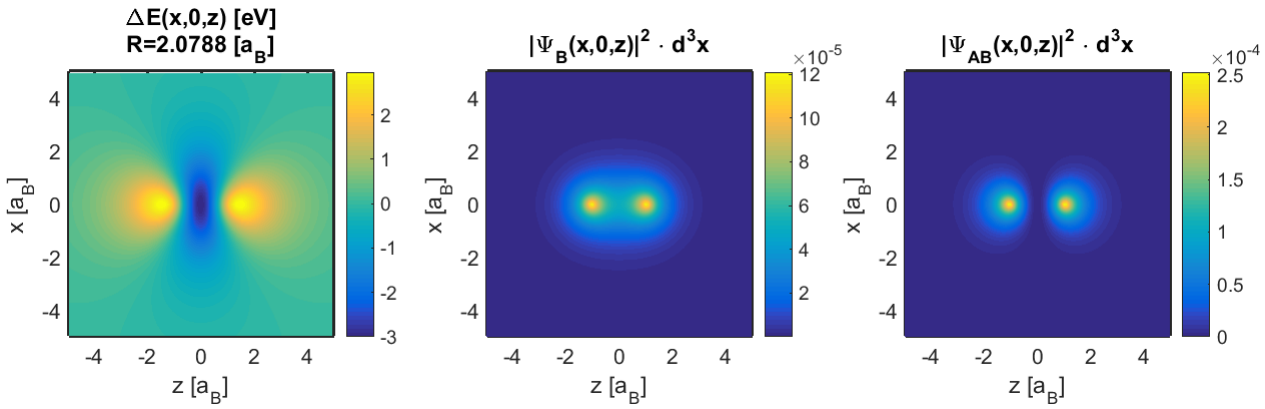

Figure 3.6: Center and right panels: H_2^+ bonding and antibonding orbitals; left panel: Electrostatic potential energy difference between the two orbitals.

change in the kinetic energy would take place. In fact, it is enough to travel a distance of 20 a_B from the ion in any direction for the switching effect be negligible ($\leq$5 meV). Electrons with 4 meV kinetic energy travel that much within the duration of a 30 fs pulse; those with higher kinetic energies will get out of the region of influence even faster. Since most of the electrons detected during the experiments in this thesis have significant nonzero kinetic energies (up to 3–8 eV), one can argue that it is the second scenario that applies in most cases. Hence, the kinetic energy detected is a faithful representation of what electrons possess at the time they appear in the continuum.

3.5 Discussion

In figure 3.1, horizontal arrows indicate regions where photoelectrons coming from the lowest-lying electronic states of the ion contribute to the spectrum; the tail of each arrow indicate the appearance energy of the photoelectrons at zero field (zero ponderomotive potential), while the head of each arrow shows the same for the peak of the field (peak ponderomotive potential). The red shaded areas further highlight regions of the spectrum where the U_p is within 25% of its peak value for each state, since as noted above, most of the ionization takes place within this range of the ponderomotive shift.
In assigning the peaks in the photoelectron spectrum of CH_2IBr to specific ionic states, it has to be noted that D_4 has a significantly higher ionization potential than states D_0 to D_3. This suggests that ionization to D_4 should be suppressed with respect to the lower states. Measurements of the ion time-of-flight mass spectrum (TOFMS) are consistent with this expectation in that very few fragment ions are measured coming from ionization to D_4, which can fragment to form I^+ or CH_2I^+ [34]. Furthermore, earlier measurements performed with velocity map imaging of the ionic fragments found that CH_2Br^+ produced with kinetic energy less than 0.30 eV could be associated with dissociation on D_2 or D_3, whereas CH_2Br^+ produced with a kinetic energy above 0.50 eV could be associated with D_4. Measurements carried out at the same intensity as the measurements shown in this chapter did not find any CH_2Br^+ with kinetic energy above 0.50 eV, consistent with the idea that there is no ionization to D_4 in the present measurements [39]. Thus, the interpretation of the spectrum is restricted to ionization to D_0 through D_3. It is also noted that for both CH_2IBr and CH_2BrCl, the lowest two ionic states, D_0 and D_1, are bound, while D_2 and D_3 are dissociative [39, 34]. Finally, as it was shown in the previous section, the photoelectron energy is determined at the moment of ionization, and thus transitions in the ion driven by the laser do not affect the photoelectron spectrum. Thus, the peaks measured in coincidence with the parent ion must come from ionization to D_0 and D_1. Peaks measured in coincidence with the fragment ion are more subtle, but

comparison with the spectrum measured in coincidence with the parent can distinguish between different cases. Peaks in the spectrum that are measured in coincidence with the fragment, but do not appear in the spectrum measured in coincidence with the parent, can be associated with direct ionization to dissociative states D_2 and D_3, whereas peaks that appear in both spectra can be associated with indirect ionization to D_2 or D_3 (i.e. ionization to D_0 or D_1 followed by laser driven transitions in the ion).

Given these considerations, it is natural to assign the peaks in the CH_2IBr spectrum at 1.04 eV and $\approx$0.55 eV to D_0 and D_1 and the peak at 1.45 eV to D_2 or D_3 (which have very similar energies). The peak at 0.55 eV shifts with intensity (see figure 3.7), while the peaks at 1.04 and 1.45 eV do not. This is because the peaks at 1.04 and 1.45 eV are due to resonantly enhanced ionization (via Freeman resonances [36, 40]), whereas the peak at 0.55 eV is not resonantly enhanced. In order to test this preliminary assignment of the peaks, the expected energies for these peaks based on equation 3.1 are considered, assuming that each peak is generated near the peak intensity of the pulse and therefore experiences the peak ponderomotive shift. For this case of maximal ponderomotive shift, and considering the lowest order process that would lead to a positive photoelectron energy, the peak corresponding to D_0 is expected to be at $K = 7 \times 1.60 - 9.69 - 0.48 = 1.03$ eV, which compares favorably with the measured 1.04 eV. For D_2, 7 photon ionization is not energetically allowed, and therefore $K = 8 \times 1.60 - 10.91 - 0.48 = 1.41$ eV is expected, which again agrees well with the experiment. For the peak assigned to D_1, the predicted energy is $K = 7 \times 1.60 - 10.26 - 0.48 = 0.46$ eV. This again is in reasonable agreement with the experimental measurements, confirming the initial assignments. It is natural to look for evidence of ionization to D_3, given the small difference in ionization potential between D_2 and D_3. The expected location for a peak corresponding to D_3 is $K = 8 \times 1.60 - 11.12 - 0.48 = 1.20$ eV, at which nonzero yield can be seen, although there is not a well defined peak. Therefore it is difficult to draw a firm conclusion as to whether or not there is substantial ionization to D_3.

Similar arguments can be made to assign the peaks in the spectrum for CH_2BrCl, taking into account that for these measurements the laser was tuned slightly to the red and thus the photon energy was 1.59 eV. Also, given the higher ionization potential of this molecule, higher intensities were set to get a comparable yield and thus the peak ponderomotive shift is 0.80 eV. Again, the focus is on the four lowest-lying states, since as in the case of CH_2IBr, D_4 is much higher in energy than the states below it. The two lowest-lying ionic states, D_0 and D_1 are not dissociative, while D_2 and D_3 are, leading mostly to the production of CH_2Cl^+ [34]. Peaks corresponding to the first two of the four states mentioned are expected to be found in the spectra associated with the parent ion, as a result of direct ionization. However, it is expected that some of these may also be found in the spectra of the fragment, which can be explained by post-ionization transitions of the ion from a non-dissociative to a dissociative state. Additionally, it is clear that in the spectrum of the parent, no peaks are expected to be seen corresponding to dissociative states.

In the spectrum associated with the parent ion, two narrow peaks are visible at 1.04 eV and 1.20 eV, which also show up in the spectrum of the fragment (see figure 3.2). These, based on the above arguments, can be assigned to the states D_1 and D_0, respectively. The expected kinetic energy for electrons associated with D_0 is $K = 8 \times 1.59 - 10.77 - 0.80 = 1.15$ eV and for D_1 it is $K = 8 \times 1.59 - 11.03 - 0.80 = 0.89$ eV at the maximum ponderomotive shift. The observed appearance energies lie well within the range set between the 75% and the peak ponderomotive shift, which supports the assignment.

The spectrum associated with the fragment ion (figure 3.2) shows two features that are absent from the parent spectrum: a broad feature between 0.10 and 0.50 eV (centered at 0.30 eV), and a relatively narrow one centered at 0.70 eV. The peak at 0.30 eV can be associated with both D_2 and D_3 since the expected energies for the two states are close together and both fall within this broad peak. The expected energies for D_2 and D_3 are $K = 8 \times 1.59 - 11.72 - 0.80 = 0.20$ eV and $K = 8 \times 1.59 - 11.81 - 0.80 = 0.11$

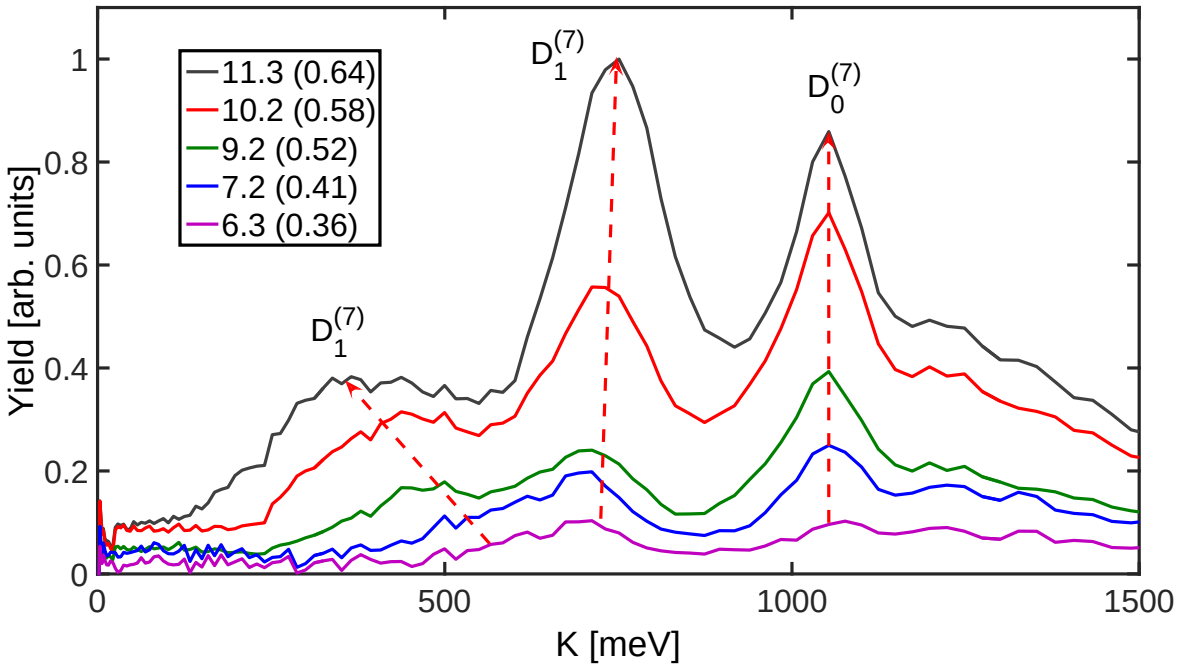

Figure 3.7: Photoelectron spectrum for CH_2IBr for several different laser intensities. Superscript on the state labels indicate the number of photons absorbed to access the specific continuum. Legend: laser peak intensity in TW/cm^2 (and ponderomotive potential in eV).

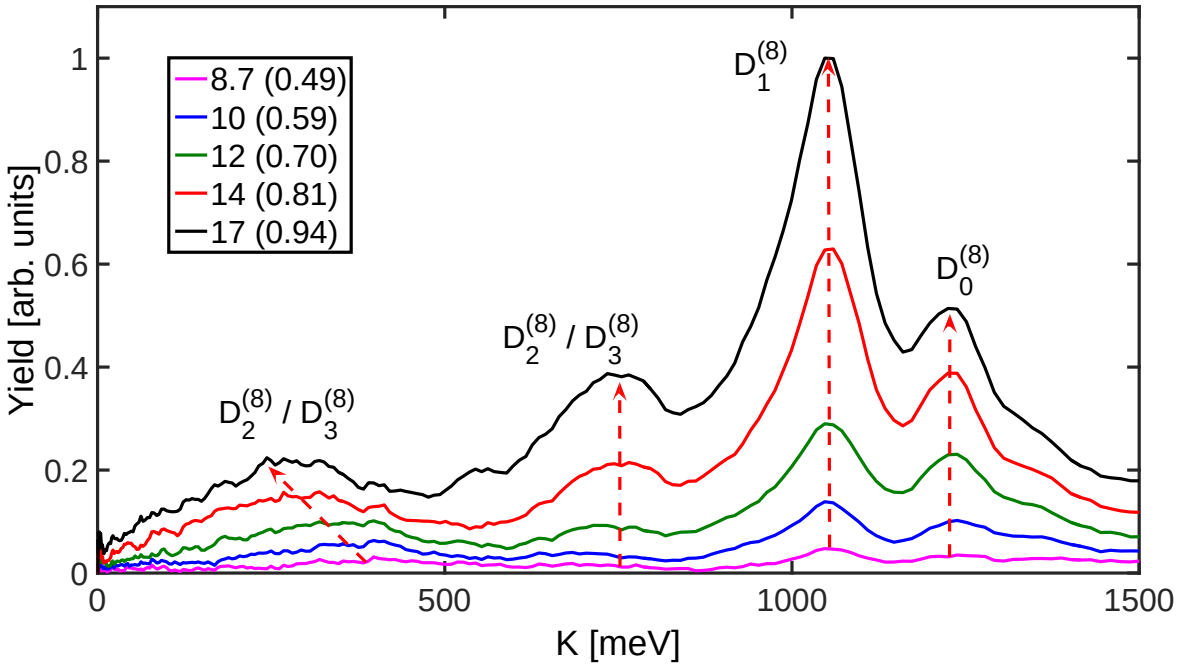

Figure 3.8: Photoelectron spectrum for CH_2BrCl for several different laser intensities. Superscript on the state labels indicate the number of photons absorbed to access the specific continuum. Legend: laser peak intensity in TW/cm^2 (and ponderomotive potential in eV).

eV respectively. However, the origin of the 0.70 eV peak is unclear. Looking at the intensity dependent measurements shown in figure 3.8, one can see that this peak and the peak at ≈0.30 eV in the coincidence spectrum have a common energy for a low intensity which corresponds to an intensity close to where the peak(s) appears in the spectrum. This, in conjunction with the fact that the peak is in coincidence with the fragment ion suggest that it is associated with ionization to either D_2 or D_3 or both. As it does not shift with intensity, it is resonantly enhanced, and the position in the spectrum corresponds to the resonant enhancement occurring at about 1/3 of the peak ponderomotive shift.
In addition to the radial distributions discussed above, the velocity map imaging measurements of the photoelectrons also provide angular distributions. While the angle-dependent yields are not the focus of the current analysis, it is noted that the angular distributions for the 0.30 eV and 0.70 eV peaks are the same (within the statistical uncertainty of the measurements), but different from the 1.04 eV and 1.20 eV peaks. This is consistent with the idea that the 0.30 and 0.70 eV peaks are both due to ionization to D_2/D_3.

As noted above, resonances in both the neutral and the ion play an important role in the ionization dynamics. The intensity dependence of the photoelectron spectrum (see figures 3.7 and 3.8) highlights the role of neutral resonances, and the comparison of photoelectron spectra in coincidence with the parent and fragment ions highlights the role of ionic resonances. In order to illustrate the role of ionic resonances and to distinguish between direct and indirect ionization to a given final ionic state, figure 3.9 is invoked. This figure shows how the direct and the indirect ionization pathways can be associated with different peaks in the coincidence photoelectron spectra. The appearance of a peak corresponding to the nondissociative state D_0 in the fragment spectrum signifies that accessing a dissociative state (most likely D_2 or D_3) took place in at least two steps (first ionization, then a transition in the ion). Hence this pathway is called "indirect" - this is to be contrasted with the peak corresponding to D_2, which is associated with a "direct" multiphoton transition from S_0 (the neutral ground state) to D_2.

As noted briefly above, the intensity dependence of the photoelectron spectra (shown in figures 3.7 and 3.8) allows us to distinguish between resonance enhanced ionization and non-resonant ionization. These measurements are not made in coincidence mode. The peaks which do not shift ponderomotively with intensity correspond to resonantly enhanced ionization. These are the 1.04 eV peak for D_0 and the 0.70 eV peak for D_1 in CH_2IBr; also the 1.20 eV peak for D_0, the 1.04 eV peak for D_1 and the 0.75 eV peak for D_2/D_3 in CH_2BrCl. However, broad features are also present in the spectrum, which shift to lower appearance energies as the laser peak intensity increases. One shifts from 0.50 to 0.30 eV in CH_2IBr and this is assigned to a nonresonant contribution from D_1. The other is observed in CH_2BrCl and shifts from 0.40 to 0.25 eV, and this is attributed to D_2/D_3 as was previously discussed. Based on the intensity dependent spectra, it is clear that strong field ionization in these two molecules proceeds via a mixture of resonance enhanced and non-resonant ionization.

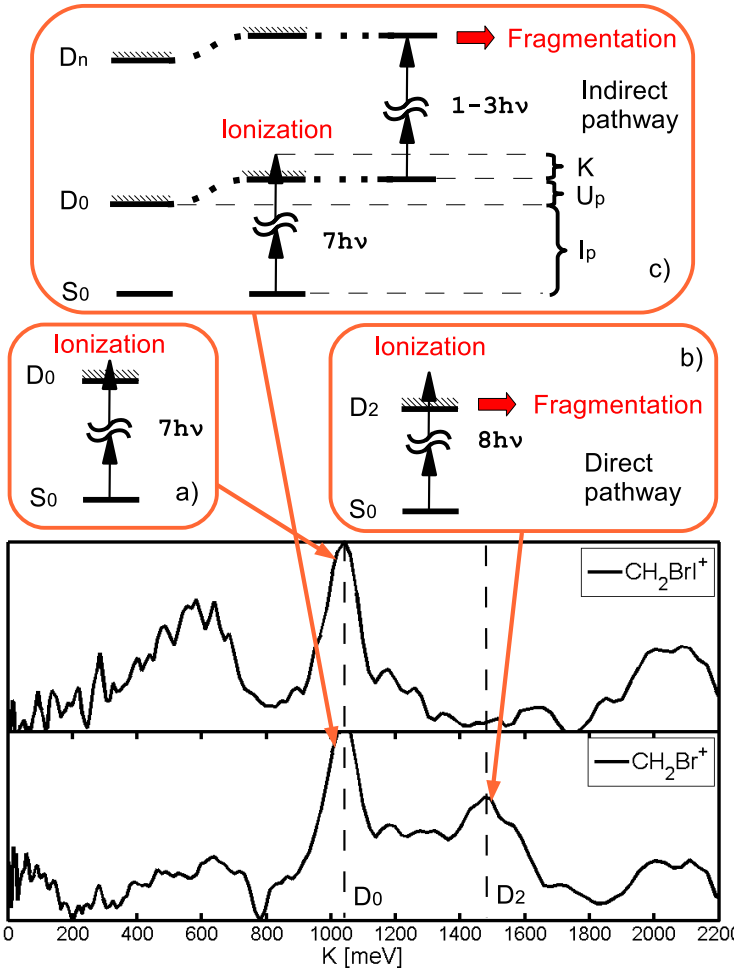

Figure 3.9: Illustration of dissociative and non-dissociative pathways in the ion, and their signature in the measured photoelectron spectra associated with the parent and fragment cations of CH_2IBr. a) direct 7-photon ionization to the nondissociative continuum D_0. b) direct 8-photon ionization to the dissociatiove continuum D_2. c) 7-photon ionization to the non-dissociative continuum D_0, followed by a post-ionization transition to a higher-lying dissociative state (D_n). Arrows point to the corresponding peaks in the spectra.

Chapter 4

Strong-Field Molecular Ionization in the Impulsive Limit

4.1 Introduction

As mentioned in chapter 1, strong-field ionization plays an important role in the generation of attosecond pulses and electron wave packets, and it can also be used to track excited state molecular dynamics. Improving time resolution is key in molecular dynamics experiments [41, 42]. For creating single attosecond pulses, the established technique is to use a few-cycle, high intensity, phase-stabilized NIR driver field [13, 43]. It has been demonstrated that 10-cycle pulses in the mid-infrared can also be used [14]. These examples are meant to highlight that it is important to understand how ionization depends on the duration of the strong-field driving pulse.

For ultrafast pulses with several optical cycles, an extensive body of work on atomic and molecular strong-field ionization [5, 38, 40], and also chapter 3 in this thesis show strong evidence for the important role of neutral resonances during the multiphoton ionization process. However, a largely unexplored aspect of the phenomenon is whether resonances still play a role when the pulse duration is shortened to include just a few optical cycles. In an attempt to get an intuitive picture, we can turn to classical physics to see how resonance takes place in a simple driven, damped harmonic oscillator. In the time domain, a general characteristic of such a response is that it builds up over multiple periods of excitation. This characteristic carries over to the two-level system in quantum physics: when coupled with a broadband radiation on a single-photon or multi-photon level, resonant transfer of population due to weak to moderate fields from one state to the other takes place over multiple cycles. It remains a question what happens in case two states are multiphoton-coupled by an intense few-cycle pulse, especially if vibrational dynamics can also play a role in determining the state populations.

In this chapter, the main focus is on ionization experiments that were carried out with coherent, broadband, high-intensity optical radiation. These enabled the study of strong-field molecular ionization with pulses whose duration could be varied from 40 fs to below 10 fs, where vibrational dynamics is frozen (this timescale will be called the 'impulsive limit') [17]. These experiments provided us with a few surprises. At the same time, they revealed a great deal about the importance of coupling between electronic and nuclear degrees of freedom. It was found that the optical spectral broadening does not always result in access to more states; also, the importance of non-Born-Oppenheimer dynamics was highlighted in determining ionic state populations.

4.2 Results

Figure 4.1 shows photoelectron spectra for CH_2IBr as a function of pulse duration. For longer pulses (>20 fs), two peaks are visible: one at ≈1.2 eV and the other at ≈0.7 eV. It is shown in chapter 3 that these peaks can be assigned to leaving the molecule in the first two states of the molecular cation: D_0 and D_1, respectively. While the yield from 0-0.2 eV and around 1.6 eV can be assigned to D_2/D_3, we focus on the yield to D_0 and D_1 for simplicity here. Earlier work [44] also established that these peaks involve resonance enhancement via intermediate neutral states that Stark shift into resonance during the ionization process. An observation such as this provides strong proof that intermediate neutral states can play an important role even for very short pulses, where the resonance condition is only met for a relatively short time, provided that there is sufficiently strong coupling. For longer pulses, ionization proceeds such that D_0 and D_1 are populated with roughly equal probability. However, as the pulse is shortened to below 12 fs, the yield for the D_0 peak diminishes and eventually becomes negligible compared to that of the D_1 peak. This is surprising given that the ionization potential for D_0 (9.7 eV) is lower than for D_1 (10.2 eV) [33], and that the bandwidth of a shorter pulse is broader, hence would enable to access more transitions (possibly leading to more ionization) than with a longer pulse and narrower bandwidth.

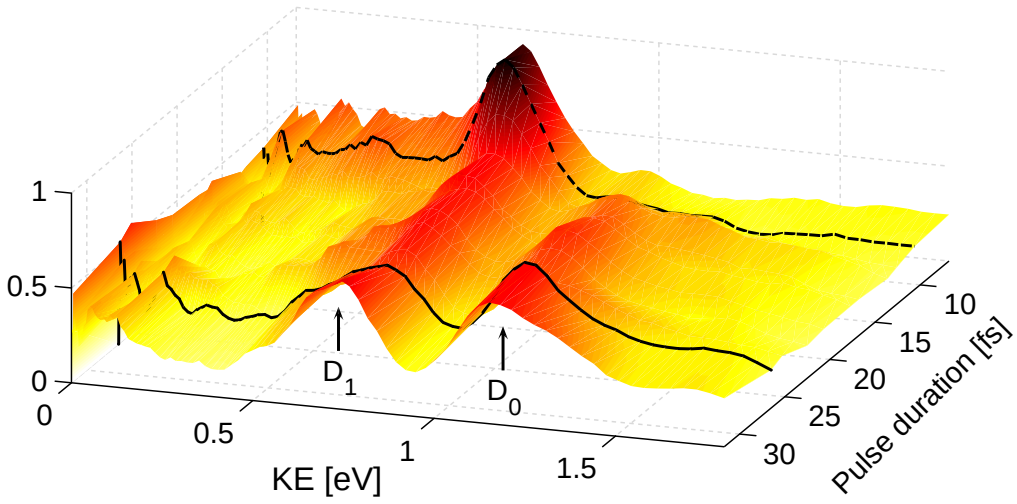

Figure 4.1: Photoelectron spectra (yield vs photoelectron kinetic energy, KE) for ionization of CH_2IBr for different pulse durations.

To record the data shown on figure 4.1, pulse broadening in a laser-induced filament was used, as described in section 2.4. Briefly, the linearly polarized pulses were compressed to near the transform limit with a 4-f grating compressor, and measured using a self-diffraction FROG apparatus [45]. The broadest spectrum produced is capable of supporting sub-6 fs pulses, and FROG measurements place an upper limit on the duration of the full bandwidth pulses of about 8-9 fs. The spectrum is cut using a variable slit in the grating compressor in order to obtain the variable bandwidth for the measurements below. The spectrum of the pulse is adjusted at the focusing element instead of the Fourier plane in order to avoid hard cutoffs at the edges of the spectrum, which would lead to a structured pulse in the time domain. The pulse durations quoted in the figure are estimated by applying inverse-Fourier transform to the recorded optical spectra and calculating the intensity profile of the pulses in the time domain.

The noncoincident ionization signal is detected in the VMI chamber (see section 2.5) in counting mode. The laser intensity is adjusted between 10-13 TW/cm^2 to keep the ionization yield roughly constant as the pulse duration is varied, yielding about 20±10 electrons per laser shot. When generating the

photoelectron spectra from the raw VMI images, we focus on the yield that is generated $\pm 30^\circ$ around the laser polarization direction. Integrating over all angles yields similar results, with slightly less contrast of the peaks.

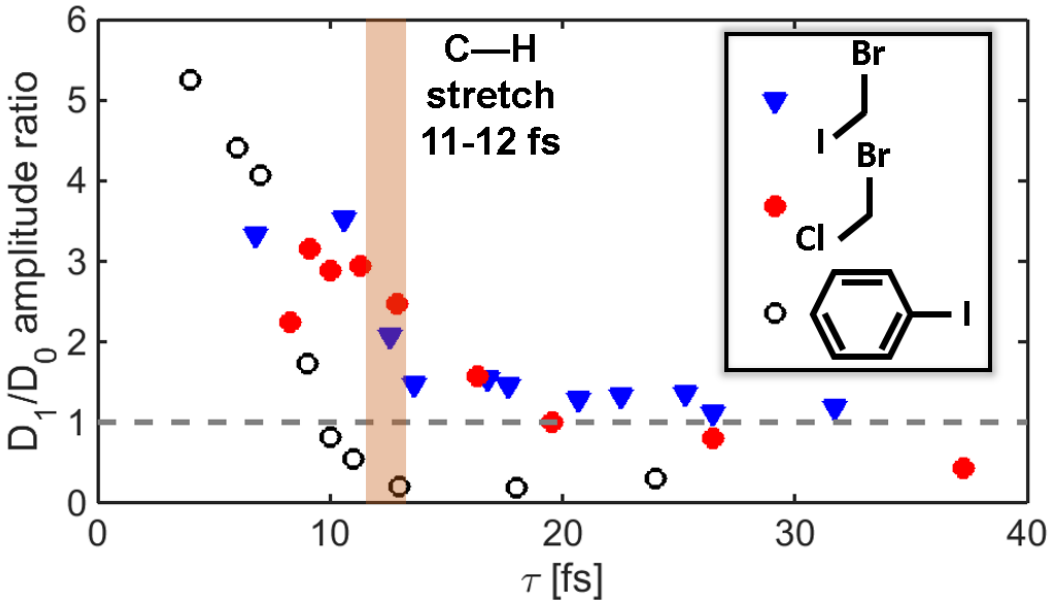

Figure 4.2: Ratio of D_1/D_0 as a function of pulse duration τ for three different molecules.

Similar measurements were carried out for other molecules and similar dynamics were observed. Figure 4.2 shows the D_1 and D_0 ratio as a function of pulse duration for three different molecules: CH_2IBr, CH_2BrCl and C_6H_5I. Data was taken for the latter two systems using the same procedure as for the first, and as described in the previous two paragraphs. For any given molecule, the photoelecron spectra for each pulse duration were decomposed to a series of peaks, which were assigned to different ionic continua. (For the case of CH_2IBr, see figure 4.3.) For each molecule, the peak positions and widths were determined globally. These values were then used when fitting the spectra for each pulse duration, during which only the amplitudes were left to be determined by the fitting procedure. As the figure illustrates, all three molecules show similar behavior as a function of pulse duration. A shaded vertical bar marks the impulsive limit, corresponding to the C-H stretch vibrational period ($\approx$11 fs - the shortest vibrational period for organic molecules) [46].

4.3 Dynamics is driven by pulse duration

In this section, the aim is to interpret the measurements and determine whether the mechanism underlying the switching/control is driven by dynamics or spectral content. Since a shorter pulse duration requires a broader spectrum, it is natural to ask whether the suppression of ionization to D_0 is driven by new frequency components in the pulse, or rather by the pulse becoming shorter.

This question is first addressed by making measurements with a series of narrowband optical pulses with different central frequencies: figure 4.4 shows the resulting individual photoelectron spectra. (These were used as a basis set for constructing the single photoelectron spectrum shown on the bottom panel of figure 4.5 with dashed red line.) Again the frequency content of the optical pulse was manipulated by adjusting a slit in the grating compressor used to compress the pulses (see figure 2.9 for the layout of the

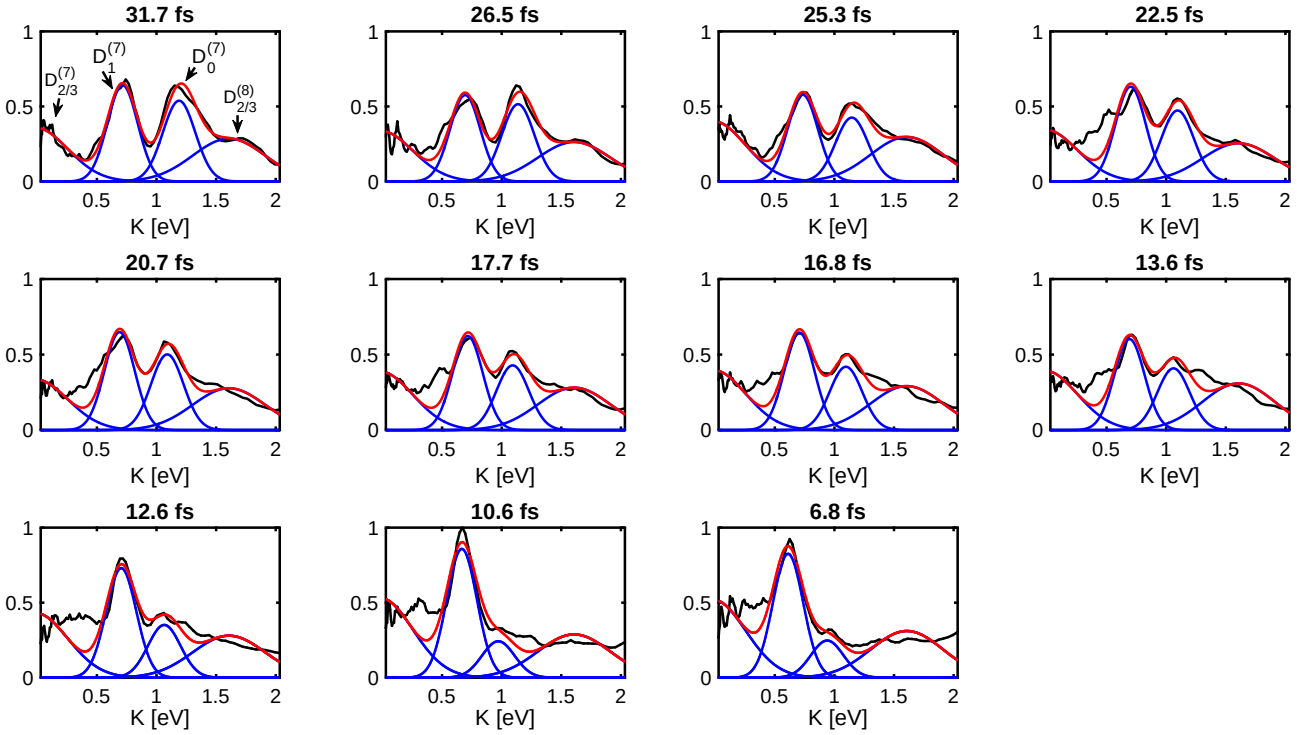

Figure 4.3: Decomposition of photoelectron spectra of CH_2IBr to a series of peaks representing ionization to different continua. Different panels show spectra for different laser pulse durations (indicated above each panel). Four ionization channels are identified, labelled as $D_0^{(7)}$, $D_0^{(7)}$, $D_{2/3}^{(7)}$ and $D_{2/3}^{(8)}$. $D_0^{(7)}$ stands for ionization to the ground ionic state, D_0 with 7 photons, etc. Blue curves show the fitted Gaussians for the individual peaks, red curve shows their sum.

setup). However, in contrast to the measurements shown on figure 4.1, this time the width of the slit was held constant and its position was varied across the spatially dispersed spectral components.

In figure 4.4, at each photon energy and at any given multiphoton order a number of peaks can be distinguished. Based on the work outlined in chapter 3, an attempt is made to assign these to ionization to the four lowest lying ionic states, D_0 to D_3. Here, as equation 3.1 suggests, the photon energy, the order of the transition, the ionization potential for each continua and the ponderomotive shift have to be taken into account. As the photon energy is tuned, the peak locations shift substantially, in accord with equation 3.1. It appears that for photon energies >1.7 eV, ionization leaves the molecule mostly in the ground ionic state, D_0. This can be seen by considering where yield associated with D_0 is expected to form a peak at different photon energies. To guide the eye, two sets of lines are shown on figure 4.4. Points along the white dashed line are calculated considering $K = nh\nu - I_p$. For the solid red line, an estimate of the ponderomotive energy is also considered, giving $K = nh\nu - I_p - U_p$. The value of U_p is estimated the following way: $U_p^{(0)}$=0.7 eV is assumed at a photon energy of $h\nu^{(0)}$=1.45 eV, based on typical intensities used in the experiment. Then, for the curves with different photon energies, U_p is scaled taking into account its dependence on photon energy and intensity: $U_p = U_p^{(0)} \left(\frac{Y}{Y^{(0)}}\right)^{\frac{1}{n}} \left(\frac{\nu^{(0)}}{\nu}\right)^2$. Here the variation in intensity is estimated based on the total measured photoelectron yield (which varied in the experiment by about a factor of 3), assuming n-photon ionization: $Y \propto I^n$. Though this approach clearly has the limitation that it does not take into account that the total yield gets contributions from a number of channels with possible different multiphoton orders, the result, shown with red solid lines on figure 4.4, lines up well with most of the observed peaks. Though a detailed analysis of the data is be-

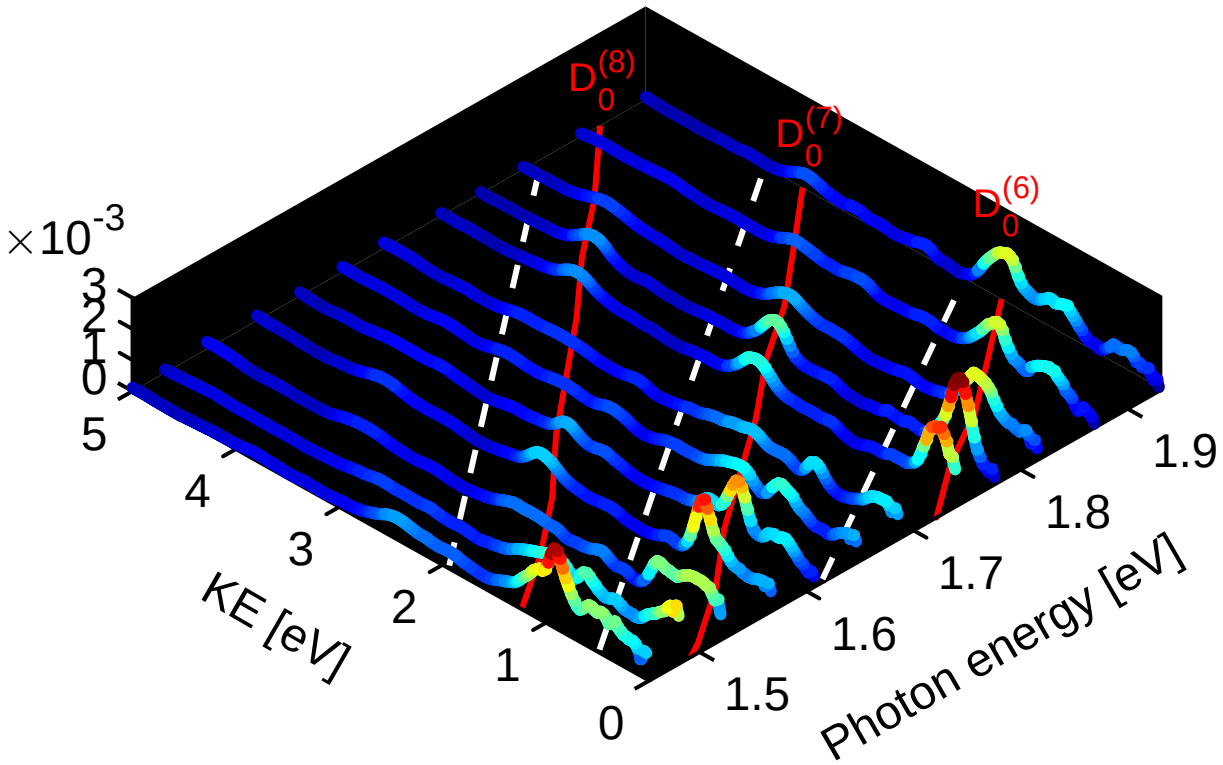

Figure 4.4: Photoelectron spectra of CH_2IBr for narrowband (FWHM≈30 nm) excitation with different central wavelengths, or photon energies. White dashed lines: expected appearance energies of D_0 for different multiphoton orders assuming U_p=0 eV. Solid red lines: expected appearance energy of D_0 but assuming U_p=0.7 eV at a photon energy hν=1.45 eV. In the latter, the dependence of U_p on photon energy and intensity was also taken into account (see text).

yond the scope of this section, it can be crudely divided into two regions. For photoelectron spectra with $h\nu$ >1.7 eV, nonresonant population transfer to D_0 is the main ionization mechanism. For $h\nu$ ≤1.7 eV, the peak assignment is more subtle, and involves resonantly enhanced as well as nonresonant channels to D_0 and/or D_1.

Having obtained the constituent narrowband photoelectron spectra, the next step is adding them up with the appropriate weights and comparing the result with the photoelectron spectrum measured for a short pulse that includes all the spectral components coherently. This idea is illustrated in figure 4.5. The top panel shows the optical spectrum of the short pulse (solid black line) and the weighted sum of the narrow optical spectra (dashed red line) together, while the lower panel shows the resulting photoelectron spectra - one curve for the sum of the photoelectron spectra produced with narrowband pulses (dashed red line), and one curve for the photoelectron spectrum produced by a broadband pulse (solid black line). The photoelectron spectra for the narrowband pulses were added in proportion to the coefficients for the narrowband optical spectra in forming the broadband spectrum as a linear combination. While the optical spectra are almost identical, there are significant differences between the two photoelectron spectra, indicating that it is not a single frequency in the pulse spectrum which drives the switching between ionic continua.

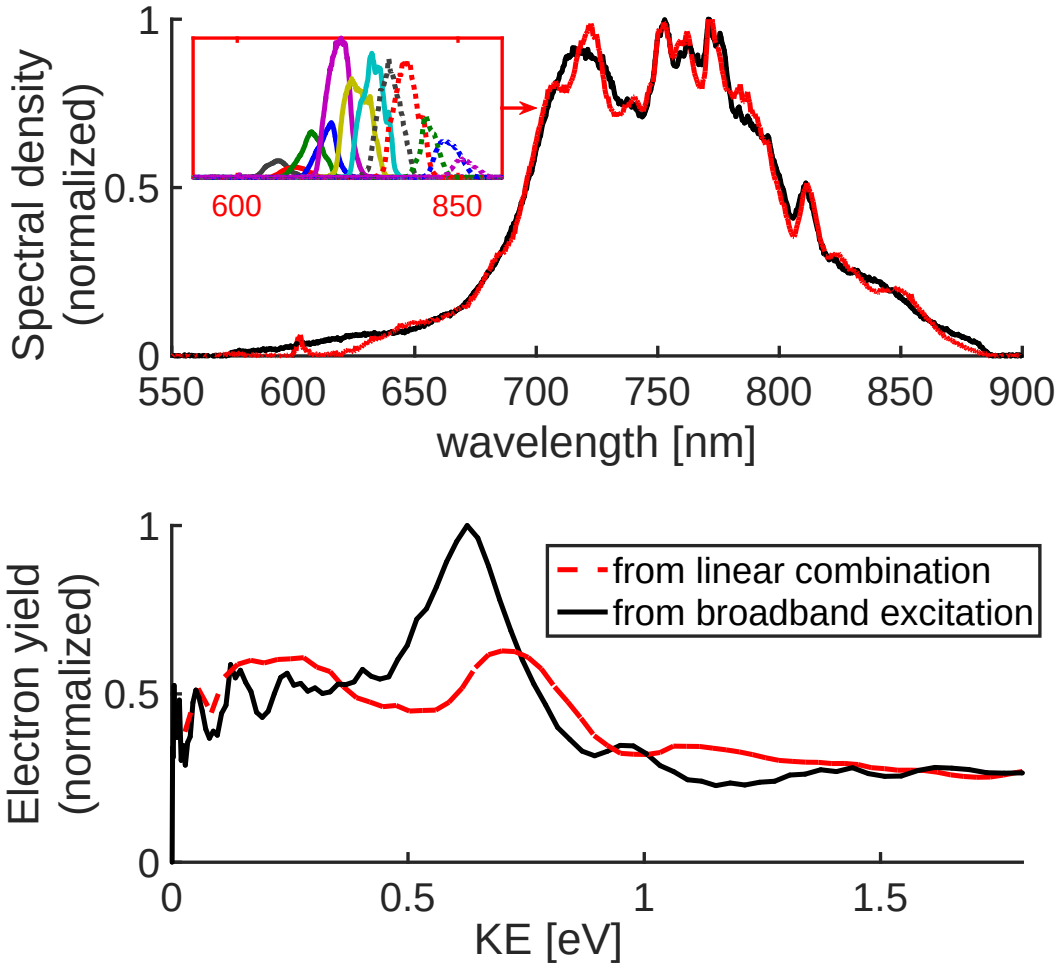

Figure 4.5: Top panel: Optical spectra for broadband pulse (solid black line) and the result of summing narrowband spectra (dashed red line). Bottom panel: photoelectron spectra of CH_2IBr acquired with full bandwidth optical spectrum (solid black line), and the result of forming a linear combination of photoelectron spectra each acquired with narrowband optical excitation (dashed red line). The latter are added in proportion to their spectral weights as shown in the inset and described in the text.

A second test performed was to vary the pulse duration while keeping the spectral content the same. This can be accomplished by placing a second-order spectral phase (chirp) on the broadband pulse, while varying the pulse energy to maintain a roughly constant yield. The second order phase was controlled by changing the grating separation in the compressor (figure 2.9). In the top panel of figure 4.6, photoelectron spectra measured in coincidence with the parent ion, CH_2IBr^+, are shown for a transform-limited (TL) pulse (black curve) and for chirped pulses with similar magnitude of the phase coefficient, but opposite sign (blue and red curves). As discussed in chapter 3, only peaks associated with the nondissociative ionic states, D_0 and D_1 are expected to be present in the spectra. Indeed, for any of the chirps, the peak at 1.05-1.2 eV can be assigned to the ground ionic state D_0, while the peak at 0.7 - 0.85 eV can be assigned to the first excited ionic state, D_1. The origin of the broad feature between 0.1-0.6 eV for negative chirp (blue curve) is not fully understood. It is surprising that it is present in the photoelectron spectrum for a negatively chirped pulse but not for the positively chirped or transform-limited cases. Intensity-dependent measurements for a transform-limited 30 fs pulse hint at a nonresonant ionization channel to D_1 in that

kinetic energy range (see figure 3.7), hence a tentative assignment is made accordingly. However, more data and calculations are necessary for a firm conclusion. The data shows that the suppression of D_0 takes place only for a transform-limited, short pulse, while for both positive and negative chirps, significantly more population is transferred to D_0. This corroborates the conclusion drawn above in that not only the spectral content of the pulse matters, but also whether this content adds up coherently to produce the shortest pulse.

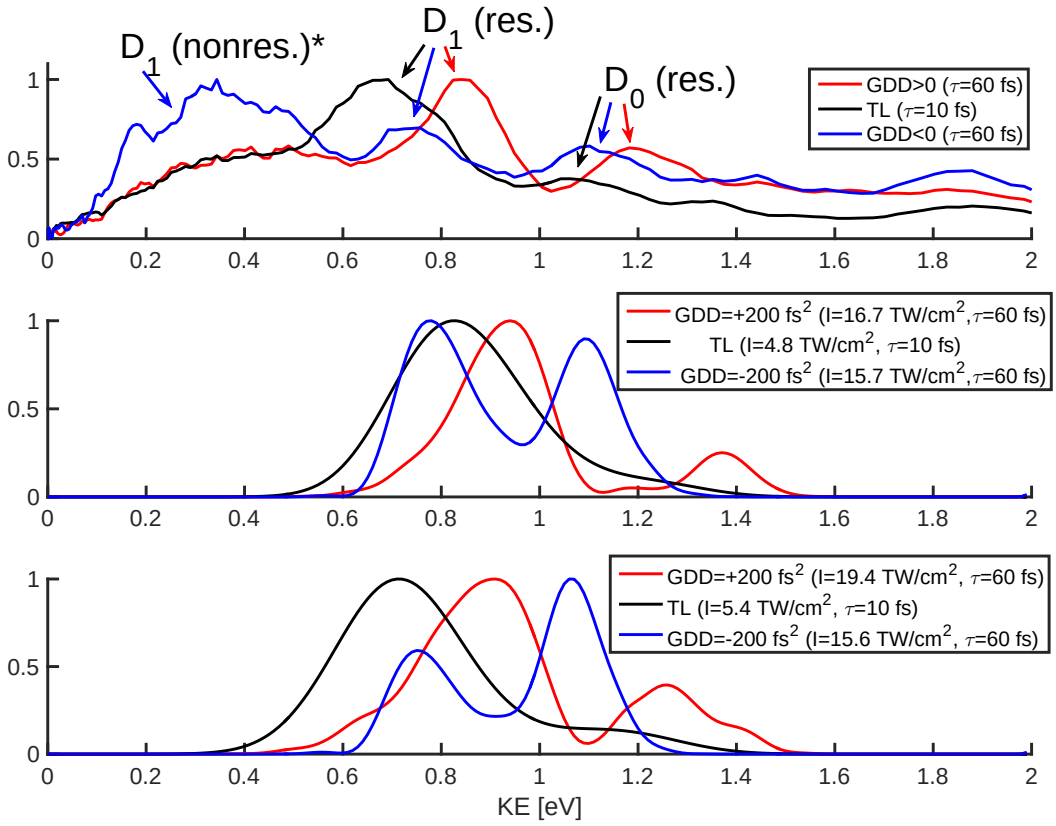

Figure 4.6: Top panel: photoelectron spectra in coincidence with the parent ion, CH_2IBr^+, for broadband excitation with different second-order spectral phase coefficients. Spectra are normalized to the maximum value. Peaks assigned to the ground and first excited ionic states (D_0 and D_1, respectively), where resonant (*res.*) and nonresonant (*nonres.*) channels are indicated. Middle panel: Calculated photoelectron spectra for the similar chirps and pulse durations as on top panel; ν_{laser}=390 THz. Bottom panel, same as the middle panel, except ν_{laser}=383 THz.
The model only included resonant excitation channels associated with D_0 and D_1; for details, see text. Legend lists the GDD parameter, intensity and pulse duration for the coupling field in the simulation for each simulated curve.

It is worth noting that there is a $\approx$ 0.15 eV shift in the peak location going from transform-limited pulse to positively chirped pulse. This shift was reproduced with a simple zero-dimensional model (with no vibrational dynamics included) constructed as a 5-level system (see fig 4.7a): a neutral ground state, 2 intermediate excited states and 2 ionization continuum ladders, representing D_0 and D_1. The intermediate excited states $|1\rangle$ and $|3\rangle$ were each multiphoton-coupled to the neutral ground state and to one of the continuum ladders ($|2\rangle$ and $|4\rangle$, respectively), serving as "stepping stones" for resonantly enhanced ionization. $|1\rangle$ and $|3\rangle$ were also coupled by a unidirectional (non-Hamiltonian) nonadiabatic coupling;

this enabled field-independent transfer of population from $|3\rangle$ to $|1\rangle$, but not the other way. The purpose of this is to phenomenologically include the effect of nonadiabatic coupling between states which would otherwise arise during nuclear wavepacket motion in a real molecule when potential energy curves cross as a function of nuclear geometry. The motivation behind this model is elaborated in section 4.4, where also an improved, 1D model (involving nuclear dynamics in addition to strong field coupling of states and ionization) is presented to understand the data on figure 4.1. However, it is beneficial to work with reduced, 0D models too, to separate the phenomena whose understanding relies on the details of nuclear wavepacket motion from those whose doesn't. (There is of course a correspondence between the states in the 0D and 1D models, which can be listed as: $|0\rangle \leftrightarrow S_0$, $|1\rangle \leftrightarrow R_0$, $|3\rangle \leftrightarrow R_1$, $|2\rangle \leftrightarrow D_0$, $|4\rangle \leftrightarrow D_1$.)

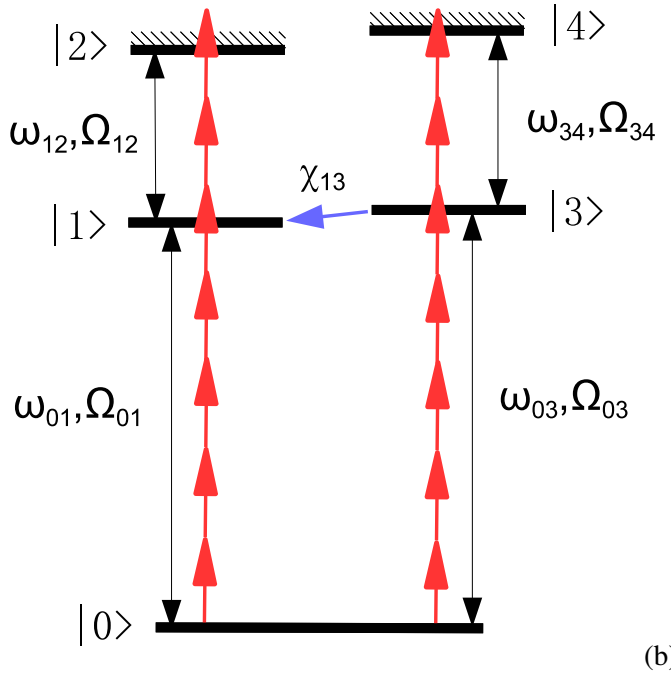

(a) Energy level diagram.

Parameter	Value
ν_{01}	1860 THz
ν_{03}	1920 THz
ν_{12}	480 THz
ν_{34}	575 THz
N_{01}	1 THz
N_{03}	10 THz
N_{12}	20 THz
N_{34}	20 THz
χ_{13}	7.5 THz
$\nu_1 = \nu_2 = \nu_3$	180 THz
I_{ref}	12.78 $\frac{TW}{cm^2}$

(b) Parameters used in the model. Comparing the values in the table to the quantities on the diagram to the left, note that $\omega_{mn} \equiv 2\pi\nu_{mn}$, $\Omega_{mn} \equiv 2\pi N_{mn}$.

Figure 4.7: Zero-dimensional model for describing ionization to the ground and first excited ionic states in CH_2IBr.

The states were allowed to Stark-shift in the field, and depending on the laser pulse parameters, that lead to significant restructuring of the spectra, shown on the middle panel of figure 4.6. Details of the framework underlying the model can be found in [44], while the parameters used are shown in table 4.7b.

The shift of the peak locations can be intuitively understood in the following way. The quadratic spectral phase on the laser pulse is responsible for rearranging the time ordering of the different colors making up the pulse. For a positive quadratic phase (positive GDD parameter), the instantaneous frequency as a function of time is monotonically increasing; more pictorially we can say that "red spectral components arrive earlier, blue components later". Hence at early times during the pulse, population transfer to the intermediate state $|3\rangle$ as the dominant process, proceeds using lower energy photons. Later during the pulse, when sufficient population is built up on the intermediate state and ionization becomes substantial, higher energy photons will drive those transitions. Reminding ourselves that the kinetic energy is determined by $K = nh\nu - I_p - U_p$, we will see increased kinetic energy compared to the transform-limited case because of the temporary increase in $h\nu$ (assuming U_p is roughly the same for the cases with and without chirp). The electron kinetic energy is increased, so the peak shifts to higher energies compared

to the transform-limited case. Similarly, negative GDD parameter results in shift to lower kinetic energies. This picture is supported by the calculations shown in the middle panel of figure 4.6, carried out for a central laser frequency of ν_{laser}=390 THz. The data is consistent with the peaks for positive GDD being shifted to higher energies than for the TL and negative GDD case. Comparing the latter two however, the relative peak positions do not match up with expectations drawn from the mechanism described above. Though so far no simple explanation has been found, calculations for ν_{laser}=383 THz were able to reproduce the relative shift of the peak positions between the negatively chirped and transform-limited cases, as shown on the bottom panel. A dynamic interplay between detunings and Stark-shifts "locks" the position of the peaks in case a chirp is applied, but not for the transform-limited case; hence only the latter shifts to lower kinetic energies when the laser frequency is tuned to the red.

4.4 Numerical Simulations and Interpretation

The observations described above suggest that there is some molecular dynamics which leads to both ionic states being populated, and if the pulse is shorter than the timescale for this dynamics, then only a single ionic state is populated. As the photoelectron spectrum is determined at the moment the electron is born in the continuum (i.e. it is not affected by possible subsequent dynamics in the molecular cation), an argument can be made that the dynamics leading to the selectivity must be neutral dynamics, involving an excited neutral state en route to the ionization continuum. As in earlier work which established the importance of dynamically Stark-shifted resonances [38, 36, 40] in strong-field molecular ionization [40, 33, 47], the intensity and wavelength dependent measurements presented here indicate that neutral Rydberg states Stark shift into resonance during the ionization process. The correlation between a neutral Rydberg state and low lying states of the molecular cation is typically large for only a single cationic state with a similar configuration of the core—i.e. the Dyson norm for a given neutral state is large for a single low lying state of the cation, and close to zero for other states [48]. While Dyson correlations can be poor for low lying neutral states in strong-field ionization, they are better for higher lying states of the neutral where the electron which is removed during ionization does not interact with the ionic core very much and does not modify the core configuration. This means that once an intermediate neutral Rydberg state comes into resonance, it typically couples to a single ionic continuum [47]. Thus, for resonance-enhanced ionization to multiple continua, as is the case for a $\approx$40 fs pulse, multiple intermediate states must be involved in the ionization dynamics.

Earlier work considered resonance enhanced ionization with separate uncoupled intermediate states for each ionization continuum [47]. Here, this model is extended to include coupling between the intermediate states, and the new measurements suggest that separate uncoupled intermediate resonances cannot account for the observed pulse duration dependence. If the bandwidth associated with different pulse durations were to select between different independent resonances, then one would expect to find a single ionic continuum favored for a long pulse (narrow bandwidth) rather than for a short pulse (broad bandwidth), since a shorter pulse contains a larger bandwidth, which would provide less selectivity between separate resonances. Furthermore, frequency-dependent measurements of the ionization yield such as the ones illustrated in figure 4.4 indicate that when there is resonance enhancement of the ionization yield, then it is through a single neutral state correlated with D_1.

While in principle both laser-driven resonance [15] and non-adiabatic dynamics could be responsible for coupling excited states, given the frequency-dependent measurements shown in figures 4.4 and 4.5, and motivated by earlier work [49], the focus will be on non-adiabatic dynamics as an explanation for the measurements shown in figures 4.1 and 4.2. Tamás Rozgonyi[1] carried out calculations for CH_2IBr that

[1]Research Centre for Natural Sciences, Hungarian Academy of Sciences, Budapest, Hungary

included non-adiabatic coupling between excited states which support the idea that molecular dynamics drives the switching between continua as a function of pulse duration.

Before modeling the strong-field ionization with numerical integration of the time-dependent Schrödinger equation (TDSE), Tamás Rozgonyi also carried out *ab initio* electronic structure calculations at the MS-CASPT2 level of theory [50] in order to determine which electronic states play a crucial role in the ionization process [2]. The strong field ionization simulations are based on a simple model [44] which includes Stark shifted intermediate neutral resonances. This model is now extended to include vibrational dynamics and non-adiabatic coupling between multiple intermediate neutral states, as considered in earlier calculations for weak (perturbative) laser fields [49]. CH_2IBr will be considered, for which the most detailed measurements and calculations have been made.

As prior measurements suggest that resonance enhancement occurs at the five-photon level [44], Rydberg states (R_0, R_1 and R_3) $\approx$8 eV above the ground state are considered. These are correlated (i.e. have similar electronic configurations) with the low-lying ionic states (D_0, D_1 and D_3), and their coordinate dependence follows those of the ionic states with which they are correlated. It is then considered whether any nuclear coordinates lead to coupling between these states. While the potential energy curves of the Rydberg states around 8 eV are largely parallel as a function of most vibrational coordinates, one particular mode has been found (CH_2 wagging) along which motion leads to degeneracy (and therefore to population transfer via non-adiabatic coupling) between states correlated with D_0, D_1 and D_3. The potential energy curves of these states along this normal mode coordinate are shown in Figure 4.8. In the calculations, population excited to R_1[3] can relax to R_3 and R_0 via rapid nuclear dynamics and non-adiabatic coupling. Based upon matches of the computed energy differences and similarities between electronic configurations, R_0, R_1 and R_3 are coupled to D_0, D_1 and D_3 respectively.

The strong-field ionization calculations produced the photoelectron spectrum as a function of pulse duration, as in the measurements. The energies of the resonant intermediate states were based on the electronic structure calculations and comparison with experimental spectra. Laser parameters, such as the intensity, central frequency and pulse duration, were based on experimental parameters[4].

As the $S_0 \rightarrow R_1$ resonance dominates, population is initially transferred from S_0 to R_1. As figure 4.8 illustrates, motion along the CH_2 wagging mode couples states R_0, R_1 and R_3. The Franck Condon point (FC, minimum of S_0) is close to the R_1/R_3 crossing, leading to rapid population transfer from R_1 to R_3 ($\lesssim$5 fs). Within $\approx$10 fs the wave packet on R_3 can proceed to the R_3/R_0 crossing. Thus, for a long pulse, ionization can proceed to a mixture of the ionic states D_0, D_1 and D_3 coupled with the three neutral states R_0, R_1 and R_3. While the measurements show evidence of ionization to all three of these states, the competition between D_0 and D_1 is highlighted because the measurements are cleanest for these states. In the limit of a short laser pulse, one might expect D_1 (which is correlated with R_1) to dominate the ionization yield, since R_1 can shift into resonance and there is insufficient time for the wave packet to move away from the FC on R_1 during the ionization. The ionization calculations aimed to test this hypothesis.

As the top right and middle panels of figure 4.8 illustrate, the photoelectron spectrum for a long pulse (40 fs) shows peaks corresponding to D_0 and D_1, whereas the photoelectron spectrum for a 10 fs pulse shows a single peak corresponding to D_1 only. This is in agreement with the results shown in figure 4.1, which contain two peaks corresponding to D_1 and D_0 for a long pulse and a single peak corresponding to

[2]Details on the electronic structure calculations are given in the supplementary information of our manuscript to appear in Physical Review Letters.

[3]Based on experimental data, R_1 is most strongly coupled to S_0 via the laser: figure 4.4 shows that ionization mostly leads to populating D_0, except for wavelengths for which D_1 is populated due to coupling to an intermediate resonance.

[4]Again, details on the parameters used for the calculations, such as coupling strengths (multiphoton Rabi frequencies), are given in the supplementary information of our manuscript to appear in Physical Review Letters.

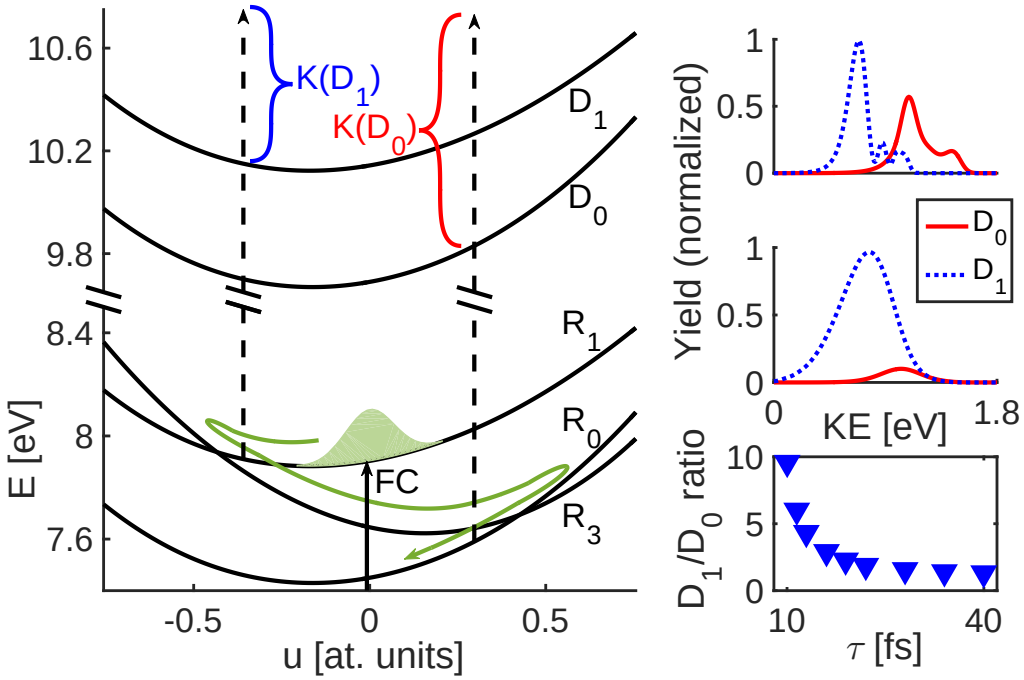

Figure 4.8: Left panel: calculated potential energy surfaces for CH_2IBr along the CH_2 wagging mode. FC: Franck-Condon point for excitation from the minimum of S_0 (u=0). Upper right panel: calculated photoelectron spectra for 40 fs pulse. Middle right panel: calculated photoelectron spectra for 10 fs pulse. Bottom right panel: calculated D_1/D_0 yield ratio as a function of pulse duration τ.

D_1 for a short pulse. The bottom right panel shows a decreasing D_1/D_0 ratio as a function of increasing pulse duration, in agreement with the results shown in figure 4.2.

One aspect of the measurements which is not reflected in the calculations is the width of the peaks in the PES as a function of pulse duration. The measurements show relatively narrow peaks for both short and long pulse durations, while the calculations show peaks which broaden as a function of decreasing pulse duration. This latter is a behavior in line with the properties of Fourier transform: ionization at the peaks of the oscillating electric field is a periodic event, and if it is confined to shorter time intervals (in this case the length of the laser pulse envelope), then it should result in broader peaks in the kinetic energy distribution. The fact that it is not observed in case of CH_2IBr can point to either systematic error in the measurement, or to a physical cause which in itself is worth investigating, or both.

Since the peak that shows a narrow width independent of pulse duration is associated with a resonantly enhanced ionization channel, it is natural to turn to nonresonant ionization channels and study their behavior as a function of pulse duration. This was the motivation behind a series of measurements that were carried out on CS_2. Briefly, CS_2 is a linear molecule with an ionization potential of 10.1 eV for the ground ionic state (D_0), with the first excited ionic state 2.6 eV above it. This is a significant difference in energy and leads to ionization to D_0 exclusively for a fairly large range of intensities. More importantly, this channel is nonresonant for lower laser intensities, leading to peaks in the spectrum that shift ponderomotively. (This fact was relied upon in section 3.3, where an estimate is given to the value of the ponderomotive energy in the laser focus.) The bottom panel of figure 4.9 shows the result of an experiment carried out with pulses of varying durations. On the top panel, the corresponding optical spectra are shown. The former include yield in the region $\pm 30^\circ$ around the laser polarization, and are

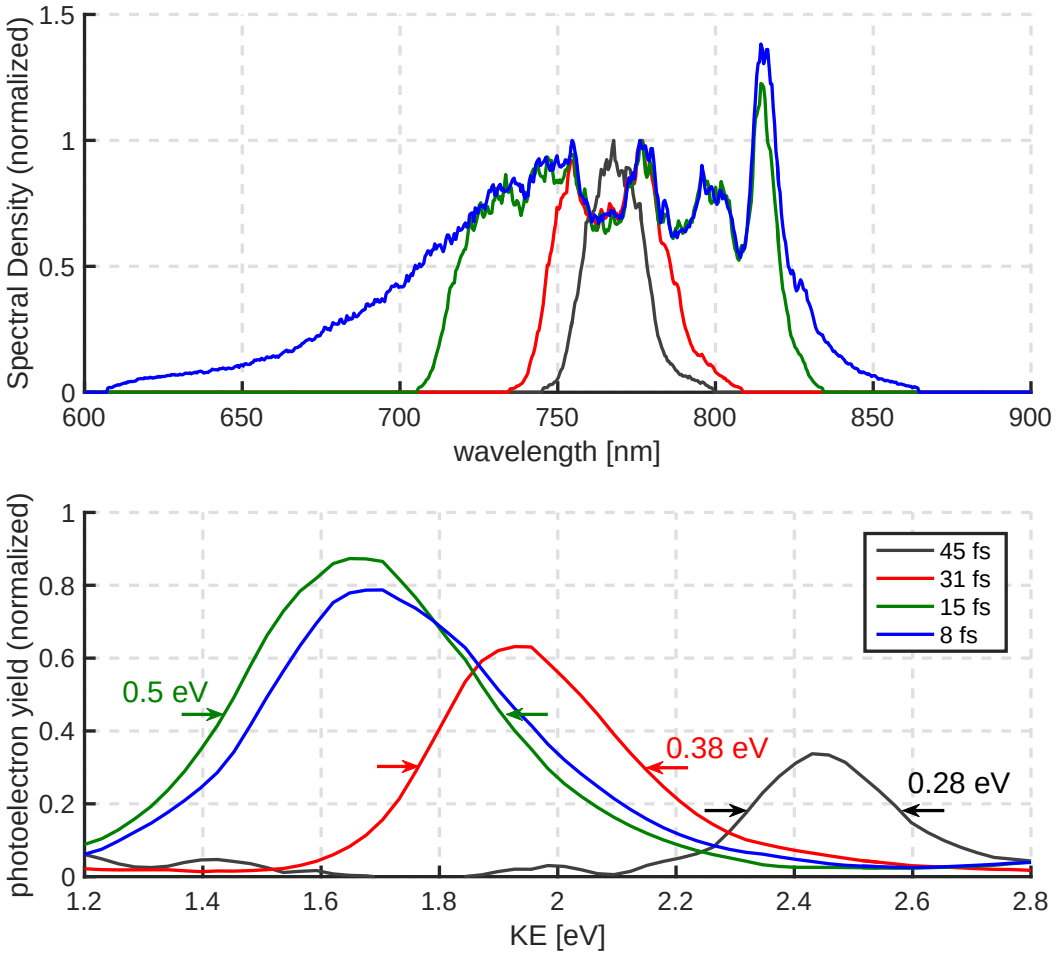

Figure 4.9: Top panel: Optical spectra of the ionizing pulses; Bottom panel: Photoelectron spectra of CS_2, curves with different colors correspond to the optical spectra on the top panel. The full width at half maximum (FWHM) value are indicated for three of the curves, showing a monotonic increase with increasing optical bandwidth. Legend: pulse duration calculated from the optical spectra. The photoelectron spectra are normalized to the total yield (area under each curve, full curves not shown for clarity).

normalized to the total yield. For the sake of clarity, only a selected range of kinetic energies is shown. The legend is shared by the two panels, and it lists the calculated pulse duration based on the measured optical spectra. Turning our attention to the photoelectron spectra, the significant shift of the D_0 peak location has to be mentioned; this is due to a combined change in the peak intensity and the photon energy across the different measurements. More importantly however, the monotonic increase of the FWHM peak width is noted, from 0.28 eV to 0.5 eV, while the pulse duration reduces from 45 to 15 fs. This is attributed to the ionization process being confined to a shorter temporal window. The increase in peak width is negligible for pulse durations below 15 fs. Such saturation may suggest that even though the spectrum is broadened during the experiment, the pulse did not actually get shorter. Independent FROG measurements of the pulse duration however make this scenario seem unlikely, pointing to an interpretation which relies on a peculiar response of CS_2 to short-pulse excitation. In any case, the measurements demonstrate two things. The first is that there is no inherent systematic error in the data acquisition or in the way the data is processed that would altogether prohibit observing the phenomenon

of peak broadening. The second is that the way CH_2IBr behaves has physical origins worth investigating further.

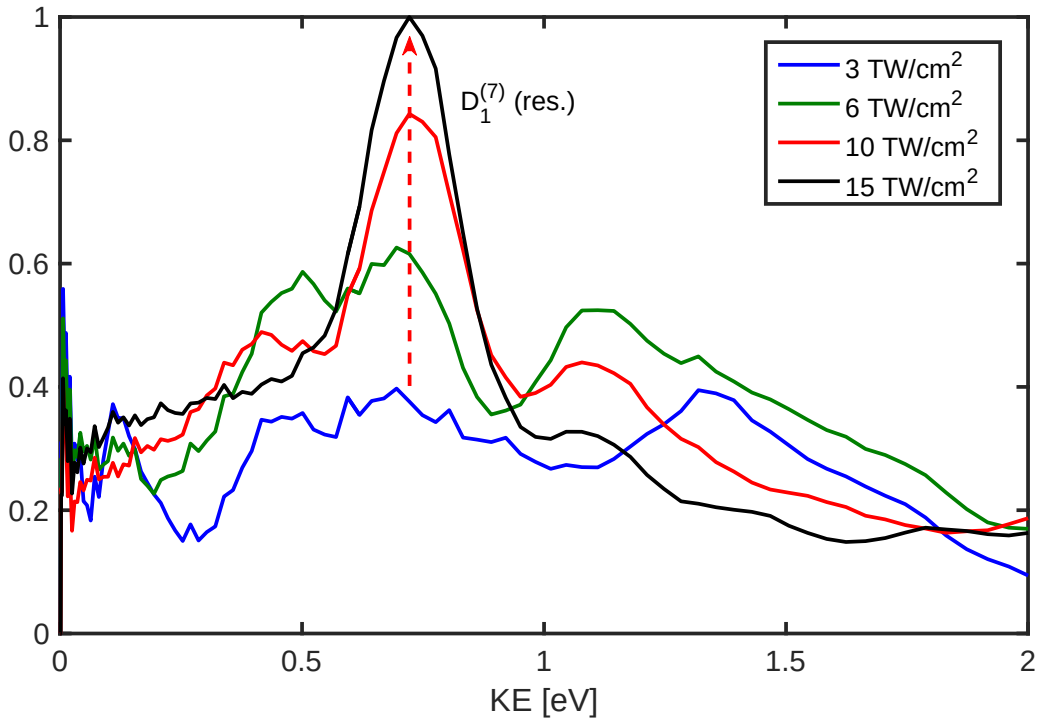

Figure 4.10: Photoelectron spectra of CH_2IBr with broadband excitation for different peak intensities (see legend). Spectra are normalized to the total yield (area under each curve).

At this point it is asked whether the narrow width of the D_1 peak in CH_2IBr has to do explicitly with the fact that the ionization channel is resonantly enhanced. An idea to answer the question is to study the spectrum with the resonant channel turned off, and when only nonresonant contributions are observed. To this end, keeping the optical bandwidth broad, the intensity is turned down in a number of steps to the point where there is essentially negligible ionization (an electron every two hundred laser shot). Data was acquired in counting mode, and the result is shown on figure 4.10. The different curves were recorded for different intensities (indicated in the legend). For the lowest intensity (3 $\frac{TW}{cm^2}$, black curve), two broad peaks are prominent. One at ≈1.35 eV, the other between 0.5 and 0.7 eV. Based on previous discussion in this chapter, these can be assigned to D_0 and D_1, respectively. The considerable width (>0.3 eV) suggests that both channels are nonresonant. Indeed, as the intensity is increased to 6 then 10 $\frac{TW}{cm^2}$, the peak for D_0 shifts ponderomotively to lower kinetic energies. The peak for D_1 however, develops a narrow subpeak centered at 0.72 eV, which eventually becomes the dominant contribution at 15 $\frac{TW}{cm^2}$. Since this subpeak is narrow (≈0.15 eV), and does not shift with intensity, its origin is clearly resonant ionization to the first excited ionic state. Also, since the intensity is set close to 15 $\frac{TW}{cm^2}$ when making the measurements for figure 4.1, it is now clear that the laser drives the same resonant transition both in case of the pulse duration-dependent and in case of the intensity-dependent experiments. Based on the calculations outlined above, one can identify the resonant neutral state in question with R_1 on figure 4.8. Though it is still not clear how the peak stays narrow at high intensities despite the short duration of the pulses, it is better understood under what conditions it does so. However, the intensity dependent data on figure 4.10 certainly highlights the fact that at higher intensities, populating D_1 is resonantly enhanced even for a short pulse, while for low intensities roughly equal amount of population is transferred to D0

and D_1. This is consistent with the idea that ionization to D_0 (but not D_1) involves field independent coupling between the intermediate neutral states, as in the model described above (figure 4.8).

As a final point, it has to be mentioned that the interpretation of the pulse duration dependence relies on neutral state resonances enhancing the ionization yield. Thus one would expect that there is no change in the ionization yield for different ionic continua with pulse duration if there are no important resonances. The pulse duration-dependent measurements in CS_2 (in figure 4.9) provide additional test for this. It can be seen that the photoelectron spectrum did not change substantially with pulse duration (apart from an expected broadening and shifting of the peaks, as discussed earlier; however, the set of ionization continua accessed remained the same), as one would expect based on our interpretation which relies on dynamics in intermediate neutral states.

Chapter 5

Zero Energy Structure in Photoelectron Momentum Distributions

5.1 Introduction

Very low energy photoelectrons are observed in the photoelectron momentum-space distributions of different atomic and molecular systems (see, e.g. figure 2.14), forming the so-called zero energy structure (ZES). These electrons manifest themselves as a narrow (width $\approx$0.6 meV) "dot" in the center of the collected Velocity Map Images, where the TOF axis intersects the plane of the detector. The origin of these electrons is believed to be high-lying Rydberg states [51, 52] which are populated during the laser pulse and then ionized in one way or another such that once free, the electrons coming from this particular channel have negligible energy compared to the rest of the ionized electrons.

Experiments have been done in the mid-infrared (at a wavelength of 2 μm), identifying the zero energy structure in the momentum distribution of strong-field ionized electrons in argon [51]. The structure is composed of electrons with a magnitude of the momentum on the order of the instrumental resolution of the reaction microscope used, i.e. 0.01 atomic units. Using a numerical model, the authors of [51] verify that the ZES in their data can be attributed to a two-step process. First, the electrons undergo frustrated tunnel ionization [53]: they tunnel through the tilted Coulomb potential, get accelerated by the laser field which turns them around when the field changes direction. This potentially puts them on a course for recollision with and recapture by the ion core. High-lying excited states are thus populated. In the second step these states are eventually ionized by the field of the electrostatic lens. This interpretation is consistent with the fact that the Keldysh-parameter for the experiment was $\approx$0.3, which is in the tunnel regime.

ZES was also observed in another experiment, exciting neon using circularly polarized, 15 fs pulses at a wavelength of 800 nm [52]. In this case however, the authors claim that ionization in the field of the plates is preceded not by tunneling and recapture of an electron, but by multiphoton transition to high-lying neutral Rydberg states [1].

We can see that there can be two steps identified so far for producing ZES electrons: first, high-lying Rydberg states leading up to one of the ionization continua have to be populated; second, at least one electron needs to be ionized without imparting significant momentum to it. The question arises whether the second step can be substituted with something other than field-ionization by the electrostatic field of

[1] I have to note that this interpretation is not consistent with the fact that the Keldysh parameter is only 0.3 for one of the experiment in the paper on neon showing the ZES. Circularly polarized pulses at 800 nm with a peak intensity of 800 $\frac{TW}{cm^2}$ were used.

the imaging plates. The aim of this chapter is to extend the body of observations in this matter, and to this end we present data acquired in a variety of different circumstances using velocity map imaging of photoelectrons. The possible mechanisms for producing ZES electrons are discussed and compared with available data.

Throughout this chapter, mostly raw VMI images will be shown, with minimal or no processing. Experiments were performed using laser radiation having linear or circular polarization, at a range of intensities, bandwidths and central frequencies. Systems in which ZES electrons are observed included both atoms (Argon) and molecules (CH_2IBr, CS_2 and α-terpinene).

5.2 The first step: populating Rydberg states

5.2.1 The case of Argon

For argon, a typical outcome of a measurement is shown on figure 5.1a, in which the photoelectrons were measured in coincidence with Ar^+ as a function of transverse momentum components parallel (p_z) and perpendicular (p_y) to the laser polarization. Linearly polarized, 30 fs, transform-limited pulse was used with a central wavelength of 780 nm and $\approx 20 \frac{TW}{cm^2}$ peak intensity. Coincidence detection separated electrons coming from the ionization of argon from those coming from the background gas in the chamber. The zero energy structure is clearly visible, as a sharply peaked feature at p_z=p_y=0. ZES electrons constitute $\approx$0.2% of the total yield in this case, which, as we shall see, is a typical number, but shows some variation with laser pulse parameters. Although detailed analysis of the photoelectron peaks at higher energies is not the aim of the present discussion, a series of narrow rings, visible at radii $|p| = \sqrt{p_y^2 + p_z^2}$ =0.3 to 0.35, are pointed to. These are consistent with resonantly enhanced 12-photon ionization to either the ground ionic state ($3s^2 3p^5$[J=$\frac{3}{2}$], I_p=15.76 eV [54]) or the first excited ionic state ($3s^2 3p^5$[J=$\frac{1}{2}$], I_p=15.94 eV). (It is not straightforward to assign any resonantly enhanced peak, since its location in the spectrum is greatly influenced by the intermediate neutral state that shifts into resonance during the pulse.)

On figures 5.2a and 5.2b, the relative yield of the ZES electrons is shown as a function of peak intensity of the laser pulse, for linear and circular polarizations, respectively. For these measurements the amplifier output was sent through the pulse shaper which was used to control the diffracted power of the laser beam. The two sets of measurements were taken with the same range for the pulse energy. When calculating the peak intensity however, one has to take into account that it is a factor of 2 lower for circular polarization than for linear. The measured ratio is 0.2% at lower intensities ($<35 \frac{TW}{cm^2}$) for linear polarization, which is consistent with the data for 20 $\frac{TW}{cm^2}$, obtained in a separate experiment using coincidence detection (see figure 5.1a for the raw image).

Important to note that one can see significant yields for circular polarization, even though it is about a factor of 5 less than for the linear case at 40 $\frac{TW}{cm^2}$. If the Rydberg-ionization hypothesis is correct, then this argues for those states being populated via direct multiphoton ionization rather than via rescattering. This is because the probability of an electron recolliding with the ion core in a circularly polarized laser field is at least an order of magnitude lower than for linear polarization [55].

Increasing the intensity results in a drop in the relative yield: many more electrons will be ionized to higher kinetic energy channels than to zero energy channels. This could be explained with the transition to the Rydberg states being saturated above a specific intensity. In contrast, population can always be transferred to the continuum, and in that sense one can think of it as a "sink" of electrons.

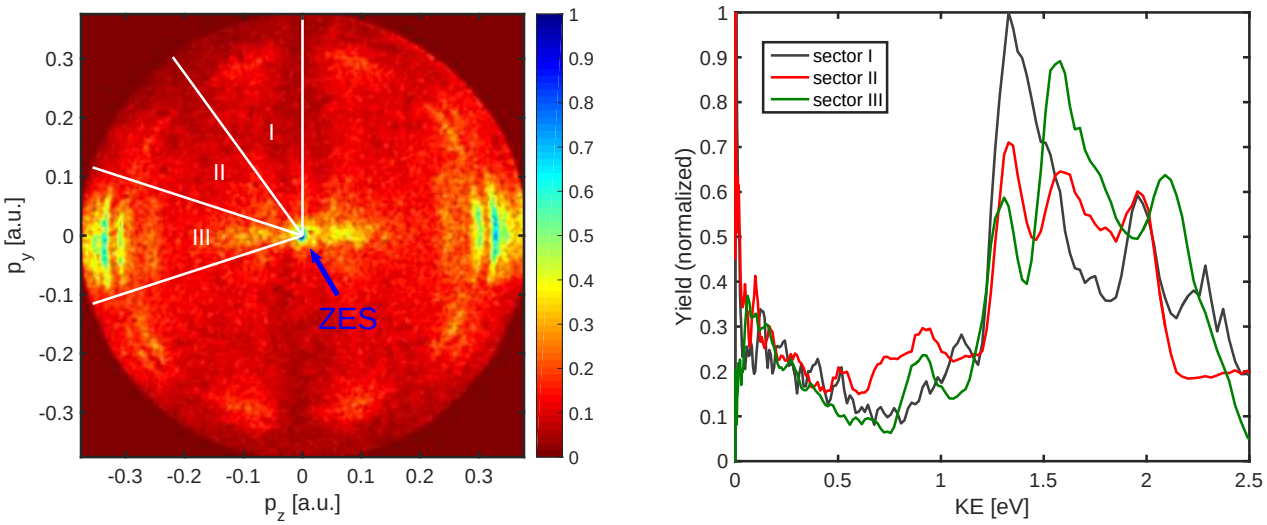

(a) Unprocessed VMI image with angular sectors indicated.

(b) Photoelectron Spectrum.

Figure 5.1: Measured photoelectron distribution in coincidence with Ar^+ for a 30 fs, transform-limited pulse with a wavelength of 780 nm, and $\approx 20 \frac{TW}{cm^2}$ peak intensity.

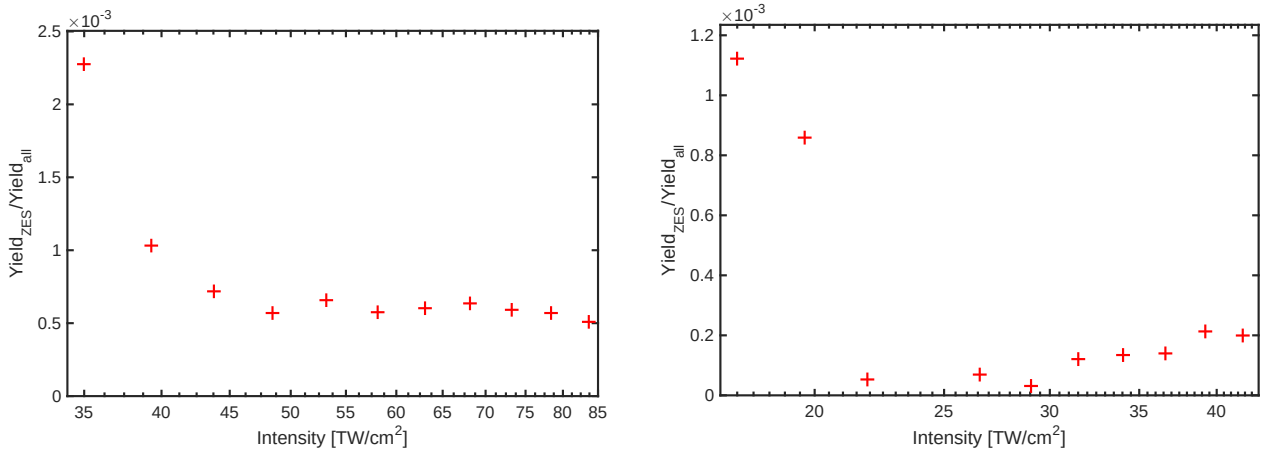

(a) Linear polarization.

(b) Circular polarization.

Figure 5.2: Ratio of yield of ZES electrons to all photoelectron yield of Argon as a function of intensity with transform limited 30 fs pulses at 780 nm.

5.2.2 The cases of CH_2IBr and CS_2

Next, the focus will be on molecular systems that exhibit ZES in the photoelectron velocity map images. On figures 5.3a and 5.3b it is shown for CH_2IBr and CS_2, respectively. CS_2 is an interesting case, because the intensity had to be raised above a certain value to clearly see the structure. As it will be shown, it is consistent with the argument made in section 3.3 that at low laser intensities resonances do not play a role during ionization to the ionic ground state. Hence, one doesn't expect to populate Rydberg states either.

Figure 5.4a and 5.4b show the yield as a function of intensity for CH_2IBr and CS_2, respectively.

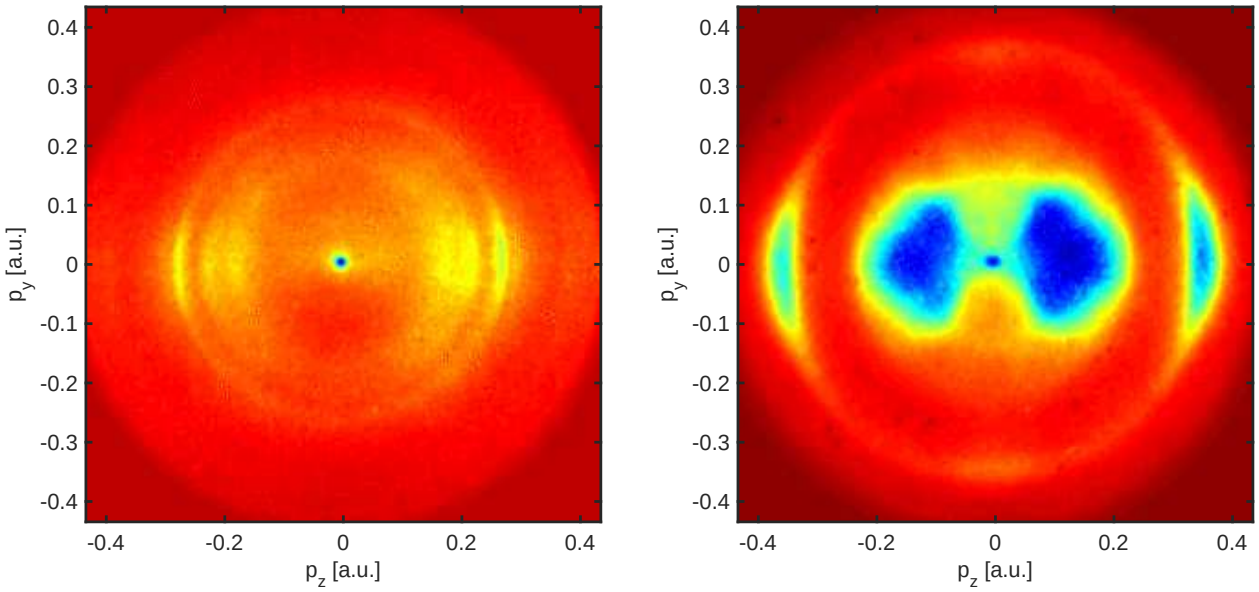

(a) Data on CH_2IBr using a peak intensity of 8 $\frac{TW}{cm^2}$. (b) Data on CS_2 using a peak intensity of 15 $\frac{TW}{cm^2}$.

Figure 5.3: Raw VMI images showing ZES for linearly polarized, transform limited 30 fs pulses at 780 nm.

Linearly polarized, 30 fs pulses were used to ionize the molecules. For CH_2IBr a very similar behavior as in argon can be observed: the relative yield of the ZES electrons is less than a percent, and it decreases with increasing intensity. As shown on the upper panel on figure 5.4a, there is a different power law-dependence of the ZES yield compared to the total yield: 4.5 and 6, respectively. This indicates that the multiphoton orders for the two ionization channels are different, and it is lower for producing ZES electrons.

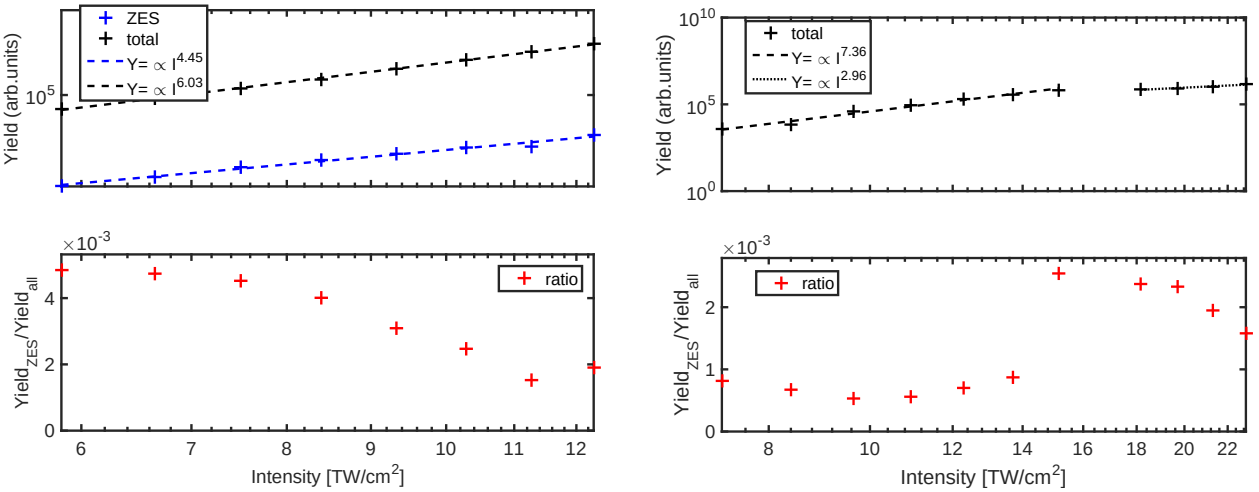

(a) CH_2IBr. (b) CS_2.

Figure 5.4: Ratio of yield of central dot to all photoelectron yield as a function of intensity with linearly polarized, transform limited 30 fs pulses at 780 nm.

In CS_2 however, the yield is very low for intensities $<14\ \frac{TW}{cm^2}$, and suddenly increases when the intensity rises above that value. The data suggests that Rydberg states are populated very inefficiently below this threshold. In this low intensity range, the total yield scales with an effective power of 7.46, as the fitting shows. This is consistent with nonresonant ionization with at least 7 photons. The way an effective number of 7.46 is arrived at can be understood as follows: with a photon energy of 1.6 eV, it takes at least 7 photons to overcome the ionization potential for the ground state, which is 10.1 eV. However, the total yield can in principle include multiphoton ionization channels with orders higher than 7, with progressively less yield as the order increases. The effective power is then determined by the yield-weighted average of all the orders above 7, resulting in 7.46 in this case. This is consistent with resonances not playing much of a role in the ionization for intensities below $14\ \frac{TW}{cm^2}$, only above. (It is just briefly mentioned here that inspection of the photoelectron spectra supports this interpretation. The shift of the peaks per unit increment in the intensity is significantly smaller for intensities above $14\ \frac{TW}{cm^2}$, suggesting subponderomotive shift due to the presence of neutral resonances.) It is also the higher intensity range when the ZES yield becomes appreciable, and this highlights the connection between it and the role of Rydberg resonances.

Let us now examine how this picture changes if the pulse duration is shortened by a factor of 3. Figures 5.5a and 5.5b show measurements for CH_2IBr and CS_2, respectively, that were performed using pulses derived from laser-driven filamentation and compressed to sub-10 fs using a grating compressor (details of the setup can be found in section 2.4).

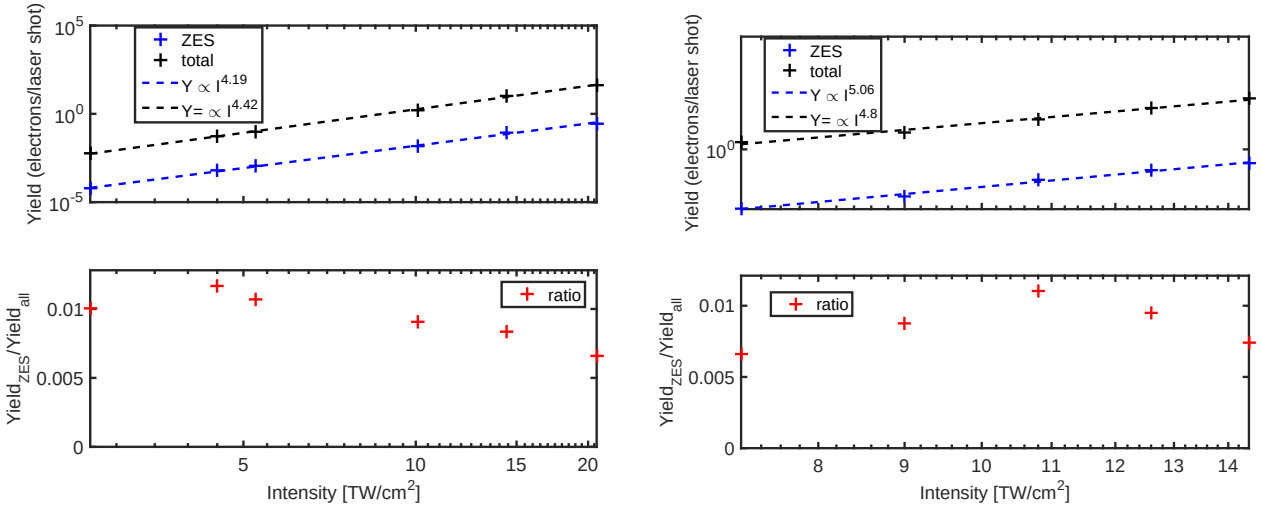

(a) CH_2IBr. (b) CS_2.

Figure 5.5: Ratio of yield of central dot to all photoelectron yield as a function of intensity with linearly polarized, transform limited 10 fs pulse.

In the top panel of figure 5.5a, the individual yields are shown along with a linear fit to each in case of CH_2IBr. Interestingly, the photon order for the ionization is much lower than for longer pulses: 4.4 instead of 6, while the order associated with the ZES electrons remained mostly the same. This indicates that the main mechanism for ionizing with short or long pulses is somehow different; in contrast, the process for creating zero-momentum free electrons is unchanged. The ratio of the yield, as shown on the bottom panel, decreases with increasing intensity, just as in case of the long pulses. However the rate at which it does so is much lower, because the difference between the photon orders for the ZES yield and the total yield are smaller for short pulses than for longer pulses.

For CS_2, the experiments with short pulses result in significant ZES yield, and this is in contrast with the observations using long pulses. The photon order of the yields, as shown on the top panel of figure 5.5b, is very similar to each other ($\approx$5), and lower than what is expected in case of nonresonant ionization. Ratio of the yields (figure 5.5b, bottom panel) is relatively high, $\approx$1%. This is reminiscent of the "above threshold"-behavior that we have seen for the case with longer pulses. It is possible that with short pulses a neutral state can come close to resonance at much lower intensities than with longer pulses. This is entirely conceivable, since a shorter pulse has larger bandwidth and hence more potential to couple states resonantly.

The transition from long to short pulse for a given intensity proves to be interesting, since there may be a way to capture at which pulse duration come any resonances into play. The details of the experiment are discussed in chapter 4. Briefly, pulses with broad bandwidth are generated in a laser-driven filament, and compressed in a grating compressor, resulting in sub-10 fs pulses for the full bandwidth. The pulse duration is controlled by blocking some of the frequency components in the compressor where the colors are separated spatially. Figures 5.6a and 5.6b show the result for the two systems. In the bottom panels the ratio of ZES yield to the total yield is plotted, while on the top, the number of electrons generated per laser shot, which is proportional to the total yield. While the aim was to keep the ionization yield (and hence the intensity) the same for different pulse durations, a variation of $\pm$30% is observed for both sets of measurements. In addition, for CS_2 two datapoints, corresponding to the longest pulses and hence narrowest bandwidth were taken with significantly different setting for the intensity, such that the yield is less than for the rest of the dataset by more than an order of magnitude. It is important to keep this in mind when interpreting the data, and avoid the confusion between pulse duration-driven and intensity-driven responses.

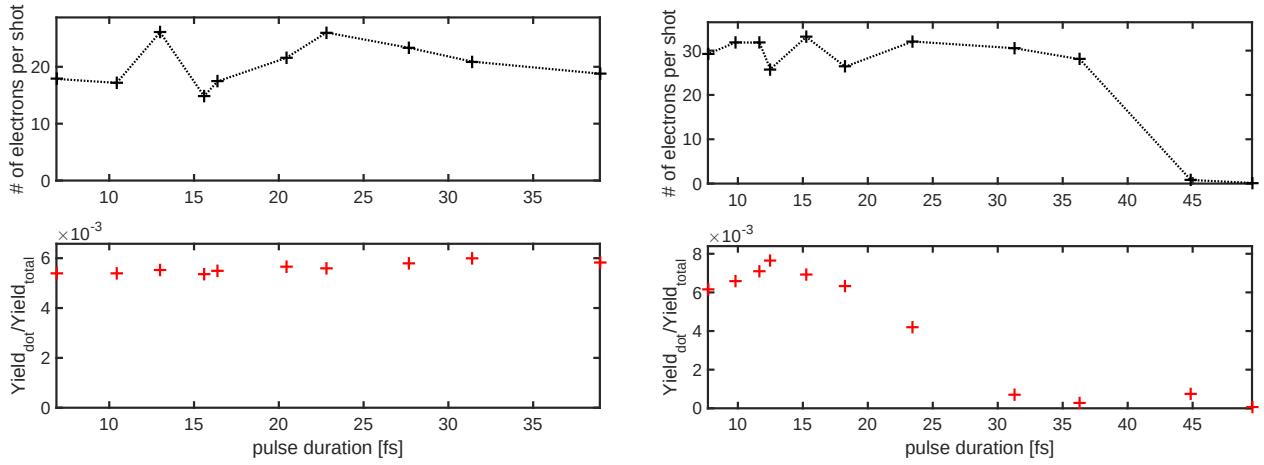

(a) CH_2IBr (b) CS_2

Figure 5.6: Bottom panel: Relative ZES yield as a function of pulse duration. Top panel: # of electrons per laser shot. Dotted line is a guide to the eye.

The bottom panel of figure 5.6a makes it clear that for CH_2IBr, the relative importance of the ZES electrons does not depend on the duration of the driving pulse. Whatever the mechanism is that produces them, it scales the same way with pulse duration as the mechanisms that produce all the other electrons. It has been shown in chapter 4 that as the driving pulse gets shorter, nuclear dynamics is frozen and the ionization channels that rely on them lose importance. It is not clear how this plays out exactly for the electrons that are born with zero momentum. However, the insensitivity of the ZES electron yield can be

taken as an indication that populating the Rydberg states which leads to their production does not involve nuclear dynamics (for instance, population is not transferred from one state to another via nonadiabatic coupling).

A very different picture can be found in CS_2, for which data is shown on the bottom panel of figure 5.6b. Focusing on pulse durations <38 fs, we find that even after taking into account the change in intensity, there is a strong variation in the relative ZES yield. We are already familiar with the extreme cases: for relatively low intensity, longer pulses produce low yield (figure 5.4b), while shorter pulses produce high yield (figure 5.5b). Here we can see a smooth transition in between, which is consistent with not being on resonance for a relatively low-intensity, 30 fs pulse, but coming into resonance as the pulse duration is decreased (the bandwidth is broadened).

Fragment-resolved measurements may add some further insight into what the underlying mechanism is for creating the ZES structure. Unprocessed momentum distributions recorded in coincidence with the parent and fragment ions, respectively, are shown on 5.7a and 5.7b for a 30 fs pulse and 5.8a and 5.8b for a 10 fs pulse[2]. All of the distributions show the appearance of ZES electrons, except for the one associated with the parent ion, CH_2IBr^+ for a 30 fs pulse. Looking at the photoelectron yield as a function of the pulse duration and fragment ions, there is a way to discriminate between certain sets of ionization-dissociation pathways available for the molecule during the laser pulse. At this point it is a worthwhile exercise to remind ourselves of what these are for the four different cases (for the states, see figure 4.8):

- 30 fs pulse, parent ion $\rightarrow$ no ZES (figure 5.7a):
  - Population transfer to $R_1 \rightarrow$ ionization to D_1.
  - Population transfer to $R_1 \rightarrow$ wavepacket evolution to $R_0 \rightarrow$ ionization to D_0.
- 30 fs pulse, fragment ion $\rightarrow$ ZES (figure 5.7b):
  - Population transfer to $R_1 \rightarrow$ ionization to $D_1 \rightarrow$ post-ionization transition to D_{2+}.
  - Population transfer to $R_1 \rightarrow$ wavepacket evolution to $R_0 \rightarrow$ ionization to $D_0 \rightarrow$ post-ionization transition to D_{2+}.
  - Direct ionization to $D_{2/3}$.
- 10 fs pulse, parent ion $\rightarrow$ ZES (figure 5.8a):
  - Population transfer to $R_1 \rightarrow$ ionization to D_1.
- 10 fs pulse, fragment ion $\rightarrow$ ZES (figure 5.8b):
  - Population transfer to $R_1 \rightarrow$ ionization to $D_1 \rightarrow$ post-ionization transition to D_{2+}.
  - Direct ionization to $D_{2/3}$.

Of course there are additional pathways that do not depend on the presence of the laser pulse; e.g. the wavepacket can transfer from R_1 to R_0 nonadiabatically even after the pulse has passed. So far there is no unambiguous way to correlate any single one from the above processes with the production of ZES electrons.

[2]For the two measurements involving short pulses, an error in determining the correct threshold for data acquisition resulted in a reduction of yield close to the center of the images.

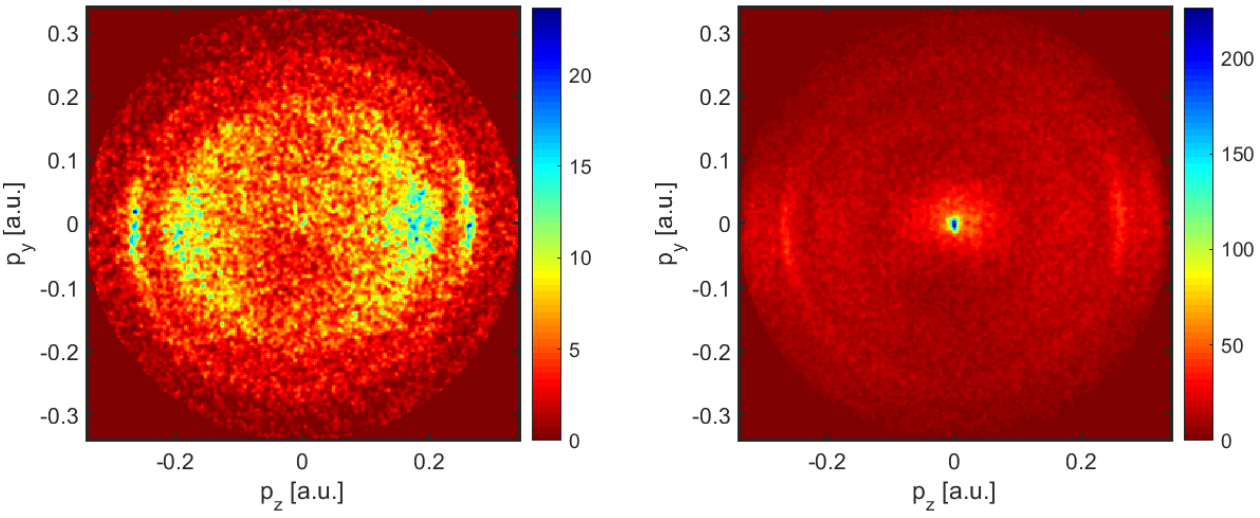

(a) The parent ion, CH_2IBr^+.

(b) The fragment ion, CH_2Br^+.

Figure 5.7: Photoelectron momentum distributions in coincidence with the parent ion and the most abundant fragment ion of CH_2IBr. Transform-limited 30 fs pulse with $\approx 8\ \frac{TW}{cm^2}$ and 780 nm central wavelength were used.

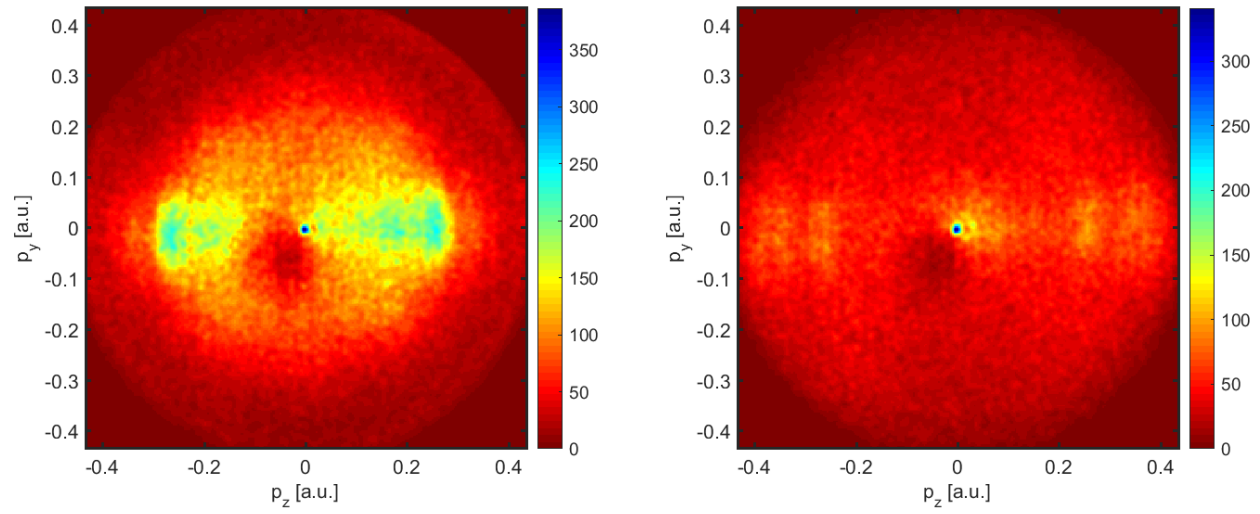

(a) The parent ion, CH_2IBr^+.

(b) The fragment ion, CH_2Br^+.

Figure 5.8: Photoelectron momentum distributions in coincidence with the parent ion and the most abundant fragment ion of CH_2IBr. Transform-limited 10 fs pulse with $\approx 9\ \frac{TW}{cm^2}$ were used.

5.3 The second step: ionization

So far only the first step—population transfer to high-lying Rydberg states—has been considered that leads to the production of zero-momentum electrons. Now we turn our attention to the second step, and ask what, possibly, is the mechanism for ionizing the trapped population.

In case of molecules, a scenario that fits naturally with the multiphoton picture is autoionization. It is well known that autoionization in molecules from a neutral electronic manifold to an ionic one can

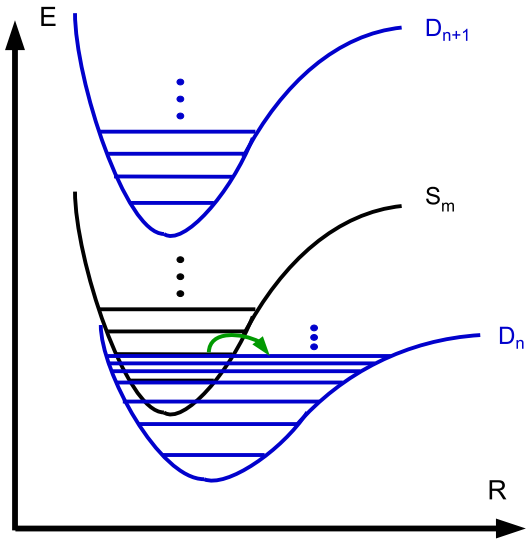

Figure 5.9: Autoionization (green arrow) from vibrational states on the neutral manifold S_m to ionic manifold D_n.

result in a different set of vibrational states being populated on the latter than on the former [56], so much so that the target ionic state may even lack bound vibrational levels, i.e. it can be dissociative, leading to fragmentation [57]. Now suppose that during excitation with the laser, population is transferred to a member of the neutral Rydberg series leading up to an excited ionic state. If there is an ionic continuum with an energy below that of the Rydberg state, the system can autoionize, producing an electron with low kinetic energy, while the rest of the excess energy could go into vibrations of the ion (see figure 5.9). However, as we have seen in section 5.2.1, the ZES can be observed in case of argon atoms, too, not just molecules. The only way the electrons can have low kinetic energy in this case is if autoionization involves only Rydberg states with energies very close to that of the target continuum (since there are no vibrations to store the energy difference), irrespective of laser pulse parameters. Since there is no reason to assume that this is the case in general, this mechanism cannot be the only explanation for the phenomenon.

The most widely accepted mechanism, as mentioned in the introduction, is field-ionization [58]. Field ionization is a mechanism during which population trapped in weakly bound states can "leak out" when the binding potential is tilted by an external field. The idea is illustrated, for the case of an atom, on figure 5.10b. As the field strength is increased, population from higher-lying states can escape. It is straightforward to calculate the index of the lowest-lying of such states for a Hydrogen-like atomic system. (The spacing of the energy levels of the Rydberg states in a molecule becomes very similar to that in atoms for states that lie close to the continuum.) In figure 5.10a, a slice through a tilted Coulomb potential along y=0 is shown; as it can be seen, there is a local maximum of the net potential: $V(x) = -\frac{Z}{x} - E \cdot x$, at finite distance from the atom (x_0), resembling a "saddle". Here *Z* is the atomic number, *E* is the magnitude of the electric field, and atomic units are used. We are looking for the value of the binding potential at the saddle point, $V(x_0)$. It is simple to show that $x_0 = \sqrt{\frac{Z}{E}}$ and $V(x_0) = -2\sqrt{Z \cdot E}$. This latter can be equated with the energy of states, $E_n = -\frac{Z^2}{2n^2}$ (where n is the principal quantum number) to find the lowest one that is made unbound.

$$-2\sqrt{Z \cdot E} = -\frac{Z^2}{2n_{min}^2} \rightarrow n_{min} = \frac{Z^{3/4}}{2E^{1/4}}$$

In the experiments, $E = 124\,\frac{V}{cm} = 2.4 \cdot 10^{-8}$ a.u. is a typical field strength for the imaging plates (for

$V_{rep} = -600$ V, $V_{ext} = -424$ V). In this case for Hydrogen (Z=1), states with n_{min}=40 and above get field ionized. Increasing the field strength by a factor of 4, one can ionize n_{min}=28 and above. Since the experiments are typically performed on molecules with lower binding potential, one can expect to ionize from states with lower index in general.

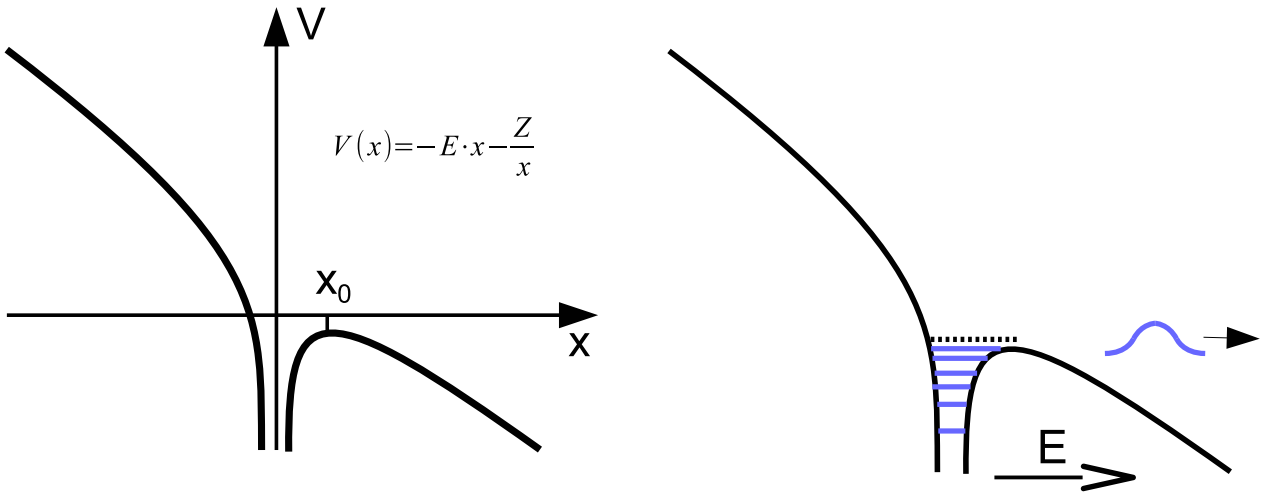

(a) Slice through a tilted Coulomb potential along y=0.

(b) Field-ionization in an atom.

Figure 5.10: Illustrations for field-ionization.

The bottom panel of figure 5.11 shows measurements of the ZES yield as a function of field strength of the imaging plates, where the latter was varied by a factor of 4. A monotonic increase in the relative yield is seen as the field strength increases; the total change is 10%, which is comparable to the uncertainty in the measurement. It is natural to ask, how much change can one reasonably expect? A simple estimate can be given for the hydrogen atom. Let's assume that population is spread evenly among all the states available (with equal weights for all n), from n=0 up to a threshold state, n_{th}, above which no states are occupied. Then contributions can be added up from the states that are above n_{min} to calculate the ionized yield: $Y(n_{min}, n_{th}) = n_{th} - n_{min}$. Comparing results for n_{min}=28 and n_{min}=40, for different values of n_{th}, it is found that a difference of 10% can be explained if one chooses $n_{th} \approx$150. However, this number can be very different depending on the value of n_{th}. For instance, for n_{th}=39, which the lower field strength can not reach, but any higher field strength can, the difference in the population is 100%; in the opposite limit, if n_{th} approaches ∞, there is no difference in the ionized populations for the two different field strengths. At this point it is worth noting that n=150 corresponds to a binding energy of less than a millielectronvolt. The chance that Rydberg states close to or above this level are selectively populated through multiphoton ionization is very small. Taking this into account, the small change in the relative ZES yield as a function of field strength argues against field ionization as a source for the ZES.

5.4 Width of the Zero Energy Structure

So far most attention has been paid to the integrated yield of electrons contributing to the ZES, but the distribution as a function of momentum has not yet been analyzed. As it can be seen in most of the 2-dimensional distributions (e.g. figure 5.3a or 5.1a) the structure is mostly a circular peak in the p_z–p_y plane. In the following, first the width is estimated for different systems, and it is tested whether one can

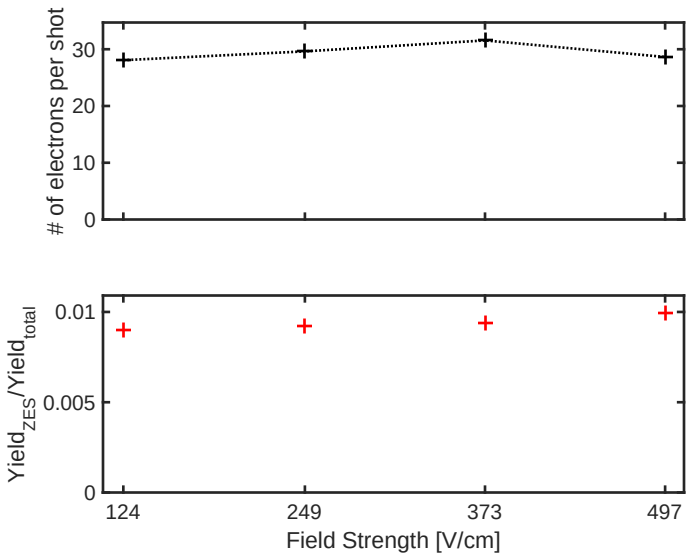

Figure 5.11: Bottom Panel: dependence of the ZES yield relative to the total yield on the electric field strength of the Velocity Map Imaging fields in case of CH_2IBr. Top panel: total yield per laser shot.

manipulate it by changing the parameters of the laser pulse. The analysis presented below is different from what is outlined in section 2.6, however it is rather straightforward. Ideally, the goal would be to plot the yield Y as a function of the magnitude of the three-dimensional momentum: $Y \equiv Y(|\vec{p}|)$. Here, $|\vec{p}| \equiv \sqrt{p_x^2 + p_y^2 + p_z^2} \equiv \sqrt{p_\rho^2 + p_z^2}$ where p_ρ is the momentum component perpendicular to the laser polarization, p_z is parallel. In order to present the photoelectron spectrum, one usually measures the yield as a function of p_y and p_z; then, assuming cylindrical symmetry about p_z, one performs Abel-inversion to obtain the yield as a function of p_ρ and p_z. Then the kinetic energy is calculated from the momentum components to obtain the dependence of the yield on energy. A technical issue bars us from following the same procedure in case of the ZES: all Abel-inversion routines concentrate the noise in the experimental data either on the p_ρ=0 axis or at the zero momentum point (p_ρ,p_z)=(0,0). This makes analysis of the ZES unreliable if the rigorous procedure is followed.

To avoid such difficulties, a less rigorous approach is taken which still retains most of the important information. Only the directly observed yield is considered, as it is measured as a function of (p_y,p_z). No effort is made to extract information about the p_x component of momentum, which is along the time-of-flight axis, and it is also the direction along which the sample is injected into the interaction chamber. However this is justified by the fact that the ZES structure resembles a Gaussian peak centered at zero momentum, and also that the Abel-transform pair of a Gaussian, centered at zero, is another Gaussian with the same width, also centered at zero. Hence, to study the structure on a coarse level, there is really no need to perform the inversion. Electrons with higher kinetic energy which were projected to the center of the image were considered as a background level. The amount of this contribution was estimated and removed from the measured ZES signal.

Figure 5.12 shows the ZES distribution in case of CH_2IBr and CS_2 as a function of radius in the (p_y,p_z) plane for a transform limited 30 fs laser pulse centered at 780 nm with $\approx$7 $\frac{TW}{cm^2}$ intensity. Both curve place an upper limit on the full-width-at-half-maximum width of about 0.01 atomic units, which roughly corresponds to 0.6 meV kinetic energy. These are typical numbers that we will see during the subsequent measurements.

It is worthwhile to take a moment here and consider what kind of mechanism can lead to such a narrow feature in the photoelectron spectrum. Reminding ourselves that the energy spectrum bears direct

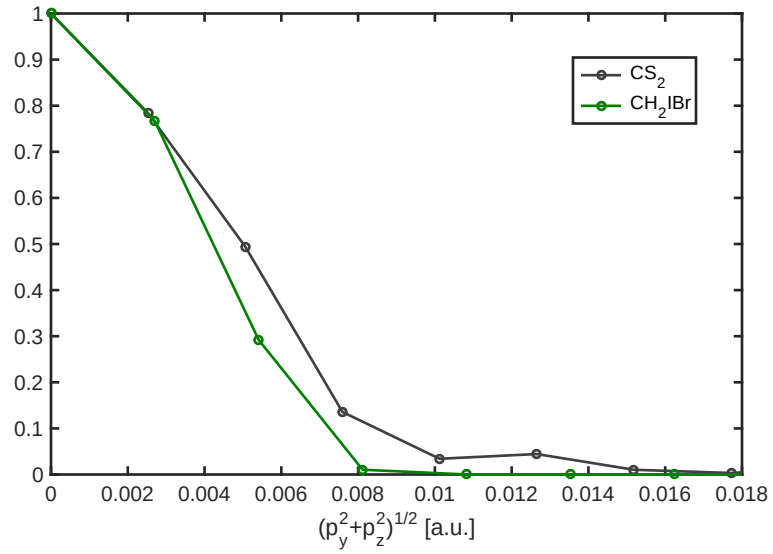

Figure 5.12: Radial distribution of the ZES structure in the detector plane.

signatures of time-sequence of events by virtue of the Fourier-transform, the timescale that corresponds to a width of ΔE=0.6 meV ($= 2.2 \cdot 10^{-5}$ a.u.) can be estimated. After a simple calculation, we get $\Delta t \sim \frac{1}{2\Delta E} \approx 2.3 \cdot 10^4$ a.u $\approx$ 550 fs. This is a timescale that is an order of magnitude longer than the laser pulse duration, and hence would suggest an ionization process that takes place way after the pulse is over.

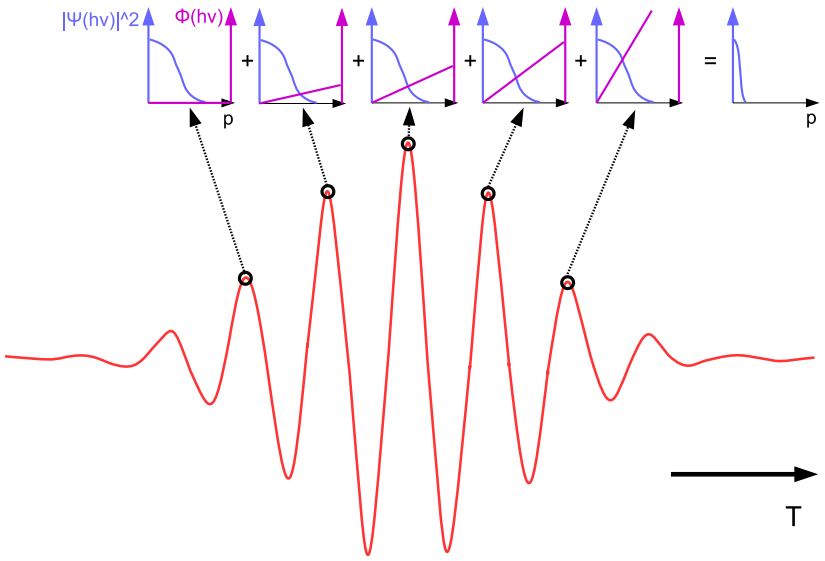

Figure 5.13: Cartoon illustrating interference of extended wavepackets to create a sharp peak in the momentum-space wavefunction. Red curve: Electric field of ionizing laser pulse. On top of the figure are distributions of the momentum-space wavefunction of the free electron wavelets born at different times.

However, there may be another explanation. This relies on ionization during the laser pulse, and interference between different portions of the ionized wavefunction. Suppose that one images the momentum-space wavefunction of an electron that escaped the atom or molecule through tunnel ionization. Assuming that initially the spatial extent of the free-electron wavefunction is roughly the same as that of the bound

electron (in other words, wavefunction dispersion is negligible during the ionization process), the Heisenberg uncertainty principle gives a relationship between the widths of the wavefunctions in coordinate and in momentum space. For argument's sake, let us assume that $\Delta x = 1$ a.u., $\Delta x \cdot \Delta p \geq \frac{1}{2} \rightarrow \Delta p \geq \frac{1}{2}$ a.u: this is the width of an ionized photoelectron "wavelet" in momentum space. In terms of energy, $\Delta E = \frac{\Delta p^2}{2}$= 0.125 a.u. $\approx$ 3 eV. In comparison, the width of the peaks that is measured is only about 1 meV. The explanation here is based on the interference of parts of free-electron wavefunction that appear in the continuum at different times. These individual parts can indeed be very broad in momentum space, but since tunnel-ionization only happens when the electric field is high, then at every half laser cycle only a portion of the electron wavefunction is liberated, with a small amplitude. This happens in regular time intervals, so the phase of the momentum-space wfn. has a different slope every time (by virtue of the Fourier-shift theorem). During measurement, these contributions add up, and interfere constructively at the momentum (or energy) where the phases are "locked": e.g. only at and near zero kinetic energy, giving rise to a narrow, well-defined peak. For graphical illustration, see fig. 5.13. In this picture, in principle one can manipulate the width of the resulting distribution, by adding up more or less wavelets. In an experiment, this can be accomplished by making tunnel-ionization happen on more or fewer occasions, by stretching or compressing the intensity envelope of the pulse. (For a stretched pulse, more intensity maxima fit within the pulse envelope.) One can calculate how many wavelets are required to "compress" the photoelectron peak width from 3 eV to 1 meV, by simply taking the ratio of the two quantities: it is of course 3000 in this case. This has to be compared with the number of intensity maxima that fit within the intensity envelope of a 30 fs laser pulse, assuming 2.6 fs period: one arrives at $2 \cdot \frac{30fs}{2.6fs}$=22. (The factor of 2 is to take into account that there are two intensity maxima in a laser period.) This result shows us that one would need two orders of magnitude more wavelets than what is available within the pulse envelope given the assumption about the initial spatial extent of the electron wavefunction.

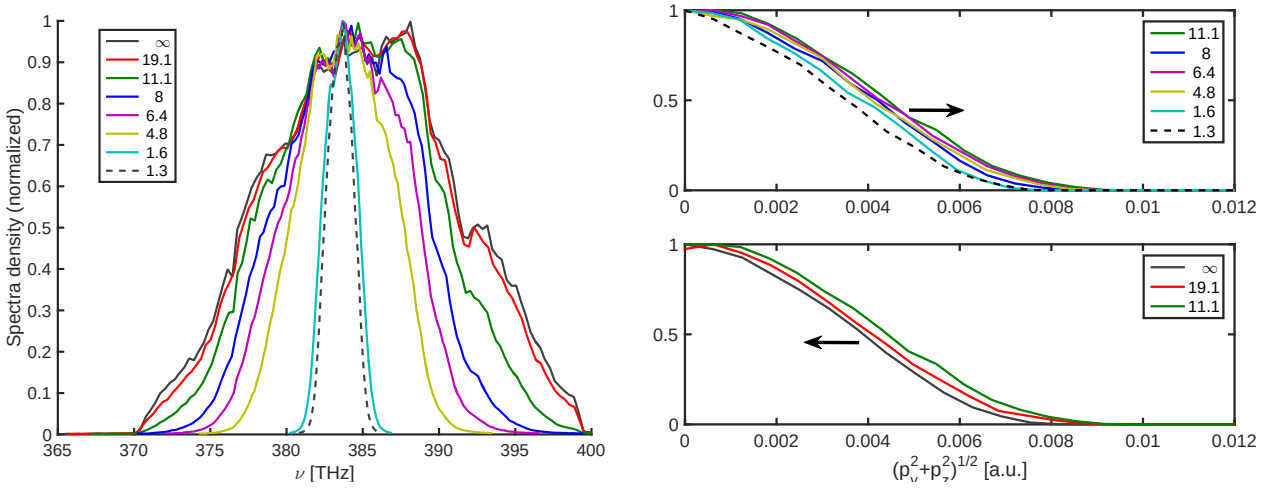

(a) Optical Spectra.

(b) Radial lineouts for the ZES.

Figure 5.14: Measurement of the ZES radial distribution in CS_2 as a function of optical bandwidth. Legend: the width σ of the Gaussian shaped spectra: $e^{-\frac{(\nu-\nu_0)^2}{\sigma^2}}$ in THz.

Experimental test of the above idea is carried out by manipulating the spectrum of the amplified laser pulses and measuring photoelectron distributions of CS_2. For the full bandwidth, the duration of the pulse was about 30 fs. The pulse shaper was used to first flatten the spectrum and then an amplitude mask of

the form $M(\nu) = A \cdot e^{-\frac{(\nu-\nu_0)^2}{\sigma^2}}$ was used, where the amplitude A and the width σ were varied such that the ionization yield for the parent molecule, CS_2^+, and hence the laser intensity, was kept constant. The normalized optical spectra are shown on figure 5.14a, while the resulting ZES distributions are on the upper and lower panels of figure 5.14b. For the lowest bandwidths, $\sigma \leq 11.1$ THz, there is a monotonic broadening of the ZES with the increase of the optical bandwidth, as it is apparent on the upper panel. The magnitude of the broadening however, is very small compared to the fractional change in the optical bandwidth, although these should be similar based on the model. Also, for $\sigma > 11$ THz, the trend seems to reverse, which is a counterintuitive result.

As an additional check, measurements on argon were performed as a function of intensity[3]. The data for circular polarization (figure 5.15b) shows no systematic variation in the width. For linear polarization (figure 5.15a) and for intensities $\leq$58 $\frac{TW}{cm^2}$ there is a monotonic narrowing, followed by monotonic broadening above 58 $\frac{TW}{cm^2}$ with increasing intensity.

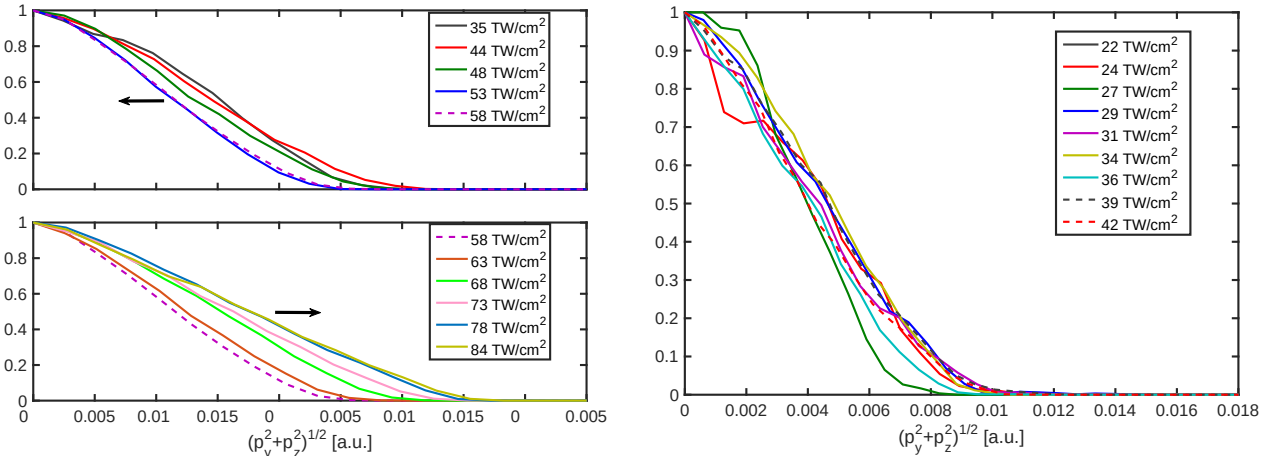

(a) Linear polarization.

(b) Circular polarization.

Figure 5.15: ZES radial distribution in Argon as a function of intensity (quoted in the legend).

Clearly, the width of the ZES was influenced by changing the properties of the laser pulse. It is perhaps not inconceivable that applying different laser pulse parameters resulted in populating different sets of Rydberg states, which in turn affected the measured distributions for the ZES, irrespective of how ionization actually took place.

To conclude this chapter, photoelectrons with $<$1 meV kinetic energy were studied; these were produced by ionizing atomic (Ar) and molecular (CH_2IBr, CS_2) systems. The work presented here examined a number of different mechanisms for producing electrons with such low kinetic energy. The measurements support that the first step involves populating Rydberg states via multiphoton excitation. The exact mechanism by which these Rydberg states are ionized is not clear at this point, but some of the experimental results can be used to argue for or against each one.

The picture involving interference of ionized wavelets is not a likely candidate given the nonmonotonicity and the small magnitude of the broadening effect when the excitation bandwidth is varied (figure 5.14b), and it is compounded with the discrepancy between the number of required and generated

[3]Even though frequency-dependent measurements on CS_2 would have been a natural choice to complement the data where the bandwidth was varied, at the time of writing this thesis no reliable intensity-dependent data on the ZES electrons for CS_2 was available. During data acquisition, special care needs to be taken not to saturate the detector locally with the low-energy electrons. This is usually not a concern when the focus is on the higher-energy portions of the distribution.

wavelets.

Autoionization is ruled out for cases that involves atoms, since there are no nuclear degrees of freedom that can store the excess energy that the ionized electron can leave behind.

Ionization in the static electric field of the VMI plates does not seem to be consistent with the magnitude of the change in the ZES yield as a function of external field strength. A simple estimate based on the hydrogen atom forecasts significantly larger changes in the signal than what is measured.

No conclusive statement can be made however about tunnel-ionization of the excited Rydberg states in the laser field. In principle, measurements where one would prepare the Rydberg states and then change the laser field strength for the ionization step separately could provide more evidence for or against it. The data presented in this chapter, where the laser intensity was varied, had the to steps coupled, in which case the results are hard to interpret.

Finally, one has to mention a scenario that is separate from the two-step process discussed above, which involves tunnel-ionization from the neutral ground state of the molecule in the laser field. As discussed in the introduction of chapter 3, during tunnel-ionization the laser field tilts the binding potential such that quantum-mechanical tunneling becomes possible for weakly bound electrons. However, ZES has been observed during photoionization of CS_2 using pulses with a central wavelength of 262 nm. The short wavelength and relatively low intensity (close to the ionization threshold) used during the experiment increased the Keldysh parameter by more than an order of magnitude (to $\gamma > 10$) compared to when the experiments were carried out with 30 fs pulses at 780 nm. This way ionization can be considered to take place in the multiphoton limit, and one can say that zero-momentum electrons are not predominantly produced by tunneling directly from the neutral ground state in the laser field.

Chapter 6

Conclusions

This thesis explored strong field ionization (SFI) of molecules using shaped ultrafast laser pulses with 30 nm bandwidth and dispersion-controlled, broadband pulses from a laser-induced filamentation source. velocity map images (VMI) of the generated photoelectrons were collected, either in coincidence or not in coincidence with the corresponding photoions, and converted to photoelectron spectra. The apparatus is described and characterized in chapter 2, along with some of the methods used to collect data and transform the VMI images to photoelectron spectra.

Chapter 3 demonstrates how the coincidence apparatus can be used to assign peaks in the photoelectron spectra of CH_2IBr and CH_2BrCl to different ionization-dissociation pathways associated with a set of low-lying states in the singly-charged ion. The validity of the idea that the kinetic energy of the photoelectrons is determined at birth is investigated in a simple analytic calculation on a model molecule, H_2^+. Building on this idea, different terms determining the net photoelectron energy are estimated, either experimentally or through model calculations. Finally, direct and indirect pathways to certain cationic states are distinguished.

Chapter 4 studies how the relative importance of the ionization pathways change as the duration of the driving laser pulse is shortened from 30 fs to below 10 fs. Broadband filamentation light source along with a rather unconventional way to compress the broadband pulses using a 4-f grating compressor (instead of chirped mirrors) was used. This technology enables a large degree of control over the spectral content of the light; for the work presented here, both the central wavelength and the bandwidth are varied. Measurements in CH_2IBr, CH_2BrCl and C_6H_5I (iodobenzene) show ionization to the first excited ionic state becoming dominant over that to the ground ionic state as the pulse is shortened below 10 fs. In case of CH_2IBr, detailed calculations interpret this as a result of the closing of ionization pathways involving nuclear dynamics. Pulse durations short enough to induce such response are said to be in the 'impulsive limit'.

The origin of photoelectrons constituting the Zero Energy Structure in VMI images is investigated in chapter 5. Starting off with observations of said structure as reported in literature, two steps are identified in the process of creating zero-energy photoelectrons. Intensity-dependent ionization yield data is presented for both atomic and molecular systems to argue that the first step is populating Rydberg states through a multiphoton transition. The significant role of the laser pulse duration in said transition is highlighted. The second step for creating the photoelectrons is the one responsible for releasing the weakly bound electron to the continuum. A number of possible candidates for the ionization schemes are considered: tunnel-ionization in the laser field, autoionization in molecules, and ionization in the field of the imaging plates. Somewhat independent of any specific ionization mechanism, an attempt at explaining the narrow width of the ZES is offered considering the interference of parts the photoelectron wavefunction ionized at regular time intervals. The viability of different schemes is cross-checked with

available data, and no single mechanism is found that is consistent with all of them.

Bibliography

[1] D. Strickland and G. Mourou, "Compression of amplified chirped optical pulses," *Optics Communications*, vol. 56, no. 3, pp. 219 – 221, 1985.

[2] S. Backus, C. G. Durfee, M. M. Murnane, and H. C. Kapteyn, "High power ultrafast lasers," *Review of Scientific Instruments*, vol. 69, no. 3, 1998.

[3] H. Fattahi, H. G. Barros, M. Gorjan, T. Nubbemeyer, B. Alsaif, C. Y. Teisset, M. Schultze, S. Prinz, M. Haefner, M. Ueffing, A. Alismail, L. Vámos, A. Schwarz, O. Pronin, J. Brons, X. T. Geng, G. Arisholm, M. Ciappina, V. S. Yakovlev, D.-E. Kim, A. M. Azzeer, N. Karpowicz, D. Sutter, Z. Major, T. Metzger, and F. Krausz, "Third-generation femtosecond technology," *Optica*, vol. 1, pp. 45–63, Jul 2014.

[4] J. Levesque and P. B. Corkum, "Attosecond science and technology," *Canadian Journal of Physics*, vol. 84, no. 1, pp. 1–18, 2006.

[5] M. Krug, T. Bayer, M. Wollenhaupt, C. Sarpe-Tudoran, T. Baumert, S. S. Ivanov, and N. V. Vitanov, "Coherent strong-field control of multiple states by a single chirped femtosecond laser pulse," *New Journal of Physics*, vol. 11, no. 10, p. 105051, 2009.

[6] E. Goulielmakis, Z.-H. Loh, A. Wirth, R. Santra, N. Rohringer, V. S. Yakovlev, S. Zherebtsov, T. Pfeifer, A. M. Azzeer, M. F. Kling, *et al.*, "Real-time observation of valence electron motion," *Nature*, vol. 466, no. 7307, pp. 739–743, 2010.

[7] M. Kling and M. Vrakking, "Attosecond electron dynamics," *Annu. Rev. Phys. Chem.*, vol. 59, pp. 463–492, 2008.

[8] P. Agostini and L. DiMauro, "The physics of attosecond light pulses," *Reports on Progress in Physics*, vol. 67, p. 813, 2004.

[9] T. Baumert, V. Engel, C. Meier, and G. Gerber, "High laser field effects in multiphoton ionization of Na_2. experiment and quantum calculations," *Chemical Physics Letters*, vol. 200, no. 5, pp. 488 – 494, 1992.

[10] W. Li, A. A. Jaroń-Becker, C. W. Hogle, V. Sharma, X. Zhou, A. Becker, H. C. Kapteyn, and M. M. Murnane, "Visualizing electron rearrangement in space and time during the transition from a molecule to atoms," *Proceedings of the National Academy of Sciences*, vol. 107, no. 47, pp. 20219–20222, 2010.

[11] D. Villeneuve, H. Niikura, N. Milosevic, T. Brabec, and P. Corkum, "A molecular-scale photocathode using a molecules own electrons to image itself," *Nuclear Instruments and Methods in Physics Research Section B: Beam Interactions with Materials and Atoms*, vol. 241, no. 14, pp. 69 – 72,

2005. The Application of Accelerators in Research and Industry - Proceedings of the Eighteenth International Conference on the Application of Accelerators in Research and Industry (CAARI 2004).

[12] M. Meckel, D. Comtois, D. Zeidler, A. Staudte, D. Pavičić, H. C. Bandulet, H. Pépin, J. C. Kieffer, R. Dörner, D. M. Villeneuve, and P. B. Corkum, "Laser-induced electron tunneling and diffraction," *Science*, vol. 320, no. 5882, pp. 1478–1482, 2008.

[13] G. Sansone, E. Benedetti, F. Calegari, C. Vozzi, L. Avaldi, R. Flammini, L. Poletto, P. Villoresi, C. Altucci, R. Velotta, S. Stagira, S. De Silvestri, and M. Nisoli, "Isolated single-cycle attosecond pulses," *Science*, vol. 314, no. 5798, pp. 443–446, 2006.

[14] M.-C. Chen, C. Mancuso, C. Hernández-García, F. Dollar, B. Galloway, D. Popmintchev, P.-C. Huang, B. Walker, L. Plaja, A. A. Jaroń-Becker, A. Becker, M. M. Murnane, H. C. Kapteyn, and T. Popmintchev, "Generation of bright isolated attosecond soft x-ray pulses driven by multicycle midinfrared lasers," *Proceedings of the National Academy of Sciences*, vol. 111, no. 23, pp. E2361–E2367, 2014.

[15] D. Irimia and M. H. M. Janssen, "Toward elucidating the mechanism of femtosecond pulse shaping control in photodynamics of molecules by velocity map photoelectron and ion imaging.," *Journal of Chemical Physics*, vol. 132, no. 23, p. 234302, 2010.

[16] A. E. Boguslavskiy, J. Mikosch, A. Gijsbertsen, M. Spanner, S. Patchkovskii, N. Gador, M. J. J. Vrakking, and A. Stolow, "The multielectron ionization dynamics underlying attosecond strong-field spectroscopies," *Science*, vol. 335, no. 6074, pp. 1336–1340, 2012.

[17] X. Xie, E. Lötstedt, S. Roither, M. Schöffler, D. Kartashov, K. Midorikawa, A. Baltuška, K. Yamanouchi, and M. Kitzler, "Duration of an intense laser pulse can determine the breakage of multiple chemical bonds," *Scientific Reports*, vol. 5, p. 12877, Aug 2015. Article.

[18] R. Trebino, K. W. DeLong, D. N. Fittinghoff, J. N. Sweetser, M. A. Krumbgel, B. A. Richman, and D. J. Kane, "Measuring ultrashort laser pulses in the time-frequency domain using frequency-resolved optical gating," *Review of Scientific Instruments*, vol. 68, no. 9, 1997.

[19] M. A. Dugan, J. X. Tull, and W. S. Warren, "High-resolution acousto-optic shaping of unamplified and amplified femtosecond laser pulses," *Journal of the Optical Society of America B*, vol. 14, pp. 2348–2358, Sep 1997.

[20] L. Bergé, S. Skupin, R. Nuter, J. Kasparian, and J.-P. Wolf, "Ultrashort filaments of light in weakly ionized, optically transparent media," *Reports on Progress in Physics*, vol. 70, no. 10, p. 1633, 2007.

[21] A. T. J. B. Eppink and D. H. Parker, "Velocity map imaging of ions and electrons using electrostatic lenses: Application in photoelectron and photofragment ion imaging of molecular oxygen," *Review of Scientific Instruments*, vol. 68, no. 9, pp. 3477–3484, 1997.

[22] S. R. Nichols, *Strong Field Dynamics and Control of Molecular Dissociation*. PhD thesis, SUNY Stony Brook, 2008.

[23] J. Eberly, J. Javanainen, and K. Rzaewski, "Above-threshold ionization," *Physics Reports*, vol. 204, no. 5, pp. 331 – 383, 1991.

[24] A. Vredenborg, C. S. Lehmann, D. Irimia, W. G. Roeterdink, and M. H. M. Janssen, "The reaction microscope: Imaging and pulse shaping control in photodynamics," *ChemPhysChem*, vol. 12, no. 8, pp. 1459–1473, 2011.

[25] C. S. Lehmann, N. B. Ram, and M. H. M. Janssen, "Velocity map photoelectron-photoion coincidence imaging on a single detector," *Review of Scientific Instruments*, vol. 83, no. 9, pp. –, 2012.

[26] G. Fraser, "The ion detection efficiency of microchannel plates (mcps)," *International Journal of Mass Spectrometry*, vol. 215, no. 1 - 3, pp. 13 – 30, 2002. Detectors and the Measurement of Mass Spectra.

[27] V. Dribinski, A. Ossadtchi, V. A. Mandelshtam, and H. Reisler, "Reconstruction of abel-transformable images: The gaussian basis-set expansion abel transform method," *Review of Scientific Instruments*, vol. 73, no. 7, pp. 2634–2642, 2002.

[28] G. A. Garcia, L. Nahon, and I. Powis, "Two-dimensional charged particle image inversion using a polar basis function expansion," *Review of Scientific Instruments*, vol. 75, no. 11, 2004.

[29] G. M. Roberts, J. L. Nixon, J. Lecointre, E. Wrede, and J. R. R. Verlet, "Toward real-time charged-particle image reconstruction using polar onion-peeling," *Review of Scientific Instruments*, vol. 80, no. 5, 2009.

[30] M. Abdallah, A. Landers, M. Singh, W. Wolff, H. Wolf, E. Kamber, M. Stöckli, and C. Cocke, "Capture and ionization processes studied with COLTRIMS," *Nuclear Instruments and Methods in Physics Research Section B: Beam Interactions with Materials and Atoms*, vol. 154, no. 1 - 4, pp. 73 – 82, 1999.

[31] J. Ullrich, R. Moshammer, A. Dorn, R. Drner, L. P. H. Schmidt, and H. Schmidt-Bcking, "Recoil-ion and electron momentum spectroscopy: reaction-microscopes," *Reports on Progress in Physics*, vol. 66, no. 9, p. 1463, 2003.

[32] L. V. Keldysh, "Ionization in the field of a strong electromagnetic wave," *Sov. Phys. JETP*, vol. 20, p. 1307, 1965.

[33] P. Sándor, A. Zhao, T. Rozgonyi, and T. Weinacht, "Strong field molecular ionization to multiple ionic states: direct versus indirect pathways," *Journal of Physics B: Atomic, Molecular and Optical Physics*, vol. 47, no. 12, p. 124021, 2014.

[34] A. F. Lago, J. P. Kercher, A. Bödi, B. Sztáray, B. Miller, D. Wurzelmann, and T. Baer, "Dissociative photoionization and thermochemistry of dihalomethane compounds studied by threshold photoelectron photoion coincidence spectroscopy," *The Journal of Physical Chemistry A*, vol. 109, no. 9, pp. 1802–1809, 2005.

[35] P. H. Bucksbaum, R. R. Freeman, M. Bashkansky, and T. J. McIlrath, "Role of the ponderomotive potential in above-threshold ionization," *J. Opt. Soc. Am. B*, vol. 4, pp. 760–764, May 1987.

[36] R. R. Freeman, P. H. Bucksbaum, H. Milchberg, S. Darack, D. Schumacher, and M. E. Geusic, "Above-threshold ionization with subpicosecond laser pulses," *Phys. Rev. Lett.*, vol. 59, pp. 1092–1095, Sep 1987.

[37] A. W. Potts and G. H. Fattahallah, "High-resolution ultraviolet photoelectron spectroscopy of CO_2, COS and CS_2," *Journal of Physics B: Atomic and Molecular Physics*, vol. 13, no. 13, p. 2545, 1980.

[38] G. N. Gibson, R. R. Freeman, T. J. McIlrath, and H. G. Muller, "Excitation and ionization dynamics in short-pulse multiphoton ionization," *Phys. Rev. A*, vol. 49, pp. 3870–3874, May 1994.

[39] D. Geißler, T. Rozgonyi, J. González-Vázquez, L. González, P. Marquetand, and T. C. Weinacht, "Pulse-shape-dependent strong-field ionization viewed with velocity-map imaging," *Phys. Rev. A*, vol. 84, p. 053422, Nov 2011.

[40] G. N. Gibson, R. R. Freeman, and T. J. McIlrath, "Verification of the dominant role of resonant enhancement in short-pulse multiphoton ionization," *Phys. Rev. Lett.*, vol. 69, pp. 1904–1907, Sep 1992.

[41] A. Baltuška, T. Udem, M. Uiberacker, M. Hentschel, E. Goulielmakis, C. Gohle, R. Holzwarth, V. S. Yakovlev, A. Scrinzi, T. W. Hänsch, and F. Krausz, "Attosecond control of electronic processes by intense light fields," *Nature*, vol. 421, no. 6923, pp. 611 – 615, 2003.

[42] P. Reckenthaeler, M. Centurion, W. Fuß, S. A. Trushin, F. Krausz, and E. E. Fill, "Time-resolved electron diffraction from selectively aligned molecules," *Phys. Rev. Lett.*, vol. 102, p. 213001, May 2009.

[43] M. Schultze, A. Wirth, I. Grguras, M. Uiberacker, T. Uphues, A. Verhoef, J. Gagnon, M. Hofstetter, U. Kleineberg, E. Goulielmakis, and F. Krausz, "State-of-the-art attosecond metrology," *Journal of Electron Spectroscopy and Related Phenomena*, vol. 184, no. 36, pp. 68 – 77, 2011. Advances in Vacuum Ultraviolet and X-ray PhysicsThe 37th International Conference on Vacuum Ultraviolet and X-ray Physics (VUVX2010).

[44] W. D. M. Lunden, P. Sándor, T. C. Weinacht, and T. Rozgonyi, "Model for describing resonance-enhanced strong-field ionization with shaped ultrafast laser pulses," *Phys. Rev. A*, vol. 89, p. 053403, May 2014.

[45] R. Trebino, K. W. DeLong, D. N. Fittinghoff, J. N. Sweetser, M. A. Krumbügel, B. A. Richman, and D. J. Kane, "Measuring ultrashort laser pulses in the time-frequency domain using frequency-resolved optical gating," *Review of Scientific Instruments*, vol. 68, no. 9, pp. 3277–3295, 1997.

[46] Y. Yu, K. Lin, X. Zhou, H. Wang, S. Liu, and X. Ma, "New C-H stretching vibrational spectral features in the Raman spectra of gaseous and liquid ethanol," *The Journal of Physical Chemistry C*, vol. 111, no. 25, pp. 8971–8978, 2007.

[47] W. D. M. Lunden, D. Geißler, P. Sándor, T. C. Weinacht, and T. Rozgonyi, "Discrimination between strong-field molecular ionization pathways using ultrafast pulse shaping," *Phys. Rev. A*, vol. 89, p. 053404, May 2014.

[48] M. Spanner, S. Patchkovskii, C. Zhou, S. Matsika, M. Kotur, and T. C. Weinacht, "Dyson norms in XUV and strong-field ionization of polyatomics: Cytosine and Uracil," *Phys. Rev. A*, vol. 86, p. 053406, Nov 2012.

[49] M. Seel and W. Domcke, "Femtosecond time-resolved ionization spectroscopy of ultrafast internal-conversion dynamics in polyatomic molecules: Theory and computational studies," *The Journal of Chemical Physics*, vol. 95, no. 11, pp. 7806–7822, 1991.

[50] J. Finley, P. ke Malmqvist, B. O. Roos, and L. Serrano-Andrs, "The multi-state {CASPT2} method," *Chemical Physics Letters*, vol. 288, no. 24, pp. 299 – 306, 1998.

[51] B. Wolter, C. Lemell, M. Baudisch, M. G. Pullen, X.-M. Tong, M. Hemmer, A. Senftleben, C. D. Schröter, J. Ullrich, R. Moshammer, J. Biegert, and J. Burgdörfer, "Formation of very-low-energy states crossing the ionization threshold of argon atoms in strong mid-infrared fields," *Phys. Rev. A*, vol. 90, p. 063424, Dec 2014.

[52] C. T. L. Smeenk, L. Arissian, B. Zhou, A. Mysyrowicz, D. M. Villeneuve, A. Staudte, and P. B. Corkum, "Partitioning of the linear photon momentum in multiphoton ionization," *Phys. Rev. Lett.*, vol. 106, p. 193002, May 2011.

[53] T. Nubbemeyer, K. Gorling, A. Saenz, U. Eichmann, and W. Sandner, "Strong-field tunneling without ionization," *Phys. Rev. Lett.*, vol. 101, p. 233001, Dec 2008.

[54] E. B. Saloman, "Energy levels and observed spectral lines of ionized argon, ArII through ArXVIII," *Journal of Physical and Chemical Reference Data*, vol. 39, no. 3, 2010.

[55] R. Cireasa, A. E. Boguslavskiy, B. Pons, M. C. H. Wong, D. Descamps, S. Petit, H. Ruf, N. Thiré, A. Ferré, J. Suarez, J. Higuet, B. E. Schmidt, A. F. Alharbi, F. Légaré, V. Blanchet, B. Fabre, S. Patchkovskii, O. Smirnova, Y. Mairesse, and V. R. Bhardwaj, "Probing molecular chirality on a sub-femtosecond timescale," *Nat Phys*, vol. 11, pp. 654–658, Aug 2015. Letter.

[56] T. A. Carlson, W. A. Svensson, M. O. Krause, T. A. Whitley, and F. A. Grimm, "Autoionization in N_2O as measured by angle-resolved photoelectron spectroscopy," *The Journal of Chemical Physics*, vol. 83, no. 8, 1985.

[57] T. Baumert, B. Bühler, R. Thalweiser, and G. Gerber, "Femtosecond spectroscopy of molecular autoionization and fragmentation," *Phys. Rev. Lett.*, vol. 64, pp. 733–736, Feb 1990.

[58] M. G. Littman, M. M. Kash, and D. Kleppner, "Field-ionization processes in excited atoms," *Phys. Rev. Lett.*, vol. 41, pp. 103–107, Jul 1978.